COUPLING AIRCRAFT AND UNMANNED AERIAL VEHICLE REMOTE SENSING WITH SIMULTANEOUS IN SITU COASTAL MEASUREMENTS TO MONITOR THE DYNAMICS OF SUBMARINE GROUNDWATER DISCHARGE

THESIS SUBMITTED TO THE GRADUATE DIVISION OF THE
UNIVERSITY OF HAWAIʻI AT MĀNOA IN PARTIAL FULFILLMENT
OF THE REQUIREMENTS FOR THE DEGREE OF

MASTER OF SCIENCE
IN
GEOLOGY AND GEOPHYSICS
JULY 2016

By
Joseph J. Kennedy

Thesis Committee:

Craig R. Glenn, Chairperson
Henrietta Dulai
Paul G. Lucey

ACKNOWLEDGEMENTS

I thank my advisor, Craig Glenn, for taking me on as a graduate student and for his patience and his willingness to be flexible with how this project evolved over the course of the last two years. He was instrumental in all aspects of this project from beginning to end. I thank Henrietta Dulai for her expertise and gracious willingness to provide valuable feedback and suggestions on both the data collection and data processing of all in situ measurements. I thank Paul Lucy for helping tremendously with troubleshooting the processing of aircraft thermal infrared (TIR) image data. I would also like to thank Jacque Kelly for her meticulous step-by-step instructions on how to best process TIR imagery. I want to thank James Bishop for his help with the collection of aircraft TIR imagery, as well as Chris Shuler and Joseph Fackrell for the time and effort put into the fieldwork carried out on Maui. I also need to thank Charles Devaney and Ted Ralston for their knowledge, input and suggestions in regards to obtaining and using unmanned aerial vehicles (UAV) for TIR imaging. Without their help, this project would not have been able to use UAVs for research. I thank Eunhee Lee of the Korea Institute of Geoscience and Mineral Resources and her UAV technician for showing me how to fly and collect TIR imagery. I want to thank the Maui DAR and all of the other Maui volunteers for deploying over 40 temperature data loggers around Maui to enable us to ground truth the aircraft TIR imagery. In alphabetical order: Flo Bahr, Wade Bortz, John Gorman and the Maui Ocean Center, Doug Harris, Tatiana Martinez, Don McLeish, Bill Rathfon, Dana Reed, Jill Rotaru, John Seebart, Larry Stevens, Karen Wetmore and Adam Wong. I also thank Casey Stewman at Maui DLNR Division of Forestry and Wildlife for working with us to provide access into the Ahihi-Kinau Natural Area Reserve. I thank the Geological Society of America for a Graduate Student Research Grant. This research was funded in part by a grant/cooperative agreement to C.R. Glenn from the National Oceanic and Atmospheric Administration, Project R/SB-12, which is sponsored by the University of Hawai‘i Sea Grant College Program, SOEST, under Institutional Grant No. NA14OAR4170071 from NOAA Office of Sea Grant, Department of Commerce. The views expressed herein are those of the authors and do not necessarily reflect the views of NOAA or any of its subagencies. UNIHI-SEAGRANT-XM-14-04.

ABSTRACT

Increased nutrient addition to the coastal zone via submarine groundwater discharge (SGD) has been suspected as the primary cause of the rapid decline of coral reefs and recurring macroalgal blooms on Maui. As a consequence, the island has been the focus of SGD research for close to 20 years. Very little, however, is known about the overall distribution of SGD around the island of Maui. To address this question, airplane-based thermal infrared (TIR) imaging was used to produce a spatially accurate regional scale map of coastal groundwater inputs around the western half of Maui. This data revealed over 70 areas of potential SGD locations over approximately 100km of coastline. Continuous radon monitoring was coupled with simultaneous time-series unmanned aerial vehicle (UAV or "drone") TIR imagery to quantify and characterize the dynamic variability of SGD. In this endeavor, this research has demonstrated that incorporation of time-series TIR imagery from a UAV with continuous radon monitoring enables new and highly refined constraints on the variability of SGD. UAV-TIR imaging reveals the exact location and dispersal of the SGD flow in relation to time-series radon monitoring location(s), thus eliminating assumptions about the surface area over which groundwater is discharging into the coastal zone, and therefore allows for highly improved and exacting determinations of SGD rates and nutrient fluxes. Furthermore, the use of time-series UAV-TIR imaging provides imagery at unprecedented resolutions that can supply spatial and temporal information about SGD dynamics that can be used to uniquely constrain and differentiate variations in flow.

TABLE OF CONTENTS

LIST OF TABLES

LIST OF FIGURES

LIST OF APPENDIX TABLES

LIST OF APPENDIX PANELS

1 INTRODUCTION

Submarine groundwater discharge (SGD) is the flow of water from land to the ocean through a coastally connected aquifer and is an important part of the water cycle that continuously supplies new naturally occurring or anthropogenically-derived nutrients to coastal waters (Valiela et al., 1990; Corbett et al., 1999; Paytan et al., 2006). As depicted in Figure 1, SGD is most often observed as a mix of fresh groundwater and recirculated ocean water that discharges within the coastal zone. Increased urbanization and agricultural development have the potential to introduce excess nutrients and other dissolved components including contaminants into the freshwater portion that flows beneath such areas, thus altering the chemical composition of SGD as well as its impact on coastal ecosystems (Johannes, 1980; Dollar and Atkinson, 1992; Moore, 1999; Slomp and Van Cappellen, 2004; Rodellas et al., 2015; Bishop et al., 2015). The impacts of nutrient loading can be many and subtle and can cascade throughout coastal ecosystems (e.g. Bowen et al, 2007) and include obvious manifestations such as macroalgal blooms that can smother or replace coral reefs in a variety of interrelated ways (e.g. Smith et al., 1981; Hunter and Evans, 1995; Lirman, 2001; McCook et al., 2001; Smith et al., 2002; Cocklin and Smith, 2005; Costa et al., 2008; Martinez, 2012; D'Angelo and Wiedenmann, 2014) as well as harmful phytoplankton algal blooms (e.g. Paerl, 1997; Hu et al., 2006; Lee and Kim, 2007; Paerl and Otten, 2013). These issues are especially pertinent in locations with oligotrophic ocean waters where even small amounts of nutrient rich groundwater can make up a substantial part of the overall nutrient budget (e.g. Li et al., 1999). Many studies have therefore focused on locating and accurately quantifying the flux of SGD so that realistic evaluations can be made regarding the associated nutrient fluxes that are delivered into coastal waters and ecosystems.

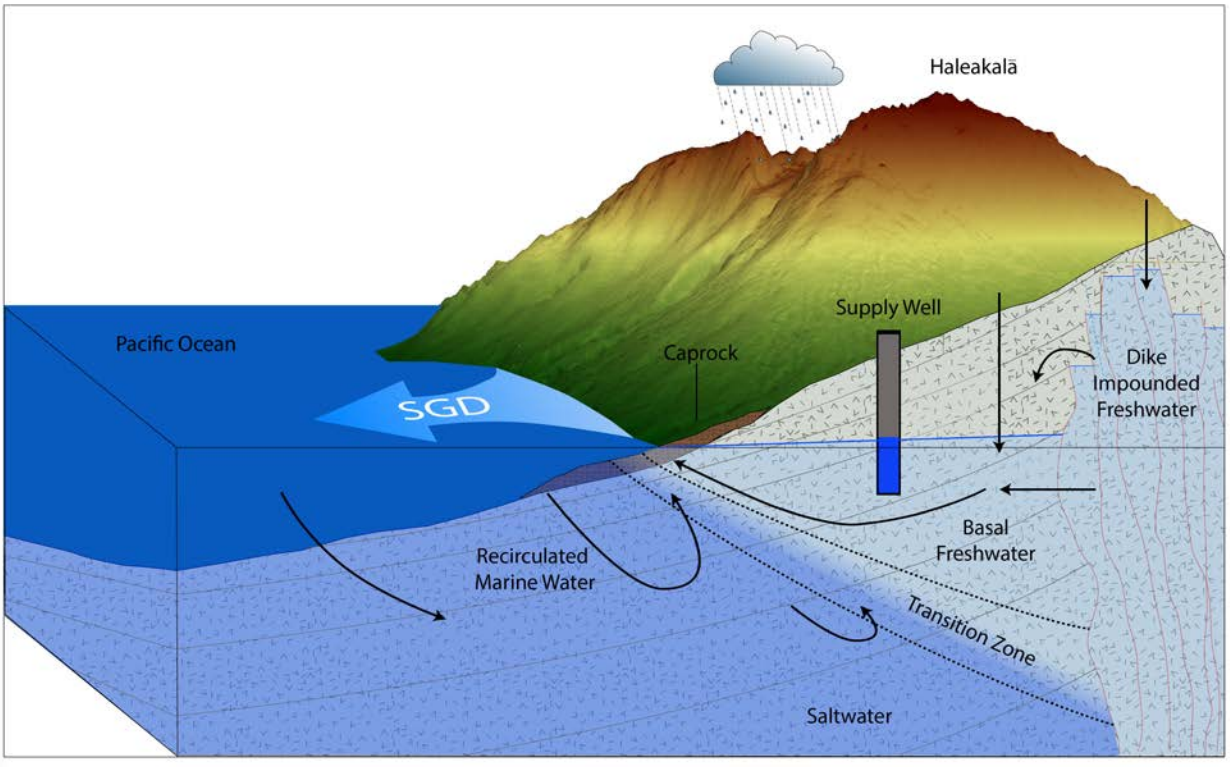

Figure 1: Conceptual diagram of Maui depicting the mixing of groundwater and recirculated seawater to form relatively cool, fresh, and buoyant diffuse or point-sourced SGD. From Bishop et al., 2015.

SGD occurs on a variety of scales and the multiple mechanisms that drive it can be complex. The most studied scale is the nearshore scale, which occurs within 10 m of the shoreline, while the largest scales include entire continental margins and their shelves (Bratton, 2010; Moore et al., 2008; Kwon et al., 2014). The primary mechanisms that drive SGD are terrestrial hydraulic gradients which can have seasonal variations, tidal pumping which has monthly and daily patterns, and wave setup which tends to be both seasonal and sporadic in time (e.g. Santos et al., 2012). The interaction between these drivers make SGD a fundamentally difficult phenomena to detect, observe and quantify, and the methods used to study it have varied greatly according to the needs of specific research endeavors, and as the technology to study it has evolved (see Burnett et al., 2006 for a review).

Because SGD is nearly impossible to visually detect with the human eye, thermal infrared (TIR) remote sensing techniques have proven to be a relatively new and highly valuable reconnaissance tool to rapidly locate and map SGD over large areas. Average groundwater temperature in coastal aquifers in the Hawaiian Islands (~20^{o}C), for example, contrast markedly with ambient coastal ocean temperatures (typically 24-30^{o}C), making temperature an excellent SGD tracer. Because groundwater is typically less saline than coastal seawater, it forms buoyant cool water “plumes” and diffuse discharges that can be

mapped as sea surface temperature (SST) anomalies by this technique. Furthermore, because TIR cameras are capable of detecting subtle temperature differences of ~0.1^{o}C, they can thus be used where ever there is a surface temperature difference between discharging waters and the water bodies receiving them. TIR imaging from aircraft was used by Banks et al. (1996) to locate and assess the areal extent of groundwater discharge locations within the Chesapeake Bay area. Duarte et al. (2006) used a handheld TIR camera to obtain oblique imagery from an aircraft to reveal the spatial distribution of SGD within Kaloko fishpond and the adjacent bay on the Big Island of Hawai'i. Mulligan and Charette (2006) used TIR imagery to provide qualitative information about the spatial variability of SGD within Waquoit Bay, Massachusetts. Johnson et al. (2008) quantified the use of TIR imagery from aircraft to produce regional TIR data maps of SGD along the western half of the Big Island of Hawai'i, and demonstrated how these could be correlated with sampled nutrient concentrations to produce surface water nutrient maps. The collection and subsequent processing routines for the aerial TIR collection method was later refined and elaborated by Kelly et al. (2013) who also demonstrated how variable flight altitudes can be used to accommodate imagery for a variety of settings. More recently Tamborski et al. (2015) used aircraft based TIR imaging to locate and measure the surface area expression of SGD on Long Island, NY. While the majority of TIR imaging has been done from aircraft with pixel resolutions of less than 5 meters, Wilson and Rocha (2012) used freely available satellite imagery to accomplish a regional scale assessment of SGD around southern Ireland (2016). The pixel resolution at which satellites are capable of collecting TIR imagery, however, is much larger with a resolution of 60 m which is often not sufficient to accurately resolve near-shore dynamics of SGD at the spatial scale that it typically occurs, as recently illustrated by Tamborski et al. (2015).

The studies noted above have shown that the use of TIR imaging cameras to detect areas of groundwater discharge into various coastal zones has dramatically increased the ability to both qualitatively and quantitatively image the extent, size and nature of how SGD mixes with seawater. This technology has proven itself to be a beneficial reconnaissance tool for investigating the spatial variability along areas of coastline that can be used for pinpointing specific locations for further research as well as characterize the discharge regime of different areas. However, due to weather dependent logistics and operational costs that typically limit surveys to a single overflight, this methodology has been limited in its capability to image SGD at the high temporal resolution needed to directly couple it with time-series monitoring methods, such as the use of the groundwater geochemical tracer radon-222.

Radon-222 (^{222}Rn) has become a valuable and widely used natural radiogenic tracer used to locate and quantify rates of SGD flow. Radon is a conservative, radioactive noble gas and its isotope

222Rn has a short half-life of 3.8 days. It is part of the U decay chain and being in contact with 222Rn emitting aquifer materials the concentration of 222Rn in groundwater is up to three orders of magnitude greater than that of ocean or surface water. This large enrichment, its unreactive nature, and its short half-life combine to make it an ideal tracer for monitoring subtle and/or rapid variations of groundwater discharge and mixing (Burnett and Dulaiova, 2003). Burnett and Dulaiova (2003) refined the method of using naturally occurring ^{222}Rn to quantify SGD flow rates using a non-steady-state mass-balance approach that accounts for all sources and sinks of ^{222}Rn using an automated continuous radon monitor to determine a linear advection rate through coastal sediments. The high temporal resolution of this time-series monitoring approach has been used for site-specific analysis, thereby revealing the variability of SGD within a specific segment of the coastal zone (Burnett and Dulaiova, 2006).

Despite the benefits of time-series radon monitoring to quantify SGD, there are still some limitations to this method. Time-series radon monitoring assumes that placement of the radon sampling intake platform is representative of the average groundwater signature of the entire discharging plume area. This may be a valid assumption in areas where diffuse seepage spans a broad areal extent, yet it is mostly unknown to what level this assumption impacts data collection at locations with point-source discharge where variable ocean conditions and limited groundwater plume extent complicate representative data collection. It is thus clear that the now well-established radon mass-balance method could benefit from better spatially constrained measurements. Furthermore, because time-series radon monitoring calculates a linear advection rate at a single location, it requires an accurate determination of the area where SGD occurs in order to calculate a volumetric flux. This has been accomplished in various ways: shoreline radon surveys (e.g. Dulaiova et al., 2010), combining spot sampling with beach face topography (e.g. Young et al., 2015) or the use of TIR imaging to locate and determine extent of SGD (Peterson et al., 2009). Each of these methods has its own distinct advantage. The main drawback, however, in all of these measurement approaches is that the geographic extent of discharging groundwater is only measured once, and then assumed to be constant throughout the monitoring period.

In summary, aerial TIR imaging is a valuable regional scale reconnaissance tool capable of providing high-resolution spatial information about the location of SGD and its discharge characteristics. The use of continuous radon monitoring as a geochemical tracer of groundwater has greatly expanded the ability to quantify the dynamic variability of ^{222}Rn within the coastal zone and thus the discharge of groundwater and the associated nutrient flux. Each method alone has limitations; however, when combined together they complement each other. Therefore, the purpose of this research is to develop

and evaluate a set of complimentary research tools and protocols that can be used in combination at any locale to (1) accurately determine the locations of SGD input and to differentiate the nature of discharge as point-source and/or diffuse flow, (2) determine the spatial distribution and variability of an SGD plume in relation to time-series radon monitoring platform, and (3) quantify the variability of the extent of SGD along any specific coastline as it varies through time. Therefore, the research presented below quantifies SGD at select locations on the islands of Maui and O'ahu with the following objectives: (A) obtain thermal infrared imaging of SGD by high altitude aircraft (A/C-TIR) to provide regional-scale reconnaissance maps of SGD within the coastal zones of Maui, enabling determination of SGD location and dispersal type; (B) confirm specific locations of SGD and stream inputs with reconnaissance unmanned aerial vehicle thermal infrared (UAV-TIR) imagery; (C) combine time-series radon monitoring with simultaneous time-series UAV-TIR imagery to determine how both SGD flux and coastal dispersal vary as a function of tidal cycle and time; (D) use in situ nutrient coastal pore water geochemistry along with the above to quantify nutrient fluxes to the ocean. Field studies for this research were conducted on the Hawaiian islands of Maui and O'ahu. Regional A/C-TIR studies were conducted on the island of Maui, and UAV-TIR and ^{222}Rn SGD studies were conducted on both islands.

2 METHODS

Regional Settings and Study Sites

Maui Island

The island of Maui is the second largest island in the Hawaiian archipelago with a surface area of approximately 1880 km^2. It consists of two shield volcanoes with a narrow isthmus connecting them. The smaller and older of the two is West Maui, which has eroded to form multiple peaks with steep cliffs and a maximum elevation of 1764 m (Stearns and Macdonald, 1942). The higher elevation slopes of West Maui are mostly protected forestland while the lower portions have had extensive agricultural development (Cheng, 2014). Haleakalā volcano is younger and much larger than the West Maui volcano. It reaches a maximum elevation of 3055 m and is classified as a dormant volcano with the most recent eruptions occurring approximately 500 years ago (Stearns and Macdonald, 1942). The coastal portions of these lava flows make up what is known today as the Ahihi-Kinau Natural Area Reserve (Natural Area Reserves System, 2012). A mix of protected forest, privately owned ranch land and residential developments cover the higher elevations of Haleakalā. The lower elevation slopes are a mix of agricultural lands and residential developments while the central isthmus is mostly sugarcane

agriculture or urban development (Gingerich, 2008). Due to the steep terrain of Maui that creates areas of high rainfall from orographic uplift along with permeable rock and little to no caprock, the island is expected to have varied amounts of SGD. Higher elevation windward slopes receive upwards of 8000 mm/y while leeward regions may get less than 400 mm/y (Giambelluca and Nullet, 1991). Hydrological budgets (Shade, 1996; 1997; 1999) also suggest that nearly all groundwater that is not pumped from the Maui aquifers is eventually lost to the coastal zone as SGD. Measurements based on these hydrological budgets suggest that SGD ranges from 0.4-29 m^3/m/d of shoreline (Figure 2).

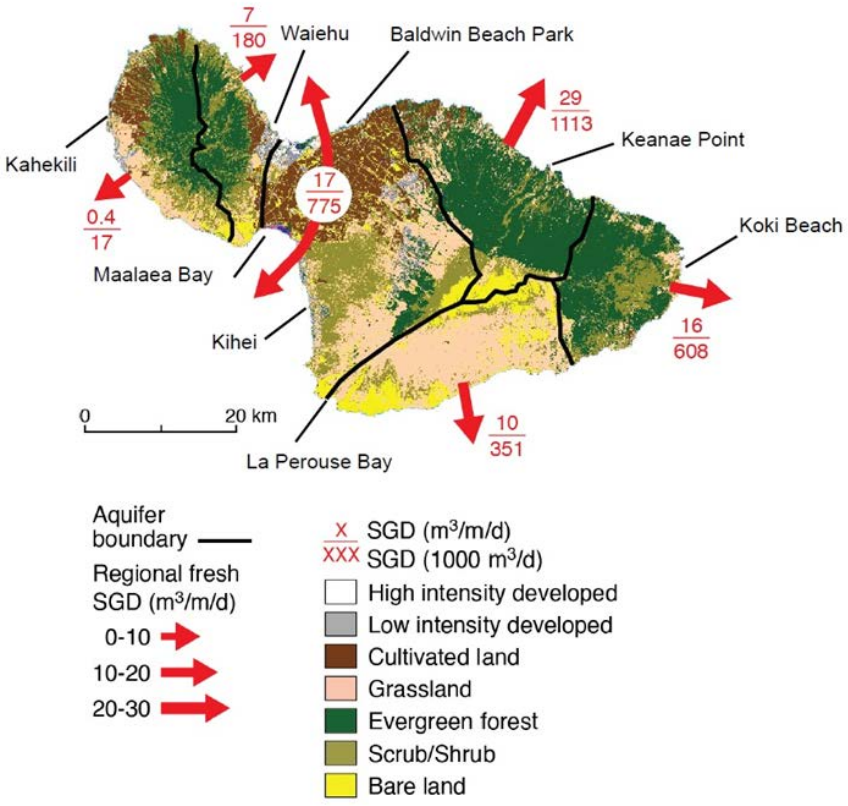

Figure 2: Land use map of Maui using data from NOAA's Coastal Change Analysis Program with principal aquifer divides shown as black lines. Groundwater discharge estimates, shown in red, are based on hydrologic budgets from Shade (1996; 1997; 1999). Top number is fresh groundwater discharge per meter of shoreline per day, while bottom number is total discharge per principal aquifer per day (Figure: Coastal Groundwater and Hydrology Research Group, University of Hawai'i).

Four research locations were selected on Maui (Figure 3) to represent a range of hydrogeologic and oceanographic settings found on the island. The Wahikuli Wayside Park study site is located on West Maui in Lahaina on lava flows from the Lahaina Volcanic series that erupted over the older Wailuku Basalt (Sherrod et al., 2007). The coastline is a relatively straight rocky stretch with little to no

sedimentary deposits and is sheltered from large northwest swells by the island of Molokai, however some larger south swells can refract up the coast and filter into the area causing mild longshore currents. The Kihei boat ramp study site is located in South Maui on the west-facing flank of Haleakalā, which consists of Kula Volcanics with some Holocene dune deposits around the area (Sherrod et al., 2007). The boat ramp is completely sheltered from wave activity and strong currents by a large jetty and has sandy beach deposits overlaying the basalt rock. The Māʻalaea study site is located on the southwestern portion of the isthmus that connects the two volcanoes, which itself consists of Pleistocene and Holocene alluvium that overlie both Wailuku Basalt and Kula Volcanics. A fringing reef, approximately 150 m offshore of an armored shoreline, attenuates large south swells that can impact the area. Strong longshore currents running from west to east, however, can cause mixing of any groundwater that discharges along this stretch of coastline. The Honolua Bay study site is a natural embayment located on the northern tip of West Maui and consists of Wailuku basalt overlain by Honolua Volcanics on either side, creating cliff faces of 20-30 m (Sherrod et al., 2007). The area can be impacted by large northwest swells during winter months, but is extremely calm during the summer time. An important aspect of this location is that Honolua Bay is noted for exhibiting both SGD and stream flow, with stream flow into the bay persisting for no more than 80 percent of the year (Cheng, 2014).

Oʻahu Island

The island of Oʻahu is the third largest main Hawaiian island with a surface area of approximately 1540 km^2. Oʻahu was formed by two shield volcanoes that have experienced a tremendous amount of flank slumping and erosion, leaving behind its two remnant mountain ranges. The Koʻolau Range, making up Eastern Oʻahu, with a maximum elevation of 946 m, and the Waiʻanae Range, forming Western Oʻahu, with a maximum elevation of 1227 m (Engott et al., 2015). On Oʻahu, the Wailupe Beach Park study site is located on the southern facing portion of the Koʻolau Range (Figure 3), which consists of unconsolidated marine calcareous sediments that overlie older Koʻolau Shield Volcanics (Stearns, 1939). A fringing reef crest over 500 m from shore with a relatively shallow reef flat attenuates all wave energy. This site was selected because SGD of the area has been well documented in previous SGD research studies (Holleman, 2011; Dimova et al., 2012; Kelly et al., 2013; Richardson et al., 2015), because of its ease of access from the University of Hawaiʻi, and because in this protected back reef setting the emanating SGD is not readily mixed away by wave activity.

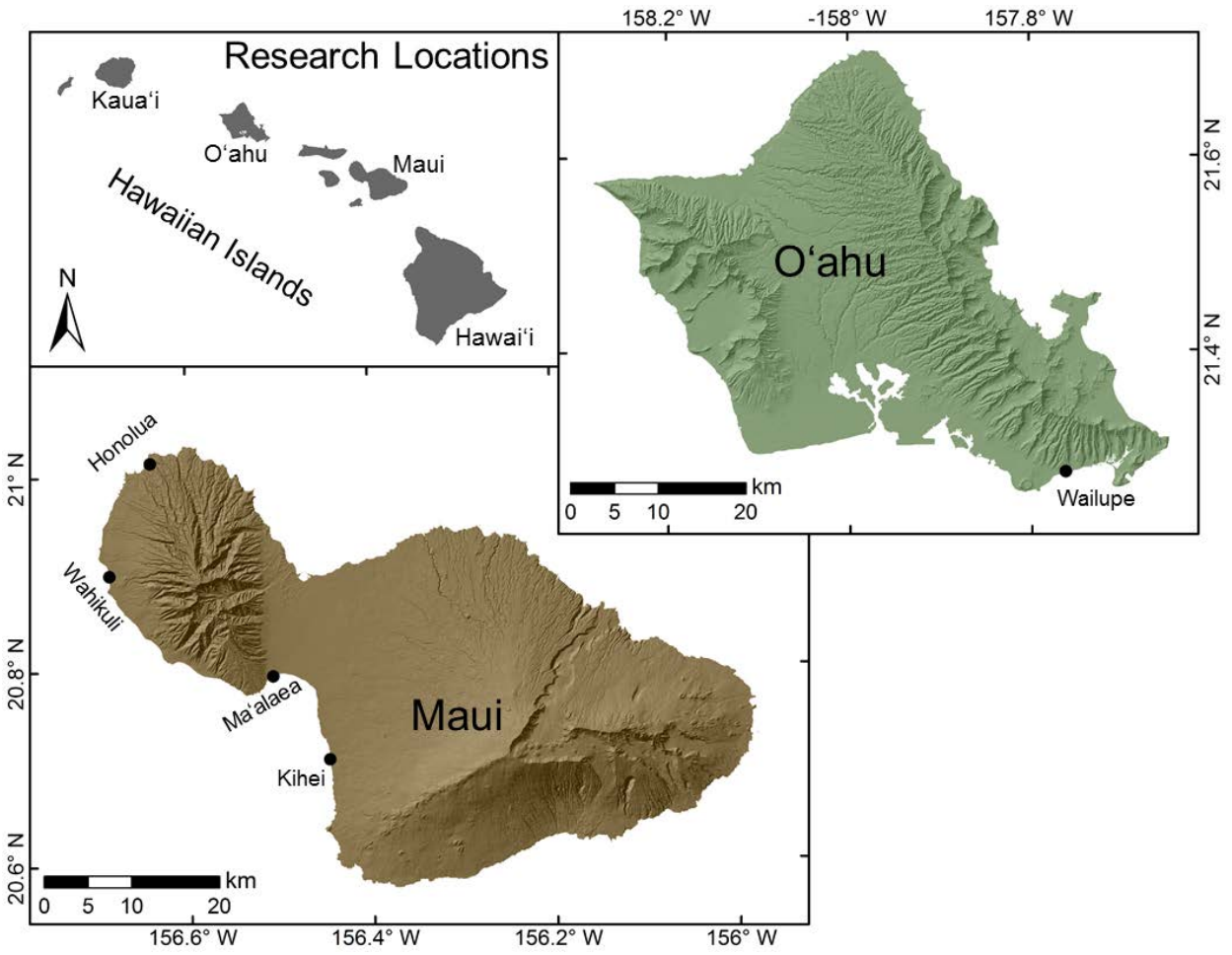

Figure 3: Shaded relief topographic map of Maui and O'ahu showing site-intensive research locations (dots).

Regional Scale Aircraft Thermal Infrared (A/C-TIR) Imaging

Equipment and Data Collection

Our regional A/C-TIR imaging equipment and methodology (Table 1) closely followed that of Kelly et al. (2013), and began with creating flight lines around the Maui coastline using a GIS system (ArcGIS 10.1, Esri) (Figure 4). Using a 25mm focal-length lens with a side-to-side field of view of 27.5°, a flight altitude of 2134 meters (7000 feet) was determined as optimal, providing an imaging swath width of 1038 m with parallel flight lines designed to include 30% overlap to ensure full coverage in case of airplane roll or deviation from the flight line. In order to ground truth the flight data, 42 data loggers (Hobo Pendant, Onset Computer Corporation) were deployed 20-30 m offshore around the island before the research flight at designated locations that ensured at least 2 data loggers were located

within the imaging path of all flight lines. Each data logger location was recorded with a hand-held GPS device (eTrex 30, Garmin Ltd.) for later comparison to the georeferenced TIR imagery.

Table 1: Comparison of A/C-TIR and UAV-TIR platforms used in this study.

	A/C-TIR	**UAV-TIR**
Aerial platform	Piper Navajo Twin Engine	3DR X8+ Drone
TIR Camera system	FLIR Photon 320, uncooled microbolometer	FLIR Tau 2 640, uncooled microbolometer
Camera lens focal length	25 mm	13 mm
Onboard camera recording	Laptop computer	TeAx ThermalCapture Camera Backpack
Camera/w lens field of view	27.5^{o}	45^{o}
TIR camera temp calibration	Internal <0.1^{o}C	Internal <0.1^{o}C
Blackbody temp calibration	1 hot + 1 ambient	none
Max Flight duration	10 hr	15 min
Length shoreline imaged	100 km	< 1 km
Imaging swath width	1038 m	100 m
Flight altitude	2134 m	120 m
Pixel resolution	3.2 m	0.2 m

An uncooled microbolometer array camera (Photon 320, FLIR Systems, Inc.) was used for the collection of infrared images which captured imagery at a frame rate of 30 Hz. The camera and lens were mounted on a custom made platform so that the camera had a nadir view from the fuselage of the Piper Navajo twin-engine plane. A combined inertial navigation system/global positioning system or INS/GPS (C-MIGITS^{TM} II, BEI Systron Donner Inertial Division) recorded the pitch, roll, yaw, velocity, altitude and geographic location of the camera platform at the same frequency as the TIR camera for precise post processing of each individual frame.

Unlike Kelly et al. (2013) who used one black body for cold, intermediate and hot temperature calibration, we used separate hot and cold black bodies in this study to mitigate the possibility of unstable calibration temperatures that could occur during black body temperature changes and re-equilibration, both between and during every flight line. The hot black body was regulated to maintain 35°C, while the cold black body was an ambient temperature black body that slowly fluctuated with aircraft cabin temperature, averaging about 15°C. The two different temperatures bracketed the range of possible temperatures imaged. The incorporation of two black bodies enabled consistent repeatable temperature calibration before and after each flight line. Both black bodies were mounted on sliders for quick movement into and out of the cameras field of view. 100 frames of each black body were collected with the exact temperature of each automatically recorded. The calibration images were later

used in post-flight processing to convert raw data values to temperatures using the temperature calibration equations of Kelly et al. (2013).

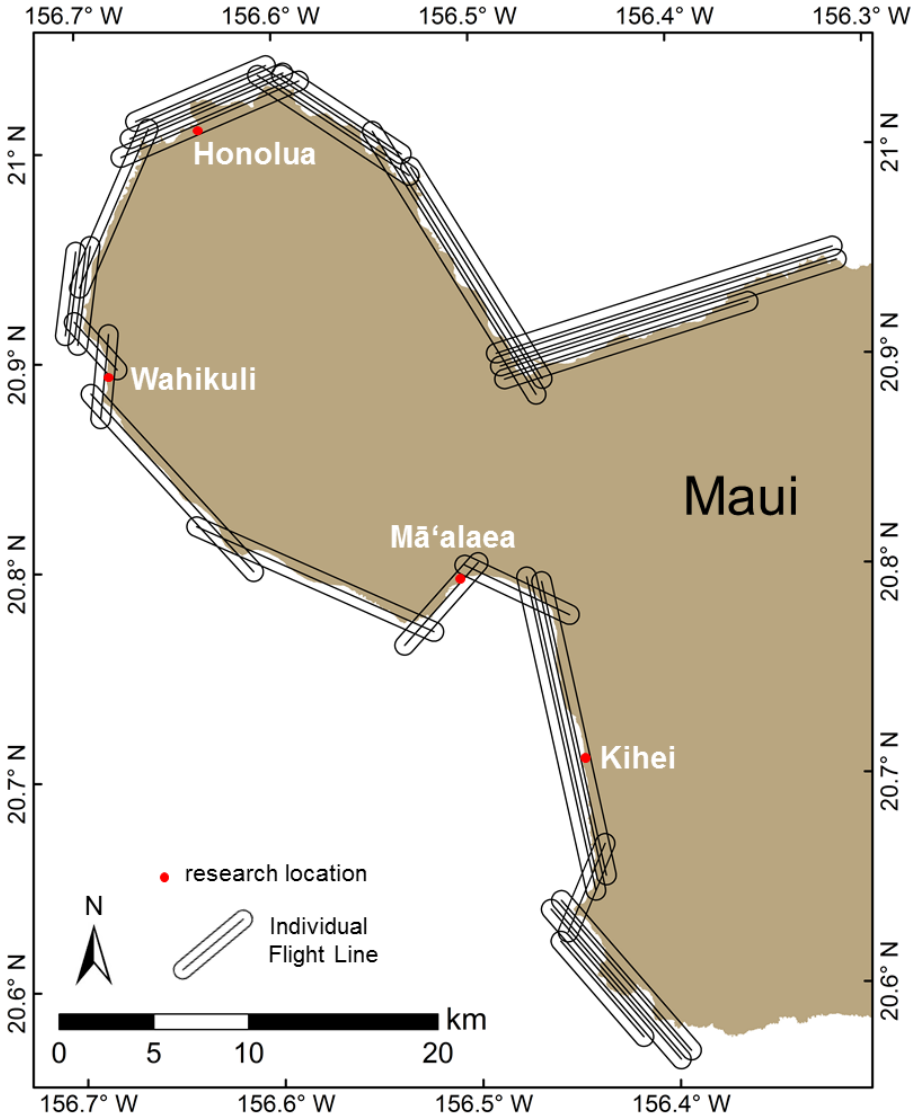

Figure 4: Map of the western portion of Maui showing aircraft TIR flight lines. The center line is the flight path while the buffer zone around the flight path is the camera imaging swath width.

A/C-TIR Image Processing

Post-flight data processing followed the procedures shown in the data processing flow chart (Figure 5) of Kelly et al. (2013), using ENVI+IDL (4.8, Exelis Information Solution Systems). Processing commenced with an initial quality control check of all recorded data, followed by black body temperature calibration of each individual frame using IDL code developed by Kelly et al. (2013) that had been modified to account for the incorporation of the extra black body. The modified IDL code also

provided the ability to correct for any warming or cooling of the camera that might take place during the collection of each flight line. The individual frames from each flight line where then mosaicked using the INS/GPS data to place each consecutive frame in its proper geographic location compared to the one before it using IDL code developed by Kelly et al., (2013). The result was a non-georeferenced image of each flight line. The automated georeferencing method of Kelly et al., (2013) produced imagery that was slightly offset from the coastal geography of Maui and therefore ground control point (GCP) georeferencing was used instead. 25-30 GCPs were used to warp each mosaicked flight line image to 0.5 meter resolution (WorldView-2, DigitalGlobe) visible light imagery. Images were then annotated to remove all land, leaving only the water which was temperature corrected based on the geographic coordinates of the in situ temperature data loggers. The final steps involved uploading the images into a GIS system where it was overlain on the WorldView-2 visible light imagery and false colorized to a set temperature scale. While the camera temperature resolution is 0.1°C, the final images are accurate to within ±0.5°C, which is due to the level of uncertainty of the temperature data loggers that were used for this project.

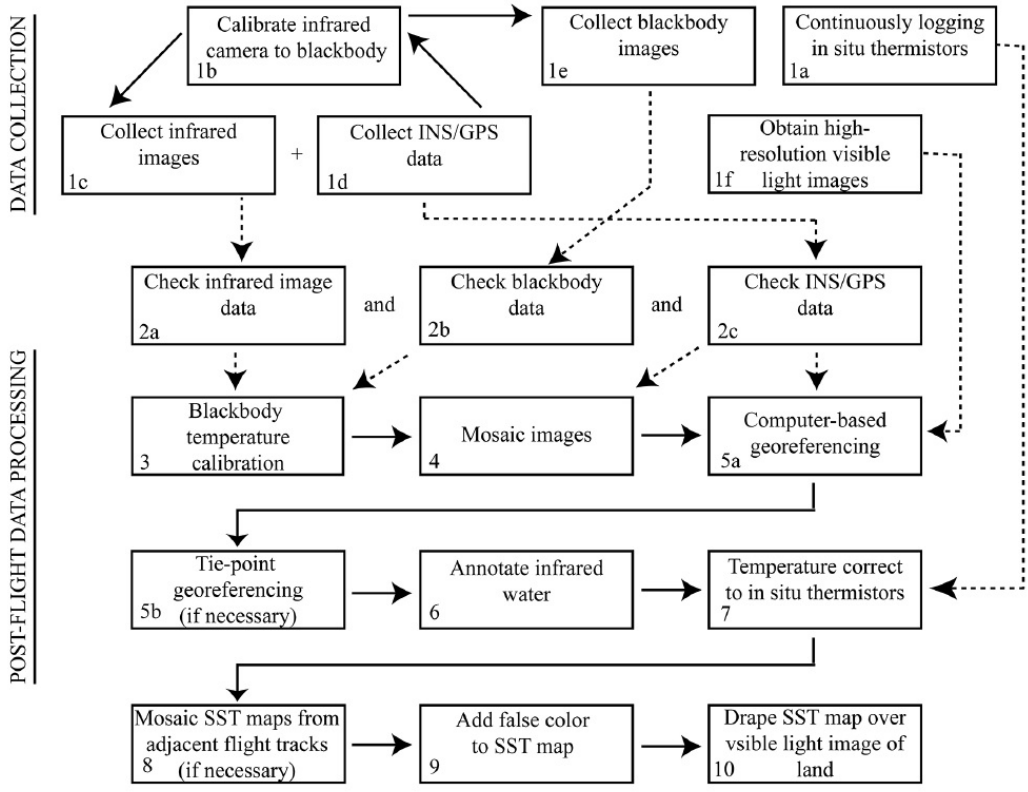

Figure 5: Flowchart of TIR image collection and post-flight processing showing all steps required to produce a final TIR image (from Kelly et al., 2013).

Time Series Unmanned Aerial Vehicle Thermal Infrared (UAV-TIR) Imaging

UAV-TIR Equipment

In order to obtain time series UAV-TIR imagery of each research location simultaneously with in situ radon measurements (described below), a TIR camera equipped UAV (X8+, 3D Robotics) was used (Table 1). The UAV was equipped with a high-resolution thermal imaging camera (Tau 2 640, FLIR Systems, Inc) with a 13 mm lens providing a side-to-side field of view of 45 degrees and capable of imaging temperature differences of 0.04°C. The camera was fitted with an onboard data capture system (ThermalCapture, TeAx Technology UG) that stores the raw imagery on a removable thumb drive at a frame rate of 9 Hz. An onboard switch controls the camera's recording function, so data collection occurred continuously from takeoff to touchdown. The raw data was converted to temperature within the TeAx software, which had been calibrated by TeAx. The UAV was fitted with a first person viewing system (LiveView, 3D Robotics) for real time monitoring of the TIR imagery. Real-time viewing provided the ability for field site reconnaissance and enabled optimum research scene composition.

UAV-TIR Data Collection

UAV-TIR data collection occurred after the radon time series deployments were setup at each site, which generally occurred the day before. All imagery was acquired during a falling tide with the first flight operated as close as possible to the time of high tide. The second UAV-TIR flight took place at mid tide and subsequent flights were flown as frequently as once per hour until low tide. Each flight lasted approximately 10-12 minutes, which provided enough time to image the entire scene at each location before needing to change UAV batteries. Due to FAA regulations (Section 336 of the FAA Modernization and Reform Act of 2012), all flights were conducted below an altitude of 122 m, which limited the field of view with a resultant pixel resolution of approximately 0.2 m. Loiter flight mode was used for all research flights as the on-board navigation system automatically maintained position, heading and altitude, but still allowed the pilot to make small adjustments for scene composition.

In order to ground truth the imagery obtained by UAV-TIR as well as provide information on vertical water column structure, temperature data loggers (Hobo Pendant, Onset Computer Corporation) were deployed at each location along a shore perpendicular transect. The temperature loggers were deployed as vertical strings of loggers hung beneath a fixed buoy. Each buoy contained 6 data loggers, one at the surface directly under the buoy to avoid solar heating, with the other 5 loggers spaced at 10 cm intervals below the surface to provide time series temperature profiles of the top 0.5 meter of water column. Only one data logger buoy was deployed at Kihei boat ramp due potential

impact with boats operating within the confined area. Geographic coordinates of each temperature data logging buoy were recorded with a handheld GPS (eTrex 30, Garmin Ltd.). The temperature data logger buoys provided in situ surface temperature data with an accuracy of ±0.5°C at one minute intervals for comparison to the TIR imagery. Immediately following each UAV flight, with the exception of Wahikuli Wayside Park, salinity and temperature depth profiles were completed along predetermined transects away from shore. A conductivity, temperature, depth logger (CTD-Diver, Slumberger Water Services) logging at a rate of 1 Hz with a temperature accuracy of ±0.2°C was slowly lowered through the water column at predetermined locations, coinciding with the offshore temperature logger buoy transect when possible. These data were used to confirm the existence and thickness of less saline cooler groundwater plumes.

UAV-TIR Image Processing

Initial image processing methods planned on using the inertial measurement unit (IMU) data from the UAV in a similar fashion to the A/C-TIR INS/GPS data to mosaic the thousands of TIR images collected during each A/C flight. This effort was not successful due to the amount of error associated with the IMU data and therefore another image processing method was developed. UAV-TIR imagery was manually accessed using TeAx's proprietary image viewing software (ThermoViewer 1.3.12, TeAx Technology UG). Out of the thousands of video frames obtained during each flight, individual frames were selected based on area covered and image clarity, then exported from ThermoViewer as a CSV file. Each file contained a 640 x 512 array of temperature values that were calculated based on calibrated pixel digital number values obtained by the camera sensor and converted into temperatures by the ThermoViewer software.

A vignette effect was apparent in all imagery obtained due to radial fall off of signal intensity around the periphery of an image that occurs with wide-angle camera lenses (Goldman and Chen, 2005). To correct for vignetting, a correction image was generated by imaging a blackbody in a laboratory setting at a set temperature for 1 minute. 7 frames equally spaced over the 1 minute long imaging process were averaged together, resulting in one raster image. All pixels of this raster image were then normalized to the average temperature, creating a raster image with an average of 1 °C, resulting in what is referred to below as the correction image. Because application of the correction image is multiplicative, normalizing to a scaling factor of one allows for correction without changing the overall scene temperature. The correction image was then applied to each individual TIR image using the method described below, thereby offsetting the lens based radial fall off (Figure 6).

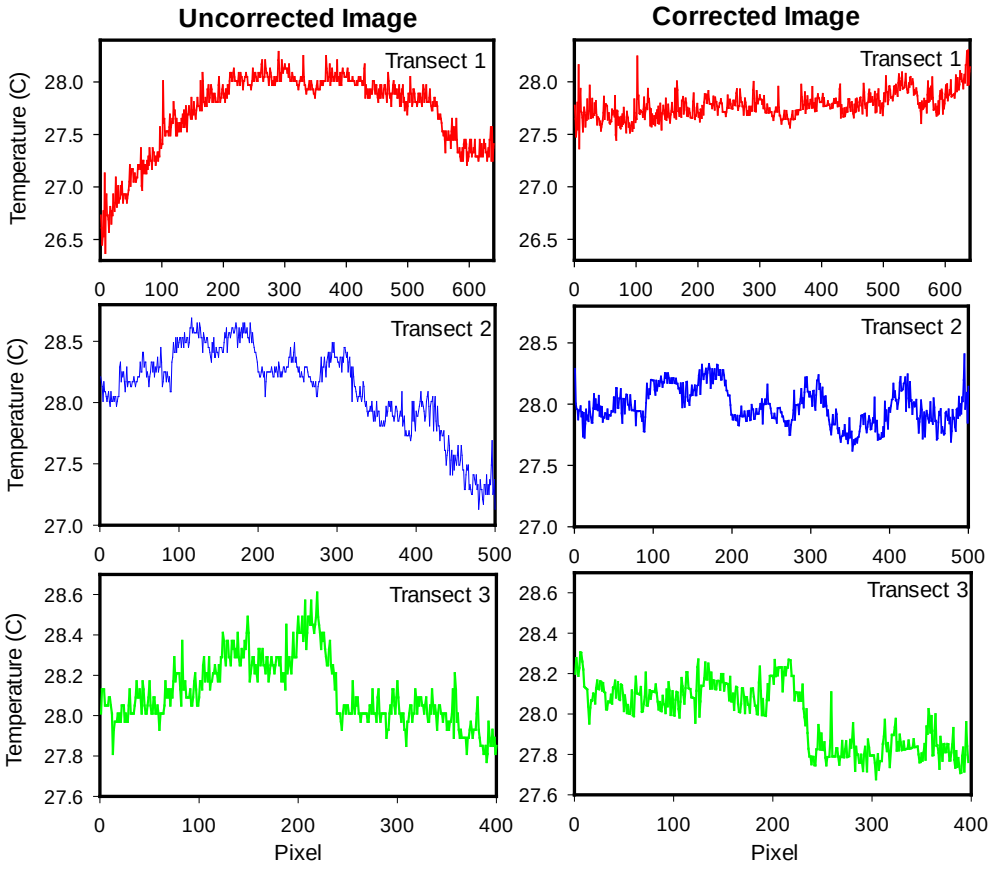

Figure 6: Temperature comparison showing how the image correction process corrects the image vignetting along the selected transects shown in Figure 7A below.

The amount of vignette effect on each image was not consistent and therefore the correction image needed to be weighted in order to not over or under correct that image. A region of interest (ROI) tool was therefore used to draw 3 rectangular polygons over the water within the uncorrected image that maximized the range of area covered, one horizontal, one vertical and a third on a diagonal, as illustrated in Figure 7B. The ROI tool provided the maximum, minimum, mean and standard deviation of all pixel values contained within. For example, an uncorrected image would have the largest standard deviation due to the discrepancy between the center pixels having higher values than those along the edges, whereas a properly corrected image would have the smallest standard deviation as the increase in pixel values around the periphery would result in a smaller pixel value range. If over corrected, however, the standard deviation within an ROI would also be larger than a properly corrected image due to pixel values along the periphery having a higher temperature than the center pixels which remain relatively unchanged throughout this process. The correction image was applied using the following formula:

$$F_i = I\,(1/C^{\alpha}) \qquad \text{eq. 1}$$

Where F_i is the final corrected image, I is the image to be corrected, C is the correction image and α is the correction weight. In order to determine the proper α for an individual image, the standard deviation of all three regions within the uncorrected image were averaged and recorded. The correction process would begin with an α value of 1.0. The average of all three ROI standard deviations would be recorded and the correction value would then be increased or decreased by 0.1 and applied to the original uncorrected image. This iterative process was repeated until the standard deviation of all 3 ROIs averaged together was minimized. Correction weights generally fell within a range of 0.5 to 1.5.

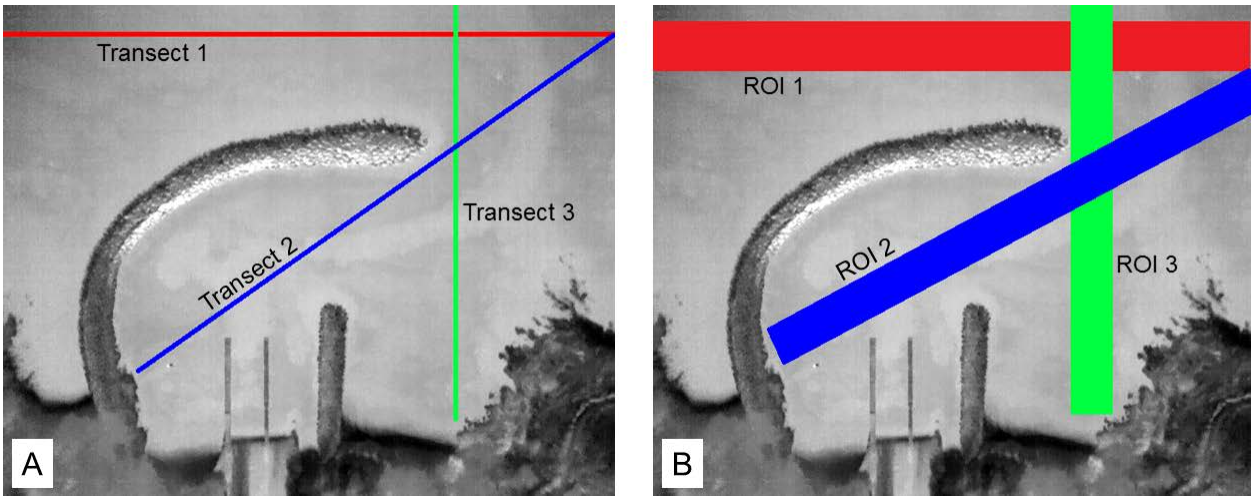

Figure 7: (A) shows the temperature transects used for the UAV image vignetting corrections illustrated in Fig. 6. (B) shows the regions of interest (ROI) used to determine the correction weight needed to properly adjust the vignetting for the entire scene.

Unlike our regional scale A/C-TIR imagery, which used GCP georeferencing to high resolution (0.5 m) visible satellite imagery, UAV-TIR images are obtained at a higher resolution (~0.2 m) and therefore it was not possible to identify enough GCPs in all of the imagery to consistently use this methodology. Each UAV-TIR image was therefore manually georeferenced in Google Earth where the images were positioned to best align with coastal features in the high-resolution imagery using the image overlay feature. The coordinates of each corner point of the image overlay were recorded and used to geo-register the image using a 1st degree polynomial transformation. All UAV-TIR images were georeferenced in the Universal Transverse Mercator (UTM) projection using the World Geodetic System 1984 (WGS-84) datum. To determine the accuracy of this method relative to the GCP georeferencing method, a comparison was done at one research location that allowed for GCP selection in all imagery

obtained. The calculated SGD plume sizes (see below for method) of three different flights were compared using the two different georeferencing methods. The corner point method had an average of 1.4% more surface area than when using GCP georeferencing. This is acceptable as it is insignificant when compared to the average +/- 14.6% uncertainty of plume size due to temperature boundary determination (see below).

Due to their spatial extent, Māʻalaea, Honolua Bay and Wailupe Beach Park could not be imaged within the field of view of one single frame and therefore required up to 3 frames to be mosaicked together. Images were layered over each other based on geographic coordinates, and pixel values were blended using pixel/distance averaging over a distance of 100 pixels and resampled using nearest neighbor method at a pixel resolution of 0.2 m. If a temperature difference existed between overlying areas due to one frame being colder than the other, 10 points were selected that appeared in both images and the average pixel temperature difference was determined. This difference was then applied to each individual pixel within one of the images and the mosaic process was continued. In some cases, a linear decreasing temperature trend across an image was observed in some of the corrected frames but not in an adjacent frame. This was assumed to be due to camera tilt as the UAV was constantly making small automated adjustments to stay in position. If a linear cooling trend of 0.5°C or greater was observed in temperature transects across the entirety of a frame, then a correction was applied to remove the trend. The correction process involved creating a 640x512 raster image where the amount of temperature correction needed was divided by either 640 or 512, depending on the orientation of the cooling trend, and each pixel value was increased by that amount compared to the one next to it. This raster was added to the TIR image using band math, thereby adding to each pixel temperature data value and thus flattening any linear decreasing temperature trend.

Final UAV-TIR image processing steps involved temperature correction and the application of a smoothing filter. The UAV-TIR imagery was compared to in situ temperature data loggers deployed during each flight. As needed, the image was corrected to the data logger temperatures that correspond to the time that imagery was obtained. Once each frame or mosaic was temperature corrected, a 5x5 kernel low pass filter was applied in order to smooth the imagery for temperature contouring as TIR imagery is inherently noisy which can complicate SGD plume temperature boundary determination. Land features were then annotated out, leaving only the water, which was then overlain on a visible light 0.5 m resolution georegistered aerial image of the land to produce the final result.

Plume Size and Contouring

The temperature inflection point method used by Johnson et al. (2008) for West Hawai'i and Kelly et al. (2013) for the island of O'ahu to determine plume temperature boundaries in A/C-TIR imagery did not produce consistent repeatable results in the UAV-TIR imagery obtained here, and therefore a different method was developed to delineate and contour SGD plume boundaries. This was accomplished by using a region of interest (ROI) tool to determine the mean SST of non-plume impacted offshore waters. The scene was then contoured at 0.5°C intervals below the mean offshore SST. The inflection point method was conducted at the one research site that enabled consistent results and was compared to the temperature contour method within a GIS system, revealing that a temperature contour of 1.0°C below the mean SST provided a comparable, consistent and conservative SGD plume boundary estimate. This contour of 1.0°C below the mean offshore SST was therefore chosen to best represent the outer boundary of SGD plume size, and is denoted ΔT_1. Due to uncertainty involved in determining the exact temperature to be contoured, the standard deviation of the temperature within the ROI used to determine the mean SST, which was then used to determine the possible plume size range of error. The SGD plume was contoured at one standard deviation above and below the calculated plume temperature boundary (ΔT_1), and the surface area of each was determined and used to calculate the range of uncertainty.

Time Series Radon Measurements

In order to derive total SGD fluxes, radon time series measurements were conducted from a small boat anchored close to shore at the Mā'alaea, Wahikuli Wayside Park, and Honolua Bay study sites. Time series deployments at Kihei Boat Ramp and Wailupe Beach Park were land-based as anchoring a boat was not feasible. All deployments lasted approximately 24 hours except Wailupe Beach Park, which lasted 5 hours. Radon in the surface water was integrated over 15 minute periods using a RAD-7 radon detector (Durridge, Inc) to achieve high temporal resolution for comparison with the simultaneous time series TIR imagery. Surface water was pumped from an intake valve located at a depth of 10-15 cm and into an air-water exchanger via a small bilge pump, or a peristaltic pump if setup on shore, enabling radon to be released into a closed air loop that is then fed into the radon detector where radon activity is measured. A conductivity, temperature and depth probe (CTD-Diver, Schlumberger) located at the intake valve logged these parameters every minute, while a second probe anchored on the seafloor below measured changes in water depth at the same frequency. Depth profiles of temperature and salinity were logged immediately after each UAV flight using a CTD-Diver in

order to determine the thickness of the SGD plume. For all Maui research sites, wind speeds were obtained from either the Lahaina or Kahului Airport weather station to determine radon evasion into the air. Winds speeds for Wailupe Beach Park site on O'ahu were obtained from the Honolulu International Airport weather station. Groundwater endmember concentrations of ^{222}Rn where determined by collecting discrete samples fronting each study site from 30-40 cm below the beach face at low tide using a push-point piezometer and pumped into a 250 mL bottle. Samples were analyzed later the same day using a radon-in-water analyzer (RAD H_2O, Durridge) and time corrected for losses due to decay.

Radon Mass Balance Model

SGD advection rates were determined using the Burnett and Dulaiova (2003) non-steady-state mass balance model approach. The model produces a linear advection rate that represents the groundwater discharge rate required to support the observed radon inventory in a 1 m^2 area ($m^3/m^2/d$). Under the assumption that the observed radon represents an average of the groundwater plume, the total water flux was then determined by multiplying the advection rate ($m^3/m^2/d$) at the stationary Rn platform located within the plume by the plume area as determined by the TIR imagery. As this study demonstrates below, the combination of radon mass balance with UAV-TIR imagery has the advantage of evaluating the validity of assumptions inherent with the method and improving on the geochemical-tracer technique.

Coastal Nutrient Concentrations and fluxes

To obtain nutrient concentration gradients away from shore, 7 to 20 nutrient samples were collected at each study site from the top 10 cm of the water column along shore-perpendicular transects at low tide. Endmember nutrient samples were also collected at the same time as the radon grab samples (mentioned above) using a push point piezometer at a depth of 30-40 cm below the beach face to determine the nutrient concentration of discharging groundwater. All nutrient samples were collected in high-density polyethylene bottles (250 mL HDPE, Wheaton) that were acid washed in a 10% hydrochloric acid bath and triple rinsed with deionized water. All samples were immediately chilled after collection, filtered the same day and then stored and transported in the dark to minimize biodegradation within the bottles. The samples were analyzed at the SOEST Laboratory for Analytical Biogeochemistry (S-LAB) within 1 week of collection using a Seal Analytical AA3 Nutrient Autoanalyzer for dissolved inorganic nutrients: phosphate (PO_4), silica (Si), nitrate and nitrite (N+N), and ammonium

(NH_4). In order to determine the uncertainty associated with nutrient analysis, a total of 8 samples were split into duplicate samples. The difference in nutrient concentration was then compared using relative percent difference resulting in an average 4.5% uncertainty for PO_4, 1.6% for Si, 8.0 % for N+N and 114.9% for NH_4. Four of the eight duplicate samples had NH_4 concentrations below detection limit resulting in extremely high uncertainty for NH_4 and are therefore not considered for nutrient flux calculations.

In order to compare our results with others in the literature, SGD rates and nutrient fluxes calculated in this study were converted to per meter of shoreline units by measuring the shoreline length of all imaged UAV-TIR SGD plumes using GIS software (ArcGIS 10.1, Esri). Averaged fluxes are the result of averaging all calculated SGD advection rates at each location and multiplying that rate by the average surface area calculated at each location including zero values to provide an average volumetric discharge rate ($m^3/m/d$). Maximum discharge fluxes were calculated using the maximum advection rate and corresponding plume surface area found at low tide. Minimum discharge rates were calculated using the minimum advection rate and corresponding plume surface area from high tide only if a ΔT_1 contour existed.

In order to compare coastal nutrient samples to previously published results for Hawai‘i, nutrient samples were normalized to the fresh water fraction in the manner of Hunt and Rosa (2009) using the following formula:

$$C_1 = C_{mix} + (C_{mix} - C_2) \times (S_{mix} + S_1) / (S_2 - S_{mix}) \qquad \text{eq. 2}$$

Where C_1 is the undiluted expected concentration of the sample, C_2 is the ocean water endmember concentration, C_{mix} is the sample concentration, S_1 is the freshwater endmember salinity, S_2 the ocean water endmember salinity, and S_{mix} is the sample salinity. Since the variance of the endmember salinities of the fresh groundwater are so small and do not significantly impact the final results (Hunt and Rosa, 2009) fresh water well salinities reported by Bishop et al. (2015) were used for all freshwater endmember salinity calculations.

3 RESULTS

A/C-TIR Imagery

Regional scale A/C-TIR imagery of Maui was collected during falling tide between 22:00 hr 07 June and 01:30 hr 08 June, 2014. All A/C-TIR imagery is shown as panels in Appendix A. Conditions were windy, and clouds obscured some areas. As noted above, at least two in situ surface water temperature loggers per flight line were used to correct aircraft recorded black body corrected TIR temperatures to in situ SST. All corrected SST ranged between 25-26.5°C. Overall, the imagery revealed more than 70 locations of cold water anomalies that had the appearance of either point source or diffuse seepage of SGD along the ~110 km stretch of coastline (Figure 8). Four primary research sites were chosen for detailed time-series monitoring which represented a range of hydrogeologic and oceanographic settings and taking into account coastal access, safe UAV launch site and ocean and weather conditions.

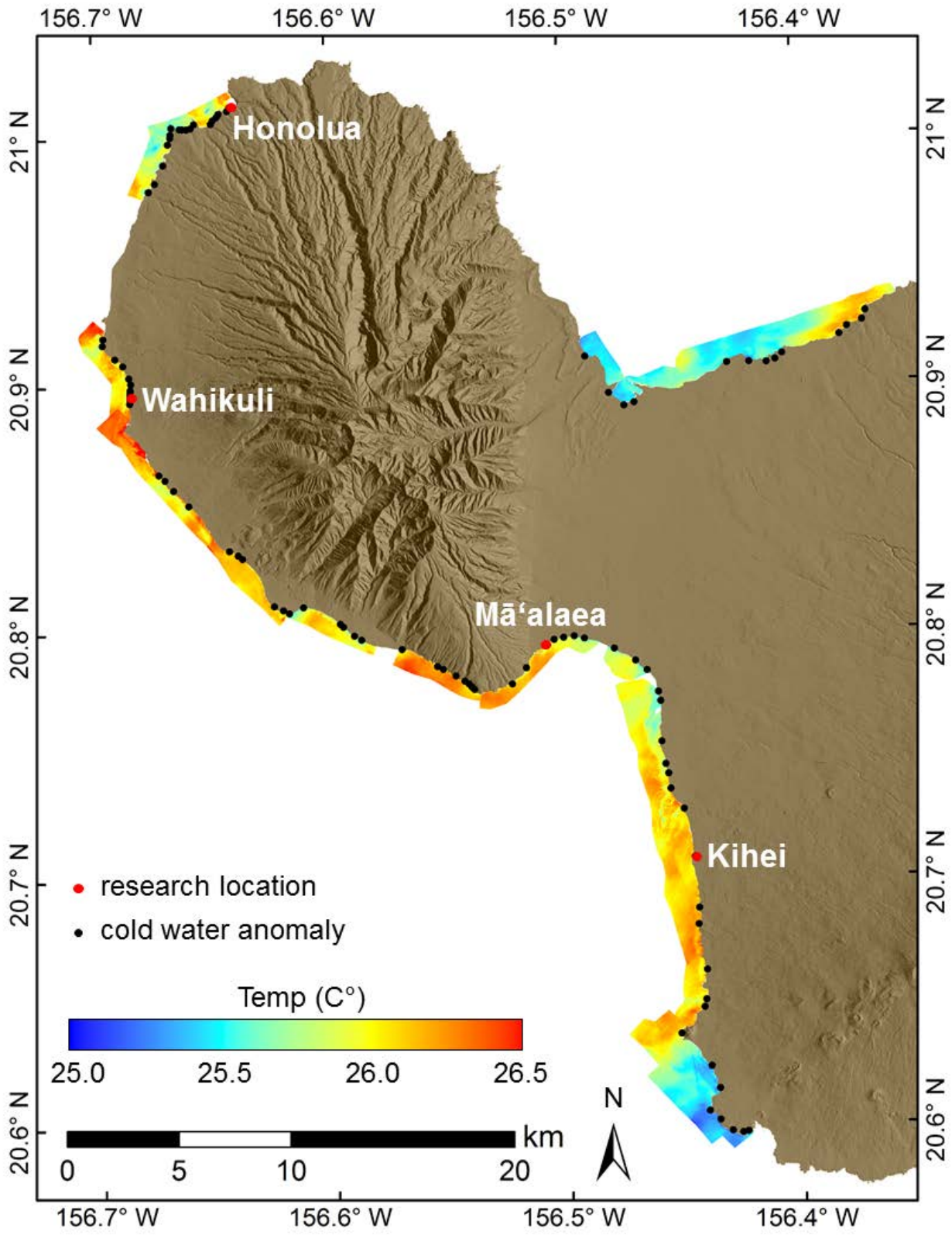

Figure 8: Regional scale TIR imagery of Maui obtained 07-08 June 2014 showing locations of potential SGD.

UAV-TIR Imagery

Results of UAV-TIR imaging and their ancillary data on Maui and O'ahu are shown in Tables 2-5 and Figures 9-12, with each study site discussed separately below. Each of these imaging flights were conducted during the daylight hours over the course of one-half tidal cycle, that is, during falling tides from high tide to low tide. The position of stationary radon platforms (discussed below) are also shown in these figures.

Wahikuli Wayside Park

A reconnaissance UAV-TIR flight was conducted in the morning on 28 August 2015 at low tide, followed by three time-series research flights on 29 August 2015 (Table 2). The first UAV-TIR flight was completed in the morning on 29 August during a falling tide. SSTs had a small temperature range of 1.3°C and no ΔT_1 contour surface area data could be obtained from the imagery. The second research flight was conducted one hour after the first flight at low tide with an SGD plume evident in the imagery (Figure 9). SSTs during this flight revealed the largest temperature range of the day with the calculated ΔT_1 contour showing a surface area of 150±40 m^2. The final flight occurred about 45 minutes after low tide with SSTs revealing the narrowest range of the day and no ΔT_1 contour surface area data was obtained from the imagery.

Table 2: Wahikuli Wayside Park time series UAV-TIR flights was conducted on 29 August 2015. Table shows time of flight, tidal stage, wind speed, Maximum and minimum temperatures imaged, absolute temperature range, average offshore SST plus or minus one standard deviation of the offshore temperature, and the surface area of the ΔT_1 temperature contour plus or minus the error based on the temperature boundary selection (see methods). No quantitative data is listed for the recon flight.

Flight time	Tidal Stage	Winds (m/s)	Min - Max SST (°C)	Temp Range (°C)	Offshore SST (°C)	ΔT_1 Surface Area (m^2)
08:01 - 08:13	falling	0-2	27.9-29.2	1.3	28.9±0.09	0
09:00 - 09:09	low	0-2	27.2-29.0	1.8	28.8±0.06	150±40
10:01 - 10:11	incoming	0-2	28.5-29.4	0.9	29.9±0.12	0

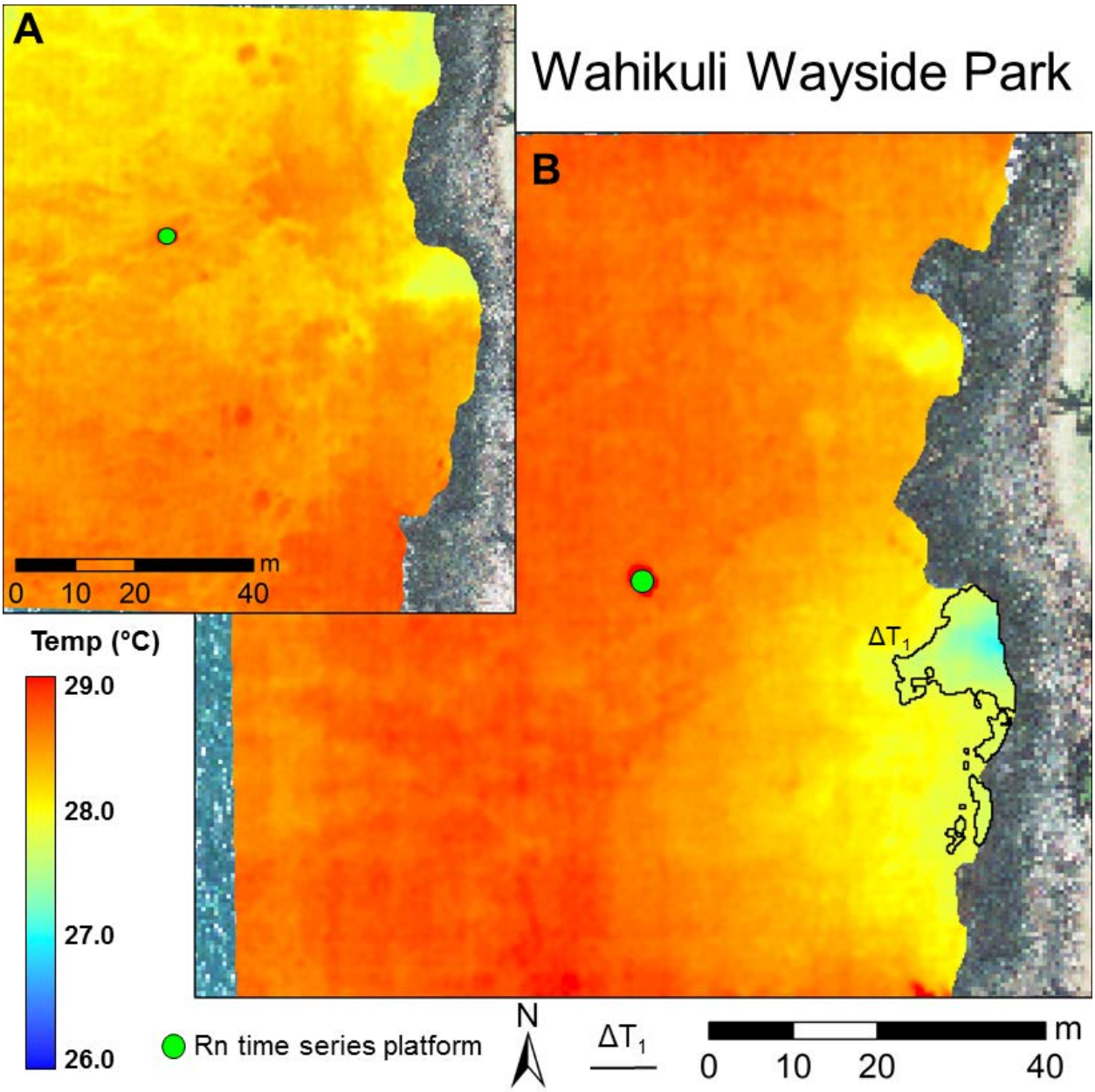

Figure 9: Wahikuli Wayside Park UAV-TIR imagery showing no ΔT_1 plume contour at (A) 08:00 falling tide while (B) 09:00 low tide has a small plume.

Kihei Boat Ramp

Four UAV-TIR flights were flown at Kihei boat ramp on 01 September 2015 as the tide was falling throughout the morning (Table 3; Figure 10). The first UAV-TIR flight was conducted at high tide with SSTs revealing the smallest temperature range of the day and no discernable SGD plume. The mean offshore SST of 28.3±0.07°C was the coolest of the entire day which was to be expected as this flight took place in the morning. Temperature and salinity depth profiles along the offshore transect during

the flight did not show a coherent trend, consistent with the lack of a discernable plume structure. The second UAV flight was conducted three hours later at mid-tide, revealing a clearly defined SGD plume discharging from the southeast corner of the area. Mean offshore SST had increased slightly and the ΔT_1 contour shows the second largest surface area of the day at 1750±260 m^2. Depth profiles at this time further revealed the dimensions of a layer of cooler less saline water with an average depth at 0.4 m. One hour later the third UAV flight revealed a similar scenario, however the ΔT_1 contour shows a smaller surface area of 1300±150 m^2. Mean offshore SST had continued to increase and depth profiles confirmed the trends observed by the TIR imagery. The final UAV-TIR flight occurred approximately 15 minutes after low tide, revealing the largest SST range of the tidal cycle as well as the warmest offshore temperature of 29.3±0.15°C. Despite occurring after low tide, the imagery revealed the largest plume size of the day with a ΔT_1 contour showing a surface area of 1990±410 m^2. Depth profiles were consistent with the previous two flights showing a cooler mixed layer of water approximately 0.4 m thick.

Table 3: Kihei boat ramp time series UAV TIR flight was conducted on 01 September 2015. Table shows time of flight, tidal stage, wind speed, maximum and minimum temperatures imaged, temperature range, average offshore SST plus or minus the standard deviation of the offshore temperature, and the surface area of the ΔT_1 temperature contour plus or minus the error based on the temperature boundary selection (see methods).

Flight time	Tidal Stage	Winds (m/s)	Min - Max SST (°C)	Temp Range (°C)	Offshore SST (°C)	ΔT_1 Surface Area (m^2)
07:00 – 07:12	High	0-2	27.6-28.6	1.0	28.3±0.07	0
10:02 – 10:11	falling	4-7	25.4-28.9	3.5	28.6±0.09	1750±260
10:58 – 11:09	falling	4-7	25.1-29.1	4.0	28.9±0.07	1300±150
11:52 – 12:03	low	4-7	25.2-29.6	4.4	29.3±0.15	1990±410

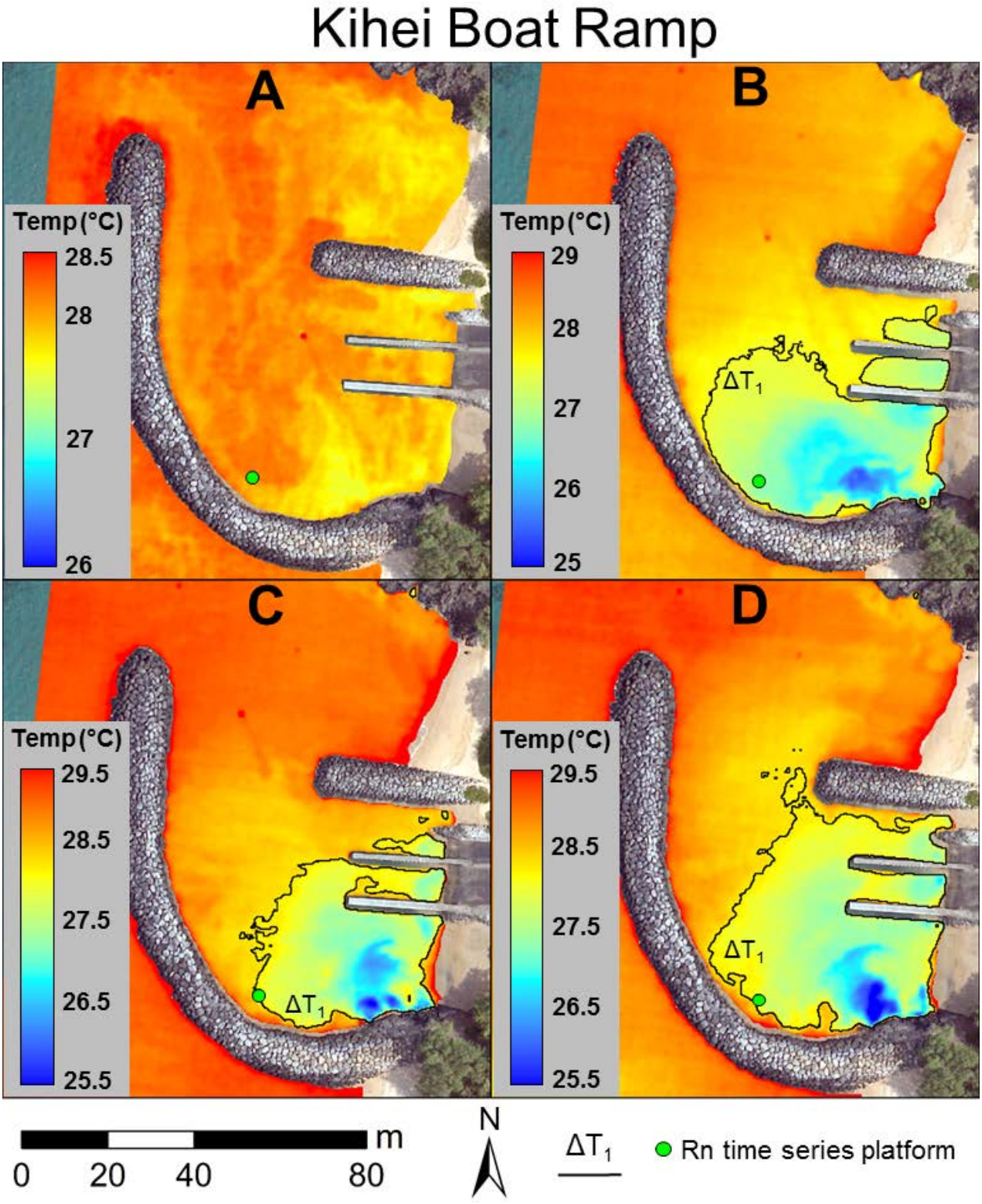

Figure 10: Kihei boat ramp UAV-TIR imagery showing the ΔT_1 plume contour over the course of dropping tide. (A) 07:00 High tide, (B) 10:00 dropping tide, (C) 11:00 dropping tide and (D) 12:00 low tide.

Mā‘alaea

Three UAV-TIR flights were flown at Mā‘alaea on 03 September, 2015 during a high swell event at 08:15, 10:58, and 14:10 hrs. None of these flights revealed a discernable SGD plume with all SSTs falling within a 1°C temperature range, thereby providing no quantitative surface area data. Salinity and temperature depth profiles were indicative of a well-mixed water column consistent with the high surf and strong currents observed during this time-series deployment and did not show any evidence of SGD. Previous research (Bishop et al., 2016) and the radon time-series monitoring did confirm the existence of SGD, however, ocean conditions were not conducive for obtaining TIR imagery due to homogenous surface water temperatures.

Honolua Bay

Four UAV-TIR flights were conducted at Honolua Bay on 05 September 2015 with calm ocean conditions (Table 4; Figure 11). Winds were initially light at 3-4 m/s in the morning and then increased to 5-7 m/s for the rest of the day. The stream at Honolua Bay was flowing during the entire time series operation. The first UAV-TIR flight was conducted mid-morning at high tide, detecting two faintly discernable SGD plumes emanating from the base of the basalt cliffs (Figure 11A). Mean offshore SST was the coolest of the day with the smallest overall temperature range. The ΔT_1 contour shows two very small plumes with a combined surface area of 80 ±65 m^2. At this time, temperature and salinity depth profiles along the offshore transect during the UAV-TIR flight showed evidence of a slightly cooler less saline mixed layer close to shore, although it did not extend out past the radon time series platform location. The second flight was conducted on a falling tide with a slightly warmer offshore SST and a larger temperature range. The ΔT_1 contour shows two well-defined SGD plumes with a combined surface area of 900 ±270 m^2. Depth profiles confirmed the existence of the less saline cooler SGD plume with a thickness of approximately 0.5 m, extending all the way out past the time series platform to the furthest offshore transect point. The third flight was conducted at approximately mid tide with two well-defined plumes evident in the imagery, with the ΔT_1 contour showing a combined surface area of 1300 ±300 m^2. Depth profiles agreed with the imaged surface expression of the SGD plumes, which revealed a cooler less saline mixed layer of similar thickness and extent as the previous depth profile. The final flight was completed just before low tide and had the largest temperature range imaged. Mean offshore SST was the warmest of the day and the ΔT_1 contour shows the largest surface area of the tidal half cycle, at 9200 ±700 m^2. Depth profiles again agreed with the imagery and showed a less saline cooler

layer of water extending beyond the time series platform to the furthest profile of the transect. The TIR imagery revealed and clearly differentiated the nearby stream input and its discharge area and therefore all surface area temperature contours that included the stream plume were removed from the SGD plume surface area calculations.

Table 4: Honolua Bay time series UAV TIR flight was conducted on 05 September 2015. Table shows time of flight, tidal stage, wind speed, maximum and minimum temperatures imaged, temperature range, average offshore SST plus or minus the standard deviation of the offshore temperature, and the surface area of the ΔT_1 temperature contour plus or minus the error based on the temperature boundary selection (see methods).

Flight time	Tidal Stage	Winds (m/s)	Min - Max SST (°C)	Temp Range (°C)	Offshore SST (°C)	ΔT_1 Surface Area (m^2)
09:38 – 09:47	high	3-4	26.4-27.9	2.0	27.8 ± 0.06	80 ± 65
12:46 – 12:55	falling	5-7	25.5-29.0	3.5	28.9 ± 0.07	910 ± 270
14:23 – 14:34	falling	5-7	23.4-29.1	5.7	29.0 ± 0.06	1300 ±300
15:55 – 16:07	low	5-7	23.1-30.5	7.4	30.4 ±0.07	9150 ±710

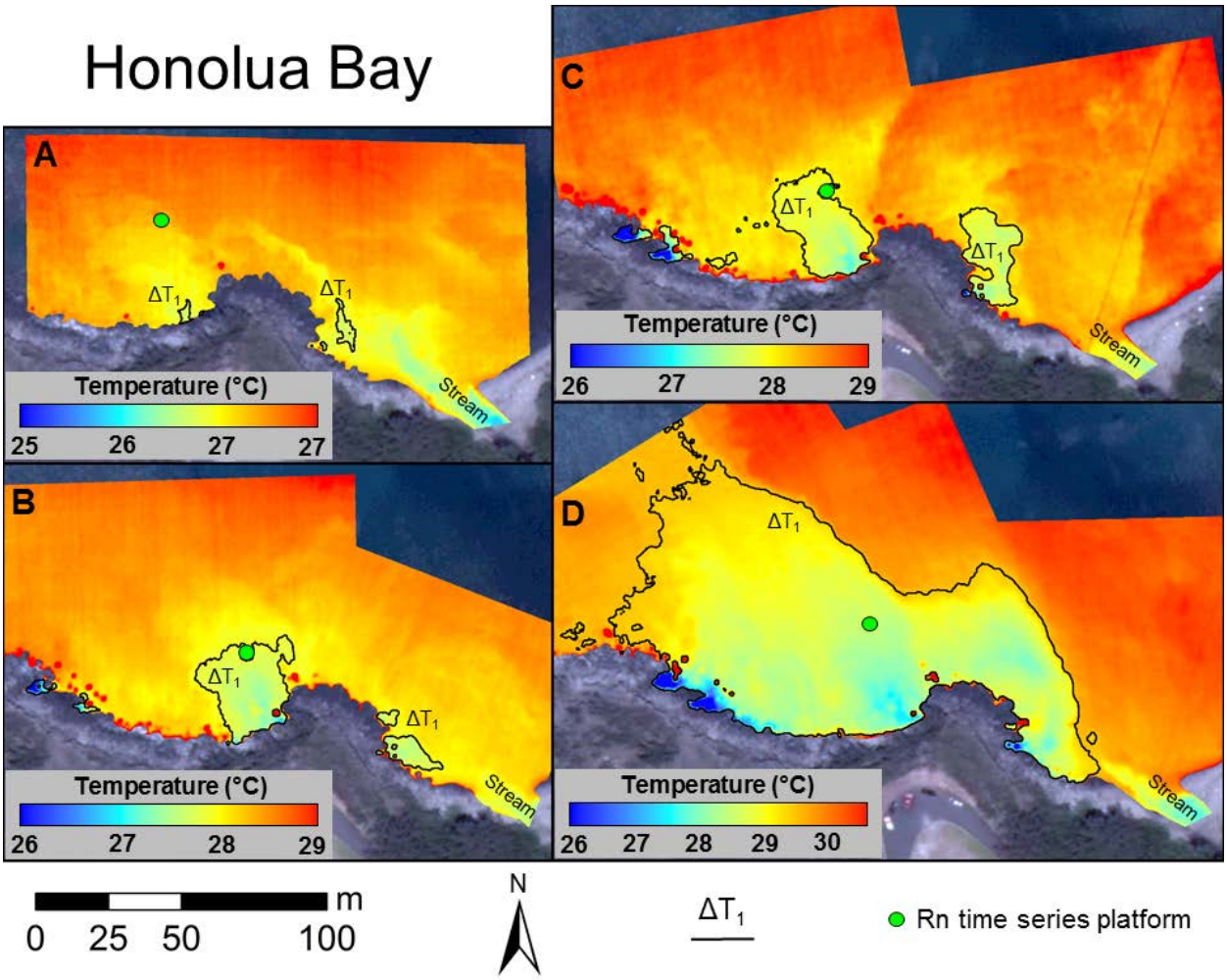

Figure 11: Honolua Bay UAV-TIR imagery showing the ΔT_1 plume contour over the course of dropping tide. (A) 10:00 High tide, (B) 13:00 dropping tide, (C) 14:30 dropping tide and (D) 16:00 low tide.

Wailupe Beach Park

UAV-TIR flights at Wailupe Beach Park on O'ahu were completed on 28 January 2016 (Table 5; Figure 12). The first flight was conducted in the morning approximately 1 hour after high tide in windless conditions. The mean offshore SST was the coolest of the day with the smallest overall temperature range, and the calculated ΔT_1 contour shows two separate plume sections. The western section shows a ΔT_1 with a surface area of 1000±370 m^2, while the eastern most section was not imaged in its entirety (Figure 12A) and therefore was not considered in the surface area calculation. These contoured areas, however, did not include any of what was previously known to be the main spring discharge at Wailupe (Richardson et al., 2015). The second flight was conducted 3 hours later on a falling tide in winds up to 2-4 m/s in an onshore direction. Mean offshore SST and overall temperature range had increased, with the calculated ΔT_1 contour revealing a surface area of 1800±360 m^2. The final flight of the day was conducted at low tide in winds of 3-5 m/s in an onshore direction revealing the largest SST range of the

day. Mean offshore SST had increased further, and the calculated ΔT_1 contour shows a total surface area of 7700±440 m^2.

Table 5: Wailupe Beach Park time series UAV TIR flight was conducted on 28 January 2016. Table shows time of flight, tidal stage, wind speed, Maximum and minimum temperatures imaged, temperature range, average offshore SST plus or minus the standard deviation of the offshore temperature, and the surface area of the ΔT_1 temperature contour plus or minus the error based on the temperature boundary selection (see methods).

Flight time	Tidal Stage	Winds (m/s)	Min - Max SST (°C)	Temp Range (°C)	Offshore SST (°C)	ΔT_1 Surface Area (m^2)
07:56 – 08:06	high	0	24.3-26.4	2.0	25.4±0.10	1000±370
10:51 – 11:02	falling	2-4	24.4-27.9	3.5	27.8±0.04	1780±360
12:26 – 12:35	low	3-5	25.3-30.9	5.6	30.7±0.07	7660±440

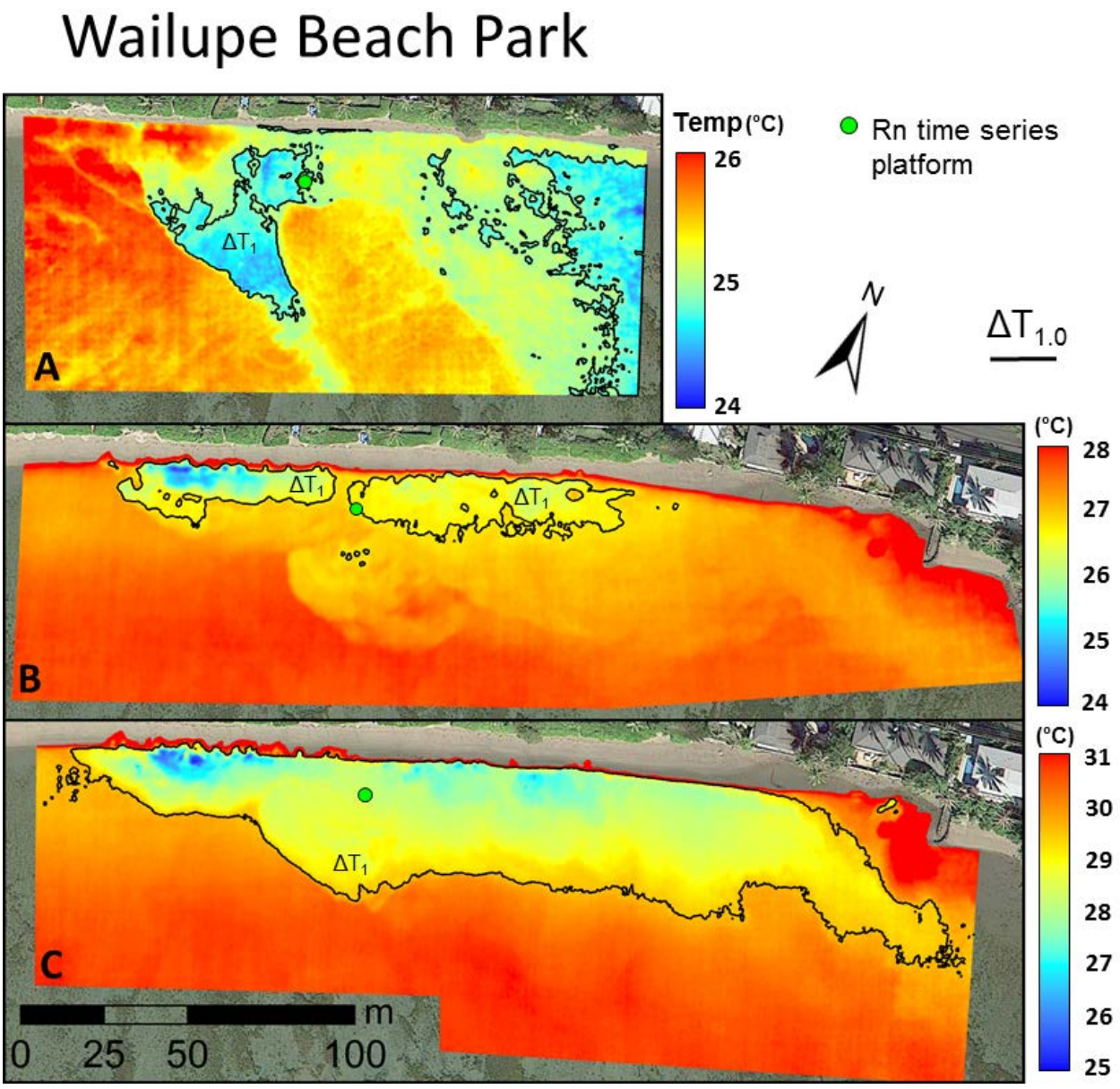

Figure 12: Wailupe Beach Park UAV-TIR imagery showing the ΔT_1 plume contour over the course of dropping tide. (A) 08:00 High tide, (B) 11:00 dropping tide, (C) 12:30 low tide.

Radon Endmember Discrete Samples

In order to quantify SGD at each study site, discrete samples were collected from the coastal sediment pore water fronting each study site to determine endmember radon activity. A total of 8 discreet samples of SGD were collected and analyzed on Maui (Table 6). Conditions at Wahikuli and

Mā‘alaea were not conducive to obtaining a reliable endmember sample due to high surf at the time of the radon time series platform deployment. In order to obtain a suitable groundwater endmember for Wahikuli, radon in water values from the time series deployment were plotted against salinity, showing a strong correlation (R^2 = 0.87) and therefore an estimated zero salinity endmember of 76 dpm/L was used as this provided the most conservative SGD estimate, as described below. One week prior to the time series deployment at Mā‘alaea, two discrete samples were collected during calm ocean conditions with ^{222}Rn activities of 365 dpm/L and 135 dpm/L. These activities were much higher than the 53.7 dpm/L sample obtained at low tide during the time series deployment at Mā‘alaea; therefore the median of the three ^{222}Rn activities (135 dpm/L) was used as the endmember. This median value agreed well with the ^{222}Rn values used for similar calculations on Maui by Bishop et al. (2015). A ^{222}Rn endmember value of 120 dpm/L was used for Wailupe Beach Park, which was obtained from previous work by Richardson et al. (2015).

Table 6: Radon endmember discrete grab sample results.

Location	Latitude	Longitude	Sample Date	Temp (°C)	Salinity	^{222}Rn in H_2O (dpm/L)
Mā‘alaea	20.793400	-156.508450	8/26/2015	26.03	4.52	365±54
Mā‘alaea	20.793400	-156.508450	8/26/2015	26.95	21.61	135±10
Wahikuli	20.896970	-156.685130	8/29/2015	27.60	31.18	26.3±13
Kihei	20.707680	-156.446230	8/31/2015	23.44	2.28	70.0±6.7
Kihei	20.707870	-156.446200	8/31/2015	25.48	5.57	91.6±26
Kihei	20.707680	-156.446230	9/1/2015	22.37	2.41	91.1±14
Mā‘alaea	20.793330	-156.508420	9/3/2015	28.50	28.72	53.7±4.2
Honolua	21.013300	-156.639360	9/5/2015	20.46	0.89	65.1±14

Radon Time Series

^{222}Rn inventory of surface water at all 5 locations generally revealed an expected inverse relationship with salinity and water depth (Figure 13). Typically, as water level falls with the outgoing tide, SGD rates increase, resulting in a corresponding drop in salinity and an increase in radon activity. Table 7 provides the average values of ^{222}Rn inventory, salinity, water depth, plume thickness, and advection rate.

Table 7: Average data values and standard deviation of the data ranges for radon inventory, salinity, water depth, plume depth and advection rate of all five research locations. The standard deviation is not the calculated error but rather characterizes the range of values observed during each sampling method.

Location	Rn Inventory (dpm/m^2)	Salinity	Water depth (m)	Plume thickness (m)	Advection rate (m/d)	Advection rate (cm/d)
Wahikuli	917±621	32.6±0.5	3.13±0.28	~0.5	0.09±0.07	8.73±7.38
Kihei	2007±1041	28.0±3.5	0.66±0.21	~0.4	0.10±0.07	9.90±7.20
Māʻalaea	8180±3439	33.4±0.8	1.34±0.17	1.34±0.17	0.19±0.16	18.9±16.1
Honolua	7710±4006	33.3±0.8	3.44±0.16	~1.0	0.34±0.28	34.5±28.2
Wailupe	4512±1329	29.8±0.8	0.40±0.14	~0.3	0.17±0.06	16.6±5.72

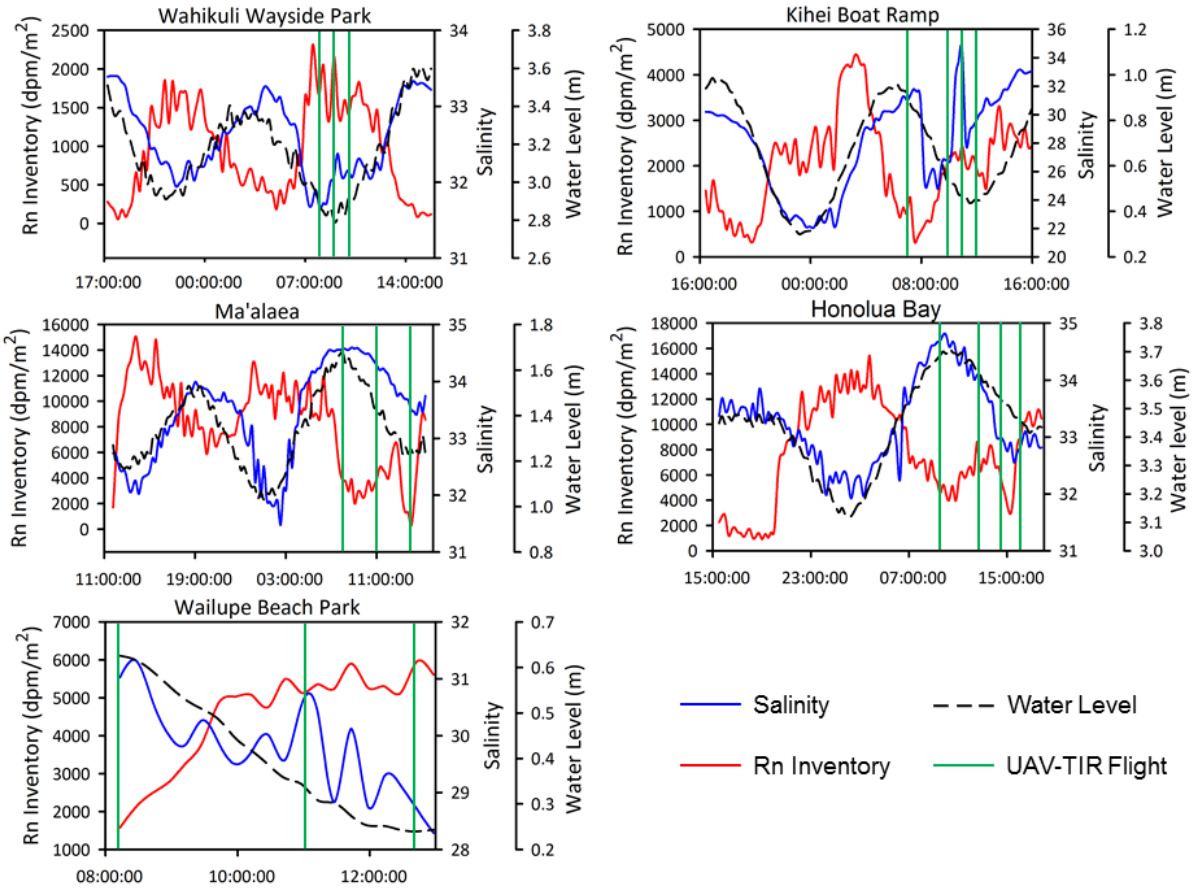

Figure 13: Radon platform time-series data showing Rn inventory, salinity, water depth and corresponding times of simultaneous UAV-TIR flights. Research occurred at each study site on the following dates. Wahikuli Wayside Park: 28 – 29 August 2015. Kihei boat ramp: 31 August – 01 September 2015. Māʻalaea: 02 – 03 September 2015. Honolua Bay: 04 – 05 September 2015. Wailupe Beach Park: 28 January 2016.

UAV-TIR area vs. SGD Rates

Relationships between SGD advection rate and the ΔT_1 surface area for each study site are shown in Figure 14. The Wahikuli Wayside Park study site did not have enough data for regression analysis, and the Mā‘alaea site had zero calculated ΔT_1 surface area during all UAV-TIR flights. Kihei boat ramp exhibited a very low correlation (R^2=0.29), however, the UAV-TIR imagery suggests that the 11:00 hr and 12:00 hr advection rates are anomalously low and are not accurately representing flux of SGD (see Discussion for more detail on this analysis). With the caveat that the number of measurements is few, data for the Honolua Bay (R^2=0.80) and Wailupe Beach Park (R^2=0.93) sites indicate positive linear correlations. The comparison of advection rate to SGD plume surface reveals that the regression lines do not pass the origin and therefore suggests that the surface area calculations are likely too conservative and/or our estimated mixing losses within the mass balance model results in advection rates that are too high.

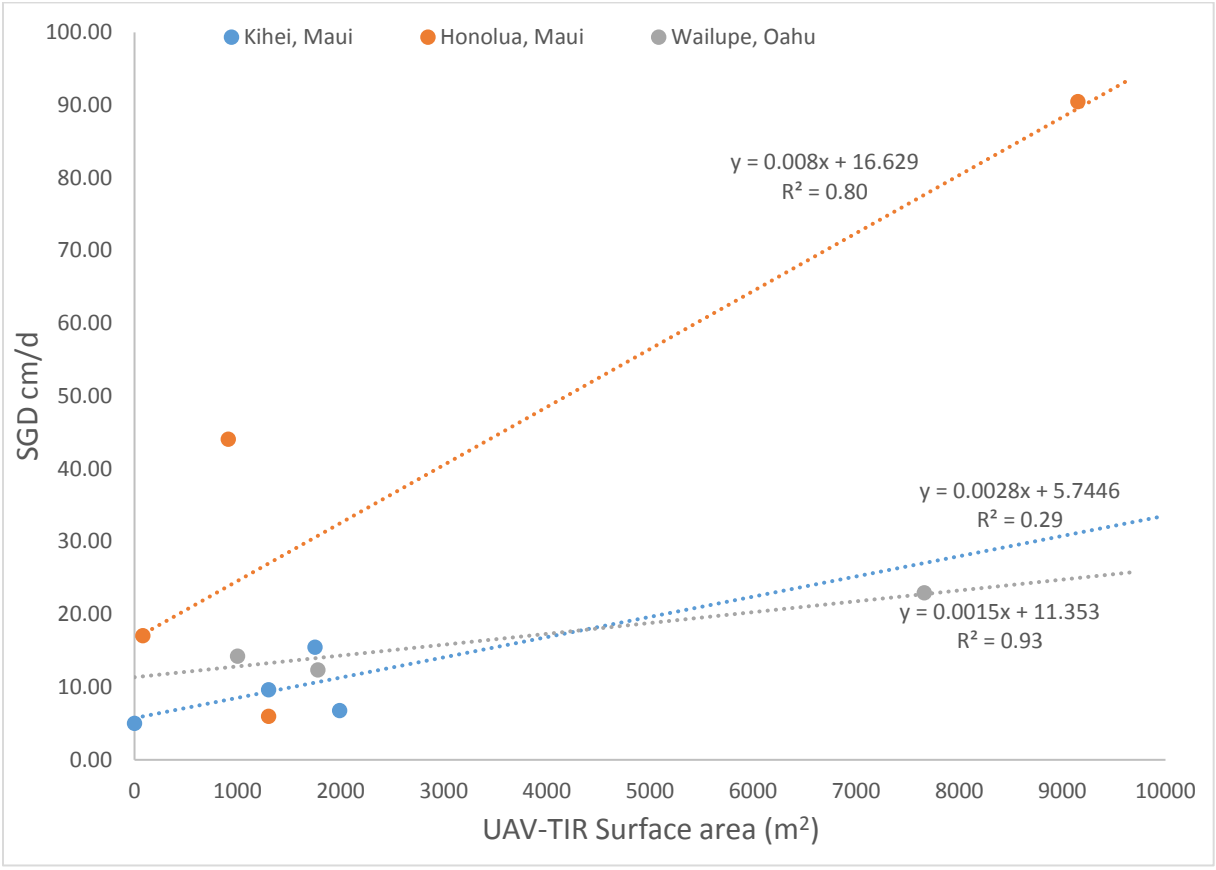

Figure 14: UAV-TIR surface area plotted against SGD advection rates. Linear regression lines are shown for the three locations that had sufficient data for regression analysis. The linear correlation between discharge rate and surface area suggests that each study site has a unique relationship that is influenced by the hydrogeologic and oceanic processes of each study site.

SGD and Nutrient Fluxes

Table 8 shows average coastal nutrient concentrations and endmember values used for nutrient flux calculations, and the calculated nutrient fluxes for each site are shown in Table 9. All coastal nutrient sample results are listed in Appendix B. High tide imagery at Wahikuli, Māʻalaea, and Kihei boat ramp did not reveal quantifiable SGD plume areas and therefore have calculated discharge rates of zero and thus no nutrient flux calculations. Honolua Bay showed the largest SGD flux of 8280 m^3/d at low tide and had the largest nutrient fluxes of all 5 sites. Wahikuli had the smallest low tide SGD rate of 31.7 m^3/d and thus it also had the smallest nutrient fluxes of all sites.

Table 8: Mean coastal surface water nutrient concentrations of each study site with standard deviation of data range (n = number of samples), and endmember sample concentrations from beach pore waters used for the nutrient flux calculations. One sample of wastewater injectate was obtained from the Lauloa condominium fronting the study site and one sample of stream water was collected at Honolua Bay for comparison purposes.

Location	n	Salinity	PO_4 (µmol/L)	Si (µmol/L)	N+N (µmol/L)
Wahikuli	6	33.6±0.5	0.23±0.05	25.1±7.91	2.36±0.93
endmember	1	32.5	0.47	57.0	6.02
Kihei	13	30.2±3.6	0.43±0.32	97.4±77.3	34.9±28.9
endmember	1	2.9	1.92	706	224
Māʻalaea	15	32.3±3.9	0.48±0.55	44.8±62.9	23.1±36.2
endmember	1	19.6	2.19	243	144
WW injectate	1	0.25	89.0	1136	1355
Honolua	7	32.5±0.5	0.22±0.02	39.3±4.71	1.78±0.3
endmember	1	0.9	1.57	688	21.5
stream	1	0.4	0.45	203	0.25
Wailupe	20	27.9±4.0	0.65±0.30	177.00±97.48	12.0±8.52
endmember	1	20.0	1.30	367	28.7

Table 9: Calculated SGD rates and corresponding nutrient fluxes with propagated error. Because the volume of SGD calculation is dependent on the determination of an SGD plume surface area, no nutrient flux calculations could be ascertained at all times indicated.

Location	Flight Time	Advection rate ($m^3/m^2/d$)	SGD Plume Area (m^2)	volume of SGD (m^3/day)	PO4 (mol/d)	Si (mol/d)	N+N (mol/d)
Wahikuli	8am	0.15±0.05	0	–	–	–	–
	9am	0.24±0.20	150±40	36±31	0.02±0.01	2.06±1.71	0.22±0.19
	10am	0.14±0.02	0	–	–	–	–
Kihei	7am	0.05±0.03	0	–	–	–	–
	10am	0.16±0.03	1750±260	272±72	0.52±0.14	192±51.1	60.7±16.9
	11am	0.10±0.04	1300±150	126±54	0.24±0.10	88.7±38.2	28.1±12.3
	12pm	0.07±0.03	1990±410	135±64	0.26±0.12	95.3±45.0	30.2±14.4
Honolua	10am	0.17±0.10	80±65	14±13	0.02±0.02	9.41±9.42	0.29±0.29
	1pm	0.44±0.08	910±270	402±142	0.63±0.22	276±97.3	8.61±3.11
	230pm	0.06±0.05	1300±300	78±74	0.12±0.12	53.8±50.4	1.68±1.58
	4pm	0.91±0.22	9150±710	8280±2152	13.0±3.43	5702±1484	178±48.3
Wailupe	8am	0.14±0.02	1000±370	143±55	0.19±0.07	52.4±20.3	4.09±1.62
	11am	0.12±0.03	1780±360	221±67	0.29±0.09	81.0±24.8	6.33±2.00
	1230pm	0.23±0.09	7660±440	1758±666	2.29±0.87	646±245	50.5±19.6

4 DISCUSSION

A/C-TIR Imagery

TIR imaging from high altitude aircraft for the purpose of imaging large stretches of coastline has proved useful for creating coastal maps of probable SGD locations. The A/C-TIR imaging flight that took place 07-08 June, 2014 on Maui revealed over 70 locations of cold-water anomalies indicative of SGD. Additionally, this information proved to be extremely informative as a reconnaissance tool as there is currently no other method capable of imaging ~100 km stretch of coast in the span of a few hours at 3.2 m pixel resolution. Although in situ temperature data loggers were used to correct SST per each flight line, an inherent limitation of this method is that due to the amount of coastline covered it is not possible to know with certainty that all observed cool water anomalies were indeed SGD, or perhaps anomalies due to other conditions such as cooler surface waters due to winds causing localized small-scale mixing, or uncertain ocean conditions such as breaking waves stirring up slightly cooler water from below. Nevertheless, this technique allows us to evaluate discharge dispersal type based on the SGD

plume appearance in the TIR imagery as well as SGD spatial distribution along large stretches of the coastline. Furthermore, regional scale TIR imagery provides the ability to determine if some areas have a higher concentration of SGD inputs into the coastal zone, which could mean a higher delivery rate of nutrients into an ecosystem.

Applications of UAV-TIR in Groundwater Discharge Research

This research has demonstrated that UAV-TIR imaging provides multiple advantageous benefits for SGD research. As illustrated in the example shown in Figure 15, the spatial resolution of UAV-TIR imagery can be extremely high, ranging from millimeters to centimeters, which can reveal SGD plume details not seen in A/C-TIR imagery. Multi-copter UAVs are capable of launching and landing within extremely confined spaces and can therefore be launched from numerous on site locations. The ability to re-launch the UAV in a matter of minutes with the change of a battery provides TIR imagery at temporal resolutions never before possible. Real-time viewing of TIR imagery further enables immediate feedback about the existence of SGD at any location, making it an ideal reconnaissance tool. Planning time is also reduced, making research missions easy and convenient to conduct with very little limitation as to weather or deployment preparation time. Because UAVs fly at low altitudes, cloud cover is not a hindrance. Furthermore, compared to TIR imagery from aircraft, TIR imagery from UAVs is extremely affordable and much safer as aircraft occupants are not involved.

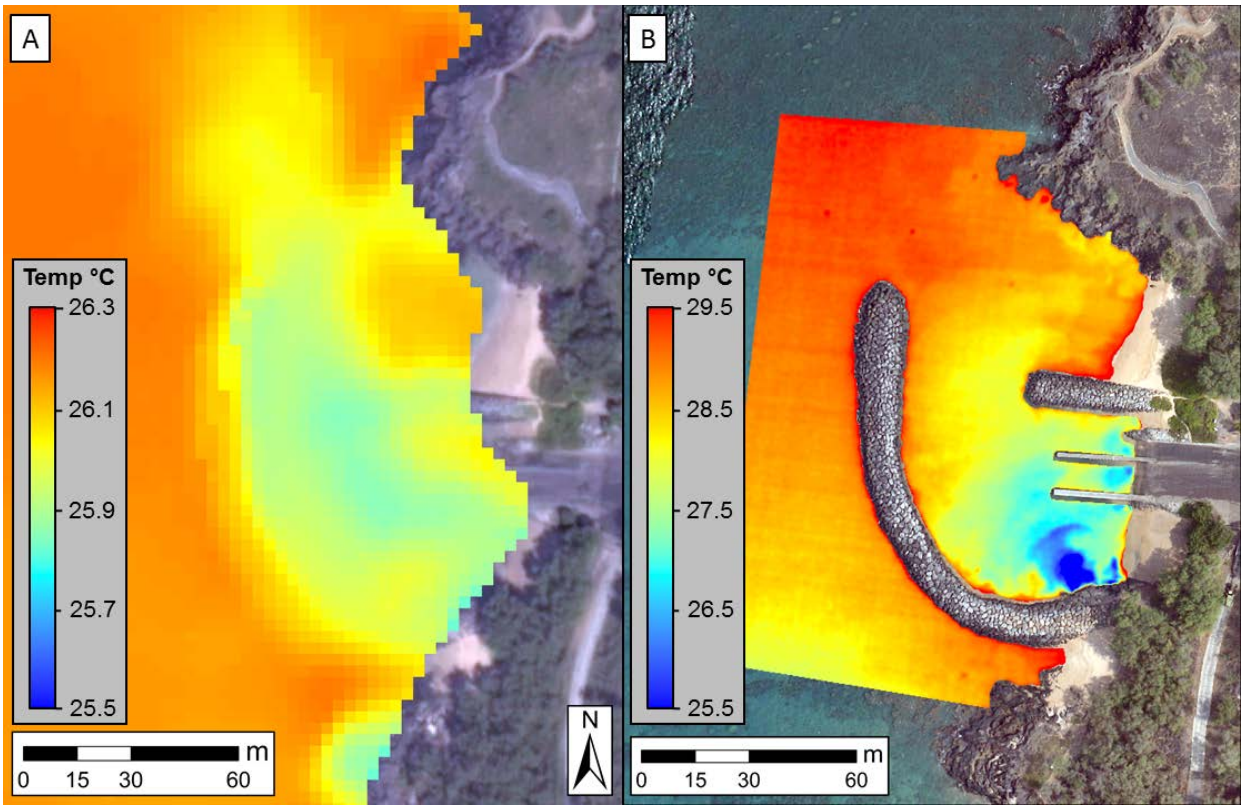

Figure 15: Comparison of TIR imagery from aircraft (A) captured on 08 June 2014 and UAV (B) captured on 01 September 2015. Both images are of the Kihei boat ramp at the same 1:800 scale.

Along with anticipated benefits of using a UAV for obtaining TIR imagery, other benefits later became evident. The capability to hover (loiter) over one location provides real-time viewing of fluid dispersal dynamics, including surface water mixing of SGD with ocean water as well as the impact of wind gusts and wind direction on SGD plume dispersal. Obtaining TIR imagery with simultaneous in situ measurements enables an entirely new method of data analysis, such as determining if radon and water quality monitoring platform placement obtains a suitably accurate representative sampling of groundwater discharge, or if variations in the areal extent of the SGD plume causes anomalously low ^{222}Rn measurements, which can then themselves be differentiated from tidally-induced SGD modulation. The high temporal resolution of UAV-TIR imaging further enables assessment of how along shore coastal extent of SGD varies with tidal changes and/or currents, which has implications on the use of radon mass balance measurement protocols, and the scaling assumptions inherent to that method. Furthermore, UAV-TIR imaging coupled with time series in situ geochemical tracer methods provides the ability to characterize the relationship between discharge rate and plume surface area at a given location, which can be used for long-term analysis, extrapolated appraisal to areas with similar hydrogeologic and oceanographic settings, and potential upscaling.

Reconnaissance UAV-TIR Imagery

The UAV-TIR Imaging method proved to be a very reliable local scale reconnaissance tool. As mentioned above, A/C-TIR imagery provides information about the location of a temperature anomaly, but could not confirm the existence of SGD. Therefore, having the ability to quickly confirm the presence of SGD with real-time viewing enabled quick determination of a location's viability as a research site. Wahikuli Wayside Park was one of such locations. A/C-TIR imagery revealed the presence of a subtle temperature anomaly at this location, however, due to the relatively low resolution of the image, it was uncertain if the anomaly was SGD or runoff from nearby drainage culvert. The reconnaissance UAV-TIR flight immediately identified the SGD plume and revealed the exact location of discharging groundwater with no temperature anomaly visible within the vicinity of the drainage culvert. Along with confirming SGD, the UAV-TIR reconnaissance also provided the spatial information about where to best deploy a time series radon platform in order to best monitor point source SGD.

UAV-TIR Imagery vs In Situ Geochemical Data

A key assumption inherent to stationary time-series monitoring of ^{222}Rn is assuming that the time-series radon platform is located where it will sample water that is representative of the overall discharge area. In locations with broad diffuse discharge, location of the radon platform is not as critical as in places where point source discharge is the primary dispersal type. This became evident at Wahikuli Wayside Park as this area was impacted by a south swell during the deployment period which had implications on where the radon time-series platform could be placed. Due to the intermittent swell, the radon platform was anchored further offshore than initially planned and was thus likely outside of the SGD plume. It was therefore not known how the platform placement would impact surface water measurements of ^{222}Rn due to unknown plume dispersal dynamics. Despite near shore mixing due to breaking waves, the radon data were elevated above ocean baseline levels and showed a clear inverse relationship with water level and salinity (Figure 13) indicating that SGD was detected. The UAV-TIR imagery (Figure 9B), however, clearly showed that even during maximum discharge at low tide the platform location is outside of the ΔT_1 plume boundary and thus the time series platform was only detecting diluted amounts of SGD. The implication of this is that the advection rates reported by the radon mass balance underestimated true rates of SGD. This example illustrates that UAV-TIR imagery can be used to determine if the use of the geochemical tracer method captured a representative sample of SGD and whether or not the calculated flux rates are representative of the area.

In similar fashion to the above-described scenario, another aspect of having time series UAV-TIR imagery is the ability to compare unexpected in situ measurement-derived SGD deviations from typical tidally driven SGD trends with UAV-TIR imagery. For example, Santos et al. (2009) reported anomalous SGD tracer concentrations that did not follow expected trends and thus, they could "only speculate about its causes." Similar anomalous measurements were observed here. For example, a notable deviation from typical SGD trends occurred at Kihei boat ramp approximately two hours before low tide. Radon inventory, and thus advection rates, peaked two hours before low tide, followed by a subsequent decline to anomalously low ^{222}Rn concentrations at low tide when ^{222}Rn concentration should have likely been at its highest based on expected trends (Figure 13). In this case, the UAV-TIR imagery revealed that shifts in the plume's geometry, and not decrease in SGD, was most likely causing this decrease in ^{222}Rn concentration. UAV-TIR imagery from the 10:00 hr flight shows the time-series radon platform intake location well within the ΔT_1 contour at this time (Figure 10B). However, the following two UAV-TIR imaging flights (Figure 10C & 10D) reveal that the intake location was bordering the ΔT_1 contour and thus was sampling water of lower ^{222}Rn concentration which translates into lower calculated SGD fluxes despite Figure 10D revealing the largest plume of the imaging period.

Changing spatial extent of SGD

One of the assumptions that we wanted to address with time-series UAV-TIR imaging was monitoring how the discharge locations of SGD vary over the course of a tidal cycle. Current geochemical tracer mass-balance methods necessitate the need to determine the extent of coastline where SGD occurs in order to calculate a volumetric flux. Due to varying hydrogeological settings, it is to be expected that this will vary depending on location and thus greatly impact geochemical tracer mass-balance calculations. UAV-TIR imagery comparisons of Kihei boat ramp and Honolua Bay during falling tide illustrate this well. UAV-TIR time-series imagery at Honolua Bay shows a clear increase in plume size with falling tide, but more importantly, an associated expansion of the along shore coastal extent of SGD as well (Figure 11). The high tide plume size at Honolua Bay was approximately 80 m^2, while the low tide plume surface area was two orders of magnitude greater at over 9000 m^2 (Table 4). This translates into an increase in SGD flux rate at Honolua Bay of approximately 400 fold, from ~20 m^3/d to ~8300 m^3/d. In contrast, the Kihei boat ramp site is a location where SGD primarily discharges from extremely restricted basalt rock conduits and thus imaged plume size did not have a large along shore variance. Although plume surface area was zero at high tide, all other tidal stages had a relatively small range of approximately 1300 to 2000 m^2 (Table 3). One unique aspect that became evident at Kihei boat ramp is

that the high tide water level appeared to almost entirely suppress all SGD as no plume was evident in the high tide imagery (Figure 10A). However, one aspect that became evident during this experiment is that SST were generally cooler during early morning UAV-TIR flights, which decreased the surface water thermal contrast, thus masking the presence of a cooler SGD surface water layer.

TIR area vs. SGD rates

Aerial TIR imaging of SGD has introduced the possibility of using SGD plume surface areas to extrapolate discharge rates to other areas based on the relationship between discharge rate determined using an independent method (in this study the radon mass balance approach) and plume surface area. Previous research (Johnson, 2008; Danielescu et al., 2009; Kelly et al., 2013; Tamborski et al., 2015) has shown that a correlation between SGD rates and plume surface area does exist. Based on the slope of the regression line, this correlation appears to be unique for each location in the literature though it could also be impacted by the different SGD quantification methods used in each study. Johnson (2008) calculated total SGD using a modified LOICZ-style mass-balance approach (Gordon et al., 1996). Danielescu et al. (2009) acquired discharge rates of point source near-shore springs through the use of a portable flume using the method of Bos et al., (1984). Kelly et al. (2013) calculated volume of SGD by multiplying the advection rates of SGD by the plume surface area using the same radon mass-balance approach of this paper. This particular method may be inherently biased however in that the volumetric discharge calculation is dependent on the very surface area that it is being compared to. Tamborski et al. (2015) calculated volume of diffuse SGD using coastal radon surveys following the work of Dulaiova et al. (2010).

Because the surface area expression of an SGD plume depends on buoyant fresher water floating on top of the denser more saline water, the dynamic processes that control the flow of SGD will play a role in the appearance of the plume. Of the different forcing mechanisms which impact groundwater flow into the coastal zone, the most important factor is the hydraulic gradient of the aquifer (Heiss and Michael, 2014), which can fluctuate on a seasonal scale. The flow rate of groundwater induced by the hydraulic gradient is further complicated by the conductivity, heterogeneity, anisotropy and dispersivity of the media through which it travels, thus determining the dispersal type, whether point source and/or diffuse flow (Roper et al., 2014). Furthermore, once the flow of groundwater reaches the land-water boundary, it is then subject to the effects of ocean conditions such as currents, waves and wind which can impact the mixing of discharging groundwater (Roper et al., 2014) as well as the dispersal pattern of a buoyant SGD plume (Jurisa and Chant, 2013). These dynamic hydrogeologic

and oceanographic processes impart variability to the surface area expression of SGD, thus complicating the determination of a correlation between discharge rate and plume size of any one specific location if they are not constant.

In spite of the aforementioned complex processes that can impact SGD plume dynamics, the research noted above has shown that a correlation does exist and once this correlation is established, it is then possible to make general estimates of discharge rates based on the surface area of an SGD plume at a location that is determined to be of a similar setting, thus allowing aerial TIR imaging to be a stand-alone method for SGD quantification. One major caveat to this concept is that the comparison of surface area to discharge rate in each of the above-mentioned studies has only been done once and therefore it is not known how the correlation will compare over time. Along with this caveat, another hindrance to extrapolating TIR imagery to other locations is the varying nature of the hydrogeologic and oceanographic processes of one location to another that can impact the surface area expression of an SGD plume, especially within settings that are as diverse as the Hawaiian Islands. An example of this is shown in Figure 16 where the research presented here is contrasted with data from Tamborski et al. (2015). The relationship between surface area and discharge rate of the 5 study sites presented in this paper do not show any cohesive correlation, most likely because all five study sites have very different hydrogeologic and oceanographic settings. Further study of these relationships clearly demands future work.

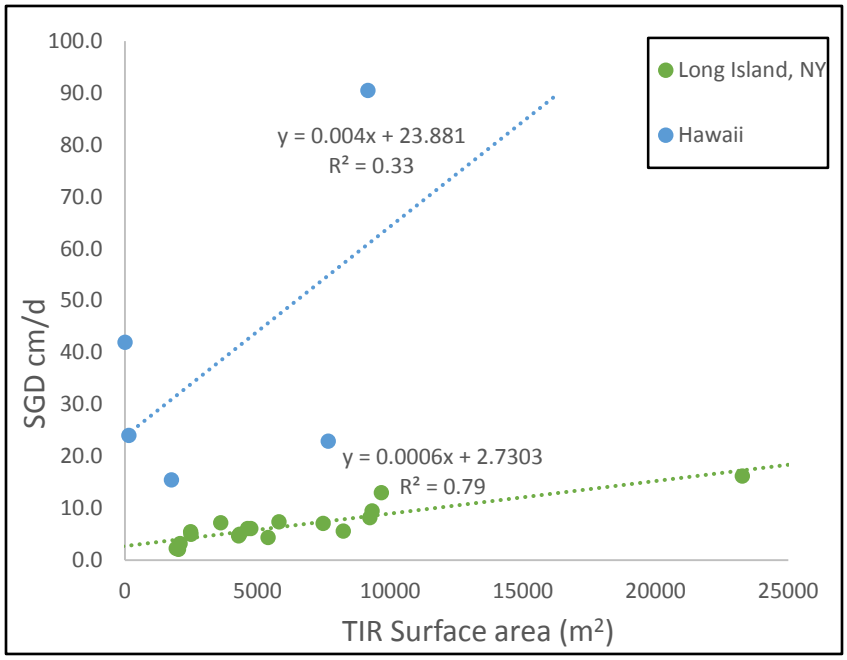

Figure 16: Low tide SGD rates plotted against low tide TIR surface area of this study and data from Tamborski et al. (2015). The low correlation (R^2=0.33) of the Hawai'idata reveal the range of diverse hydrogeologic and oceanographic processes that impact the relationship between surface area and discharge rate. The data from Tamborski et al. (2015), however, show a strong correlation (R^2=0.79) even though the 18 different plumes are from a variety of locations, suggesting that all the study sites of Tamborski et al. have very similar settings.

Comparison of Coastal Nutrient Concentrations and Fluxes

Long-term benthic monitoring studies have shown up to a 67% decrease in the coral cover of observed reefs surrounding the island of Maui over the past 10-15 years (Ross et al., 2012), and numerous past studies have also suggested that Maui's coastal ecosystem problems, particularly the prevalence of macroalgae, may likely be linked to elevated nutrient concentrations entering the coast by way of SGD (Soicher and Peterson, 1997; Hunt and Rosa, 2009; Dailer et al., 2010; Glenn et al., 2012, 2013; Bishop et al., 2015; Amato, 2015). Nutrient results (Table 8) are compared in Table 9 to previously reported nutrient concentrations on Maui and nutrient flux calculations from this study are compared with previously published results from throughout the Hawaiian Islands in Table 10. The Hawai'i fluxes in Table 10 were compiled by Bishop et al. (2015) with all values normalized to per meter of shoreline. It is highly noteworthy that the calculated discharge rates of the research presented here compared well with SGD rates calculated in previous research throughout the State of Hawai'i, confirming the validity of combining UAV-TIR with time-series radon monitoring.

Kihei Boat Ramp

Discharging groundwater nutrient concentrations at Kihei boat ramp were unexpectedly high, with N+N concentration matching groundwater from a well sampled by Hunt and Rosa (2009) that was determined to be down gradient of the Kihei Wastewater Reclamation Facility (WWRF). Endmember concentration of N+N at the Kihei boat ramp was 224 µmol/L while the well sampled by Hunt and Rosa (2009) was 229 µmol/L. This was unexpected due to the fact that the Kihei Boat ramp is located 2 km south of the modeled plume of groundwater determined to be impacted by injected effluent from the Kihei WWRF. Based on the findings of Bishop et al. (2015) the most probable cause of the elevated nutrients are due to the high density of on-site disposal systems (OSDS) of the area as there is no agricultural land up-gradient of the study site. Both SGD rates and nutrient fluxes calculated for Kihei boat ramp are very similar to those calculated by Bishop et al. (2015) for Kū'au, Maui (Table 10), where the primary contributor for elevated nutrient fluxes at Kū'au was determined to be due agricultural land use.

Mā'alaea

The lack of SGD as visible by UAV-TIR prevented the calculation of SGD rates or nutrient fluxes for Mā'alaea. However, sampled groundwater endmember nutrient concentrations at this site (Table 9) are indicative of anthropogenic impact. While endmember nutrient concentrations collected at Mā'alaea were much lower than those collected by Bishop et al. (2015), the high salinity of the

endmember sample was indicative of dilution by seawater. The average normalized nutrient concentration of all samples collected at Māʻalaea, however, compare well to the endmember samples obtained by Bishop et al. (2015). Normalized N+N concentration for this study was 301 µmol/L while the work of Bishop et al. (2015) reported 291 µmol/L. One unique aspect of the Māʻalaea area is the existence of multiple small-scale wastewater injection wells from some of the condominiums. A sample of the wastewater injectate was obtained from one of the condominiums (Table 9). Despite the presence of the local wastewater injection wells, the work of Bishop et al. (2015) determined that the most likely sources of elevated nutrients in SGD in the area were due to fertilization of large tracts of sugarcane surrounding the study site.

Honolua Bay

The Honolua Bay site was the only study location representative of an area with minimal human impact. The majority of land use in the area is undeveloped land with some former pineapple agriculture (Bishop et al., 2015). Endmember nutrient concentrations were relatively low with a normalized N+N concentration of 21.0 µmol/L and a sampled endmember N+N concentration of 21.5 µmol/L, which was slightly lower than the N+N concentration of 29 µmol/L obtained by Bishop et al. (2015). Average calculated SGD rates at Honolua Bay were the greatest of all 5 research sites of this study, however these SGD rates also revealed the widest range of discharge from a minimum of 0.5 m^3/m/d at high tide to a maximum of 46.0 m^3/m/d at low tide. The average SGD rate of 9.5 m^3/m/d for this study was slightly higher than the 5.9 m^3/m/d calculated by Bishop et al. (2015) and within the range of that determined by Street et al. (2005).

Wahikuli Wayside Park

The Wahikuli Wayside Park site was directly down gradient from a neighborhood that was determined to be of high OSDS density by Bishop et al. (2015). SGD at this location was the most difficult to sample due to the rocky terrain with no obvious SGD conduits along with high surf impacting the shoreline. Normalized nutrient concentration revealed an N+N concentration of 88.8 µmol/L, indicative of anthropogenic impact. Due to the high surf and with the radon time series platform located outside of the SGD plume (Figure 9), discharge rates were lowest of all 5 study sites, with an average SGD rate of 0.2 m^3/m/d. The discharge rate is also the lowest calculated SGD rate of all previous research within the state of Hawaiʻi, further confirming the impact the high surf event had on the quantification of SGD at this location.

Table 10: Coastal endmember nutrient concentrations from each study site, averaged nutrient concentrations of all samples collected at each site normalized to freshwater salinity concentrations, and corresponding nutrient concentration samples from other studies if collected near the study site of this work.

Location	type	Salinity	PO_4 (µmol/L)	Si (µmol/L)	N+N (µmol/L)
Wahikuli	endmember	32.5	0.47	57.0	6.02
	normalized	0.2	4.69	687	88.79
Kihei	endmember	2.9	1.92	706	224
	normalized	0.2	3.06	740	253
	*WW well	1.65	6.01	–	229
Māʻalaea	endmember	19.6	2.19	243	144
	normalized	0.2	5.86	577	301
	WW injectate	0.25	89.0	1136	1355
	**endmember	1.5	7.2	611	291
Honolua	endmember	0.89	1.57	688	21.5
	normalized	0.2	2.16	577	21.0
	**endmember	0.86	1.80	473	29
	stream	0.38	0.45	203	0.25
Wailupe	endmember	20.0	1.30	367	28.7
	normalized	0.2	3.21	636	72.9

*Hunt and Rosa, 2009

**Bishop et al., 2015

Table 11: SGD rates and nutrients fluxes normalized to per meter of shoreline for comparison of this to study to past studies in Hawai'i.

Location	Total SGD ($m^3/m/d$)	Total PO_4^{3-} (mmol/m/d)	Total Si (mmol/m/d)	Total N+N (mmol/m/d)
Wahikuli, Maui [a]				
Avg	0.2	0.1	11	1.2
max	1.0	0.5	59	6.2
min	–	–	–	–
Kihei, Maui [a]				
Avg	6.3	12	4450	1408
max	6.8	13	4803	1520
min	–	–	–	–
Honolua Bay, Maui [a]				
Avg	9.5	15	6531	204
max	46.0	72	31670	987
min	0.5	0.9	376	12
Wailupe, O'ahu [a]				
Avg	3.4	4.4	1240	97
max	8.4	11	3072	240
min	1.02	1.3	374	29
Kuau, Maui [h]	4.4	19	3345	1660
Mā'alaea, Maui [h]	11	50	4220	2072
Kahului, Maui [h]	1.5	2.8	745	42
Waiehu, Maui [h]	0.8	2.5	283	18
Honomanu, Maui [h]	3.3	10	1952	21
Honolua Bay, Maui [h]	5.9	9.1	2390	145
Honolua Bay, Maui [e]	2.5-21	1.2-8.7	–	6.2-72
Kahana, Maui [e]	4.2-11	3.6-9.0	–	144-360
Kahana, Maui [e]	250-530	200-430	–	8220-18000
Kahana, Maui [b]	35-113	–	–	1968
Mahinahina, Maui [e]	3.5-10	3-7.5	–	1840-6650
Honokowai, Maui [e]	2.7-7.2	0.5-9.0	–	54-153
Kahekili, Maui [f]	21-55	90-1400	6980-32000	1400-4700
Kahekili, Maui [g]	6-92	–	–	–
Hanalei, Kauai [d]	3.7-11	1.0-3.0	169-361	20-73
Haena, Kauai [d]	1.8-3.8	0.8-0.9	207-259	6.4-26
Kiholo, Hawai'i [c]	34.0	150	24900	6400

a This study
b Paytan et al. (2006)
c Johnson (2008)
d Knee et al. (2008)
e Street et al. (2008)
f Swarzenski et al. (2012)
g Glenn et al. (2012, 2013)
h Bishop et al. (2015)

5 CONCLUSIONS

The use of high altitude A/C-TIR imaging is a proven and reliable method for detecting the location of groundwater inputs into the coastal zone and determining the dispersal type, whether of point source and/or diffuse flow. Its primary strengths lie in its ability to use thermal contrasts in SST to map the areal extent, size and nature of discharging groundwater over large areas of coastline. Logistical limitations of A/C-TIR include operational costs, which usually limit its use to single-pass "snap shot" surveys, the inability to image through cloud cover, and typical flight altitudes of 1000 m - 2500 m, which limit pixel resolution to ~ 0.5 to 3.5 m, respectively. The A/C-TIR flight of the western half of the island of Maui provided regional scale imagery with a pixel resolution of 3.2 m, revealing approximately 70 temperature anomalies indicative of SGD over approximately 100 km of coastline. We additionally used in situ ^{222}Rn mass balance method for quantifying localized discharge rates and associated nutrient fluxes as well as providing detailed time-series information about the variability of SGD. Time-series radon measurements on Maui and O'ahu proved effective in providing high resolution discharge rates of SGD at all five locations within a variety of oceanographic and hydrogeologic settings. Limitations of time-series radon monitoring, however, are that it requires assumptions to be made about areal extent of SGD in order to obtain a volumetric flux. These two primary methods – A/C TIR imaging and radon tracer – each on their own accord have inherent limitations, but when coupled together with simultaneous time-series UAV-TIR imaging and time-series radon monitoring, all three complement each other well, creating a robust research method that can help eliminate many assumptions and elucidate the variability of coastal SGD fluxes. UAV-TIR real-time viewing provides valuable feedback, allowing for quick and rapid accurate assessment about the existence and extent of SGD at any given location. UAV-TIR imaging also reveals the exact location of the SGD plume in relation to the time-series radon platform, eliminating the need to assume a constant surface area through which nutrient rich groundwater is discharging into the coastal zone, and allows for highly improved and exacting determinations of SGD rates and nutrient fluxes. Furthermore, the use of time-series UAV-TIR imaging provides imagery at unprecedented temporal resolution that can provide information about SGD plume spatial dynamics that may be used to constrain and differentiate variations in flow.

APPENDIX A

Processed aircraft thermal infrared imagery of Maui are provided in the appendix as panels. All imagery was collected overnight on 7-8 June 2014 with the specific time range listed for each panel in the caption along with the map scale used. All panels are projected in Universal Transverse Mercator (UTM) zone 4 using the WGS-84 datum. The temperature ramps were adjusted to maximize contrast within each panel. The GIS stream location data layer of perennial and non-perennial streams was obtained from the State of Hawai'I Office of Planning GIS database which was sourced from DLNR Division of Aquatic Resources. The panels begin at Pā'ia and move counter-clockwise around the island where they end at Cape Kina'u. Any break in the imagery was due to cloud cover and therefore no data exists for those areas. Imagery was collected on a falling tide with high tide at Kahului, Maui occurring at 21:54, 7 June 2014 and low tide occurring at 05:06, 8 June 2014, based on tide observations from National Oceanic and Atmospheric Administration tide gauge 1615680.

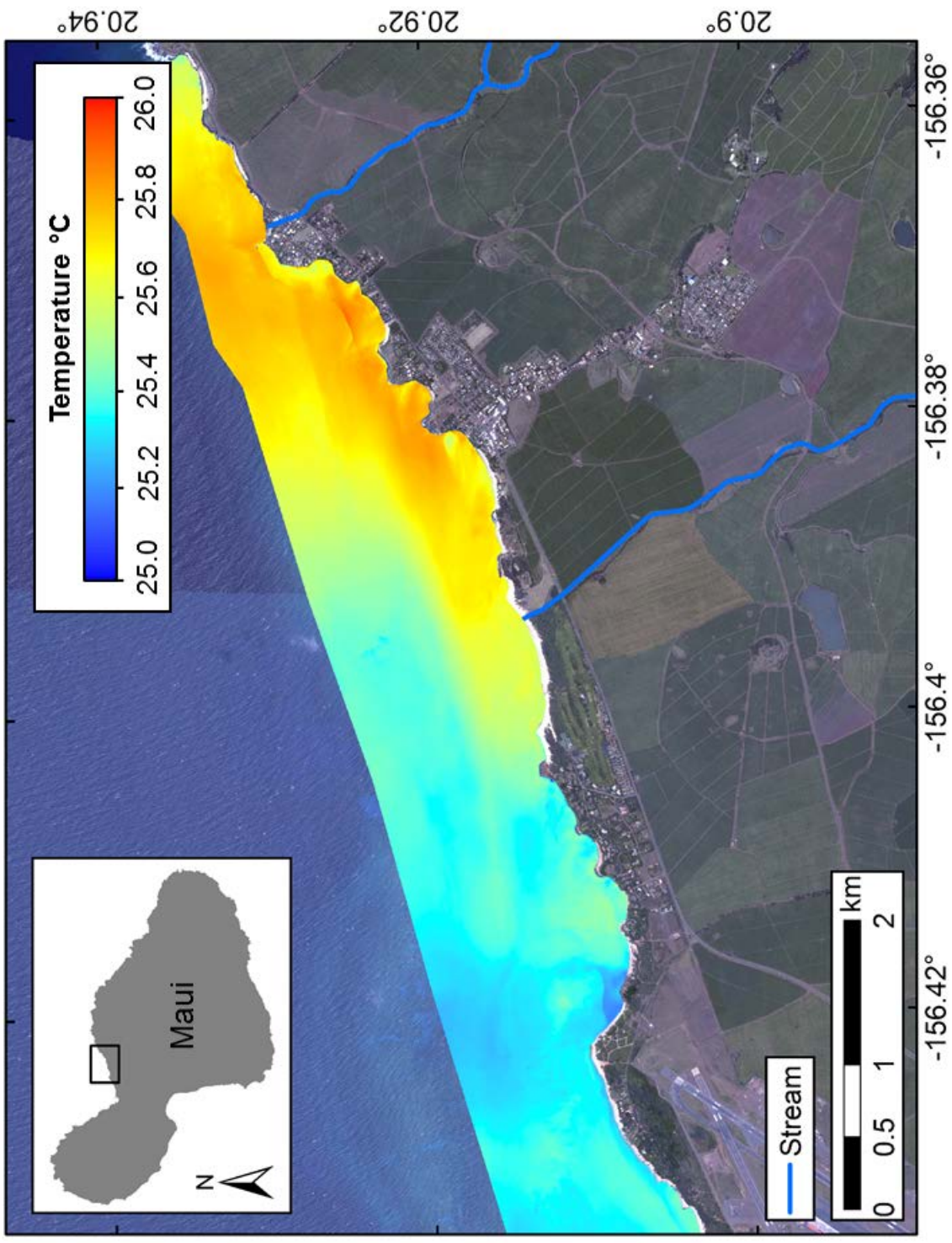

Panel 1: Pāʻia to Papaʻula Point, 7 June 2014, 22:03-22:06 HST (scale 1:31,000). Blue line representing stream in panel only indicates stream bed location which is likely dry.

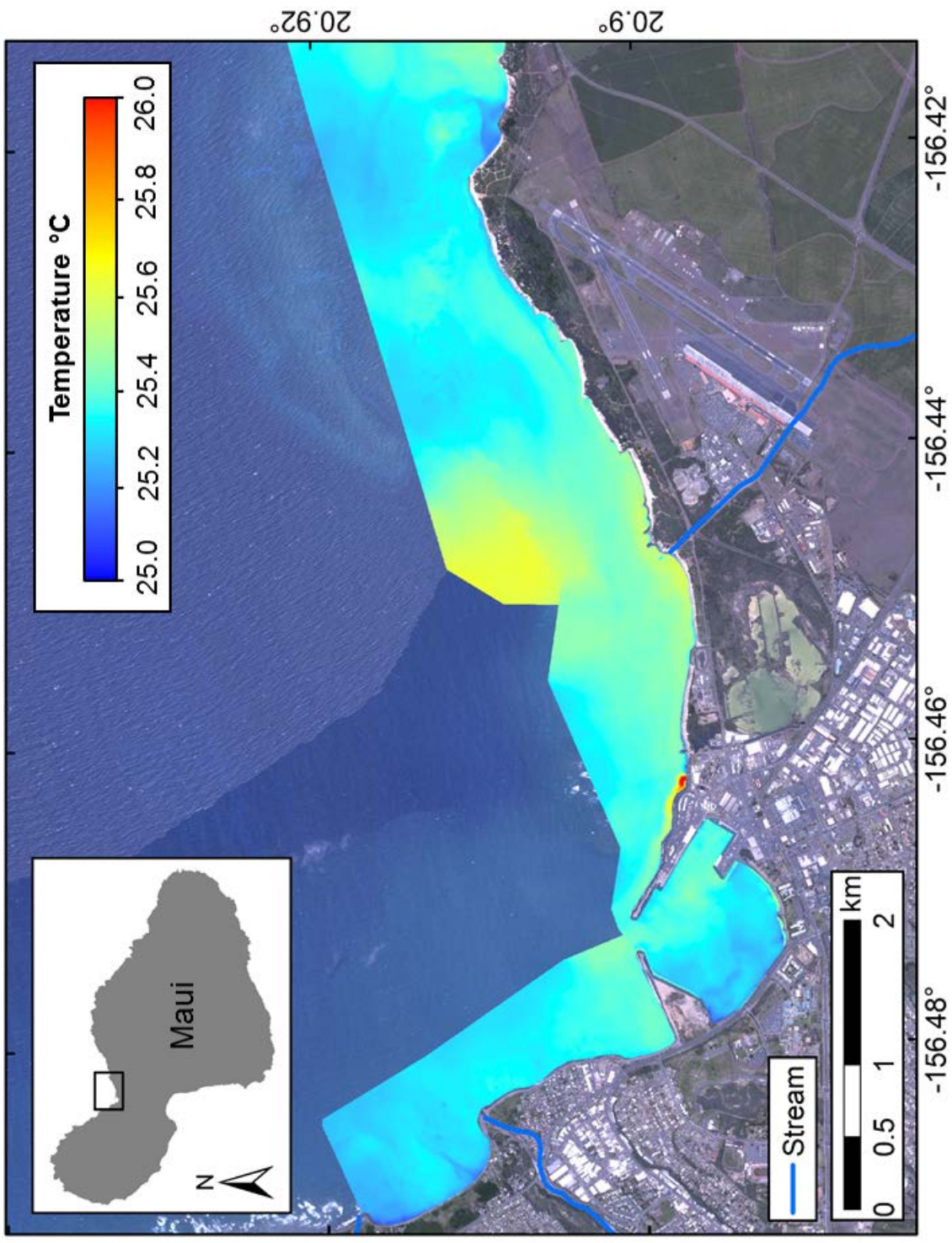

Panel 2: Papa'ula Point to Kahului, 7 June 2014, 22:03-22:28 HST (scale 1:31,000). Blue line representing stream in panel only indicates stream bed location which is likely dry.

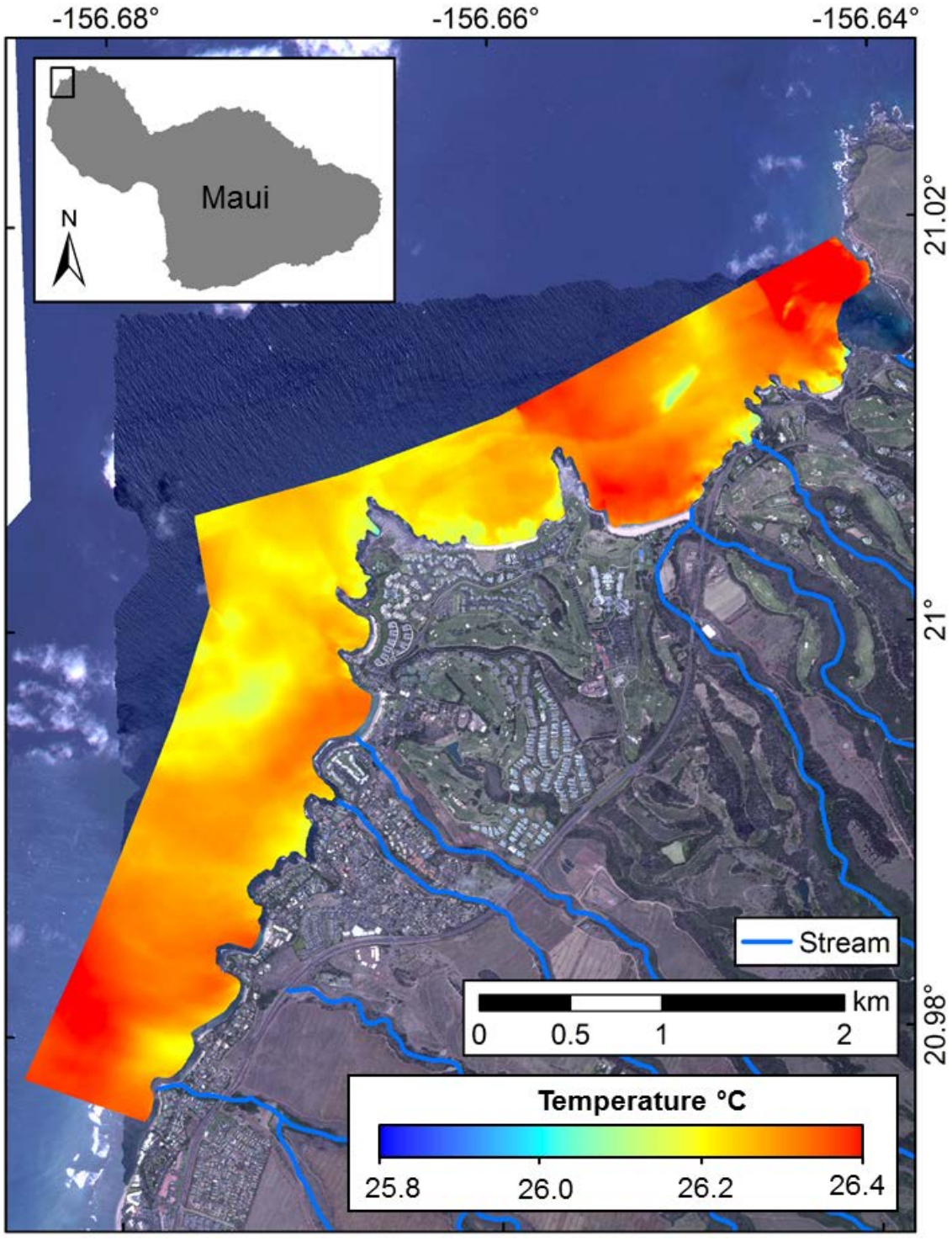

Panel 3: Nāpili, 7 June 2014, 22:51-22:54 HST (scale 1:24,500). Blue line representing stream in panel only indicates stream bed location which is likely dry.

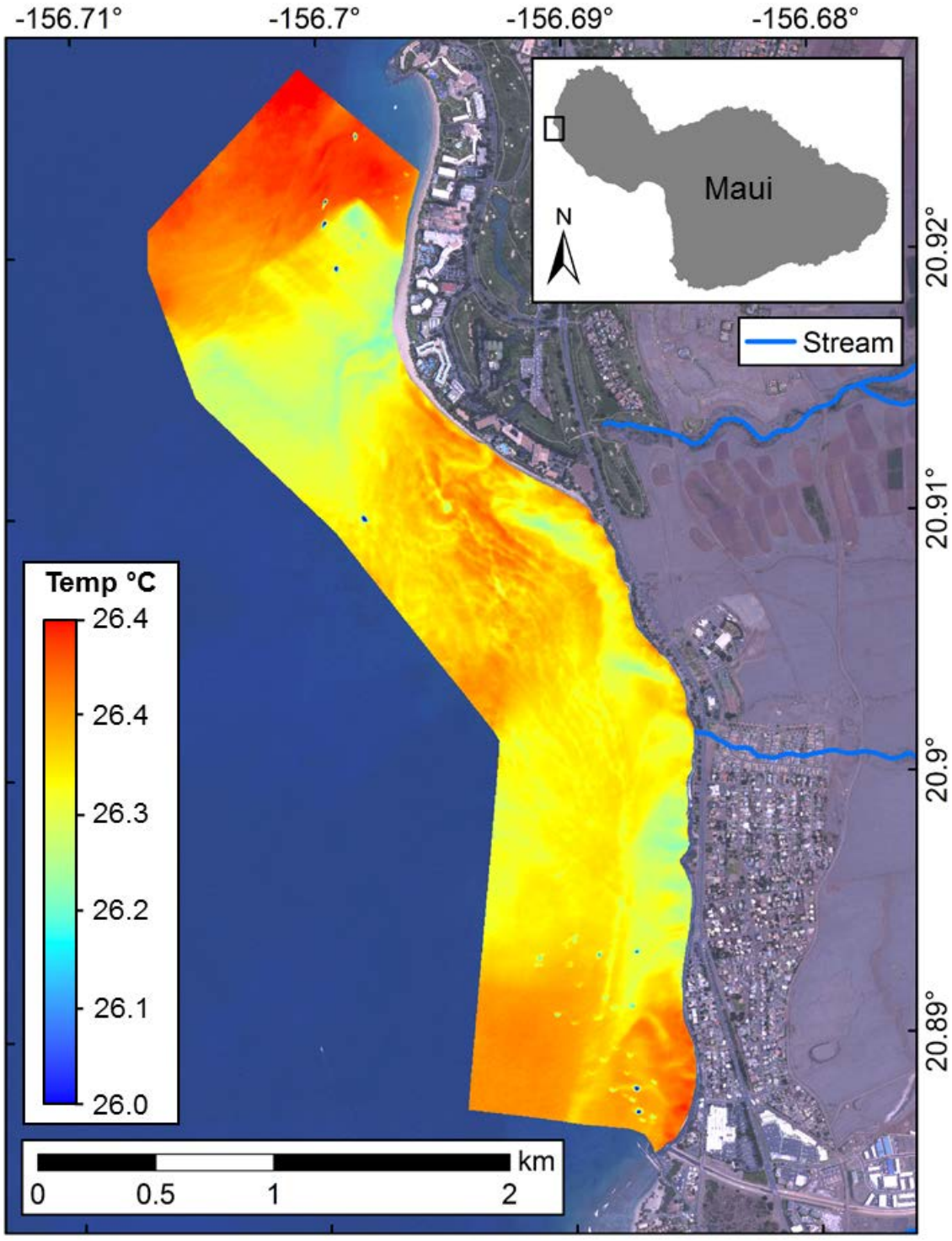

Panel 4: Kā‘anapali to Wahikuli, 7 June 2014, 23:36-23:42 HST (scale 1:19,000). Blue line representing stream in panel only indicates stream bed location which is likely dry.

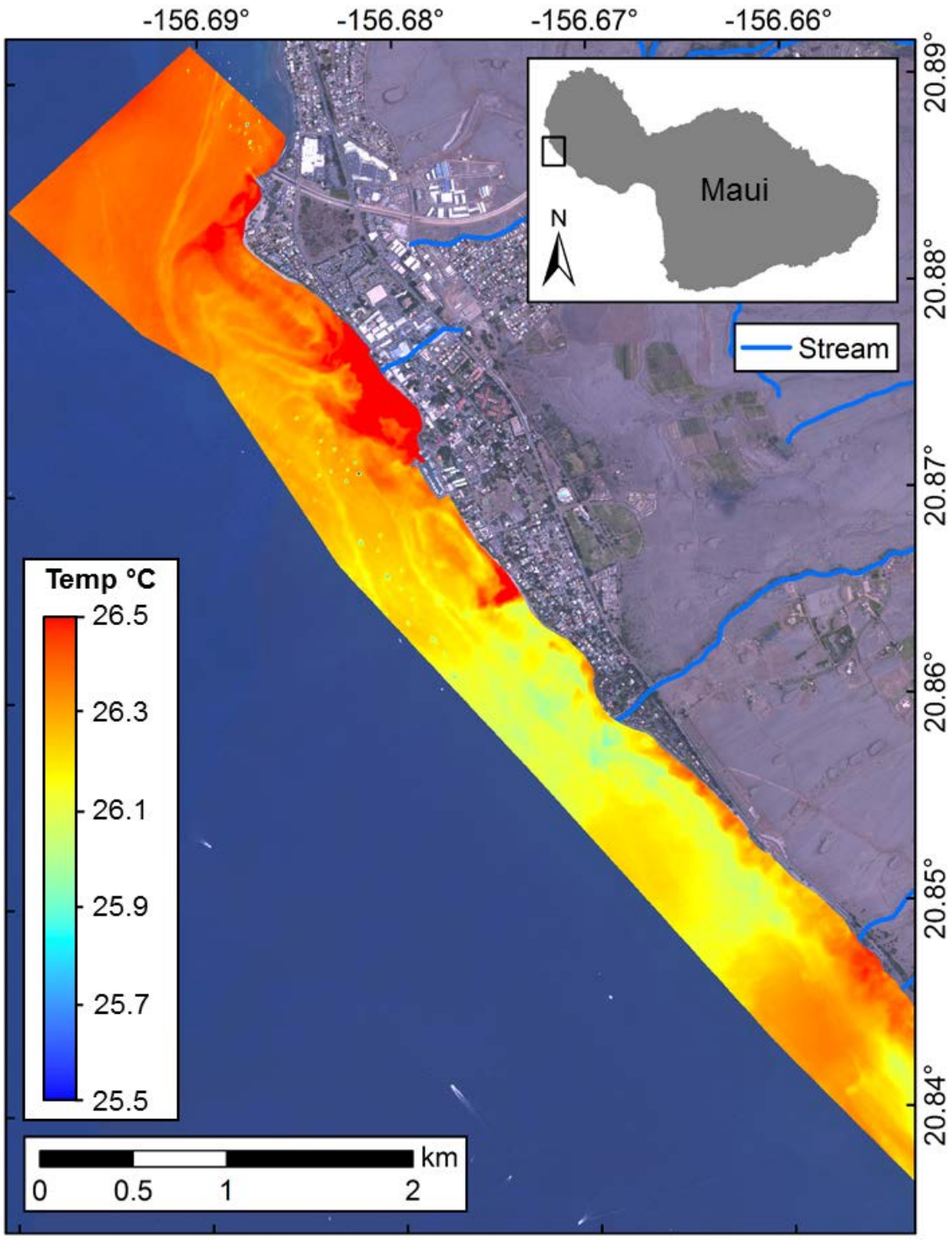

Panel 5: Lahaina, 7 June 2014, 23:43-23:47 HST (scale 1:24,000). Blue line representing stream in panel only indicates stream bed location which is likely dry.

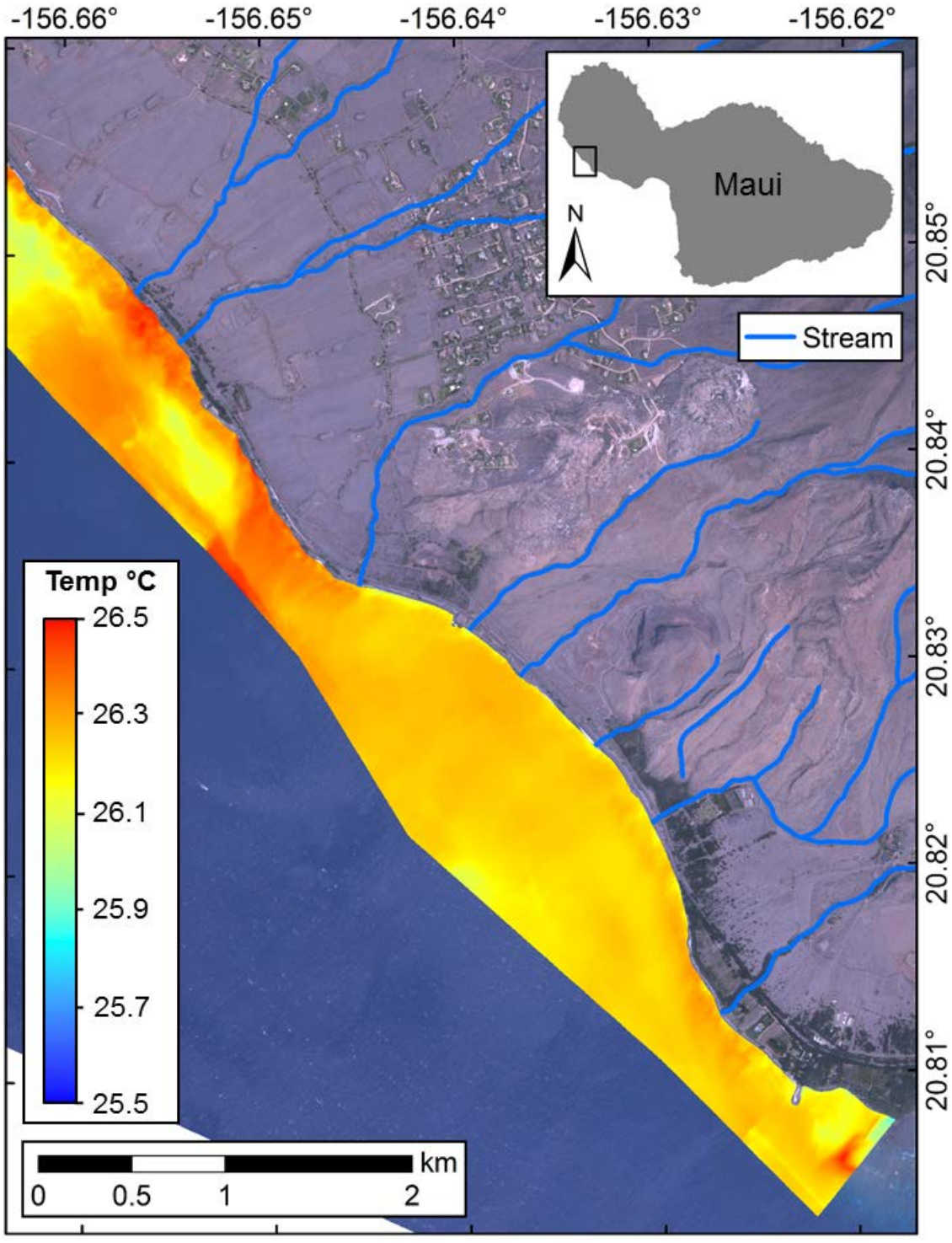

Panel 6: Launiupoko to Olowalu, 7 June 2014, 23:43-23:47 HST (scale 1:24,000). Blue line representing stream in panel only indicates stream bed location which is likely dry.

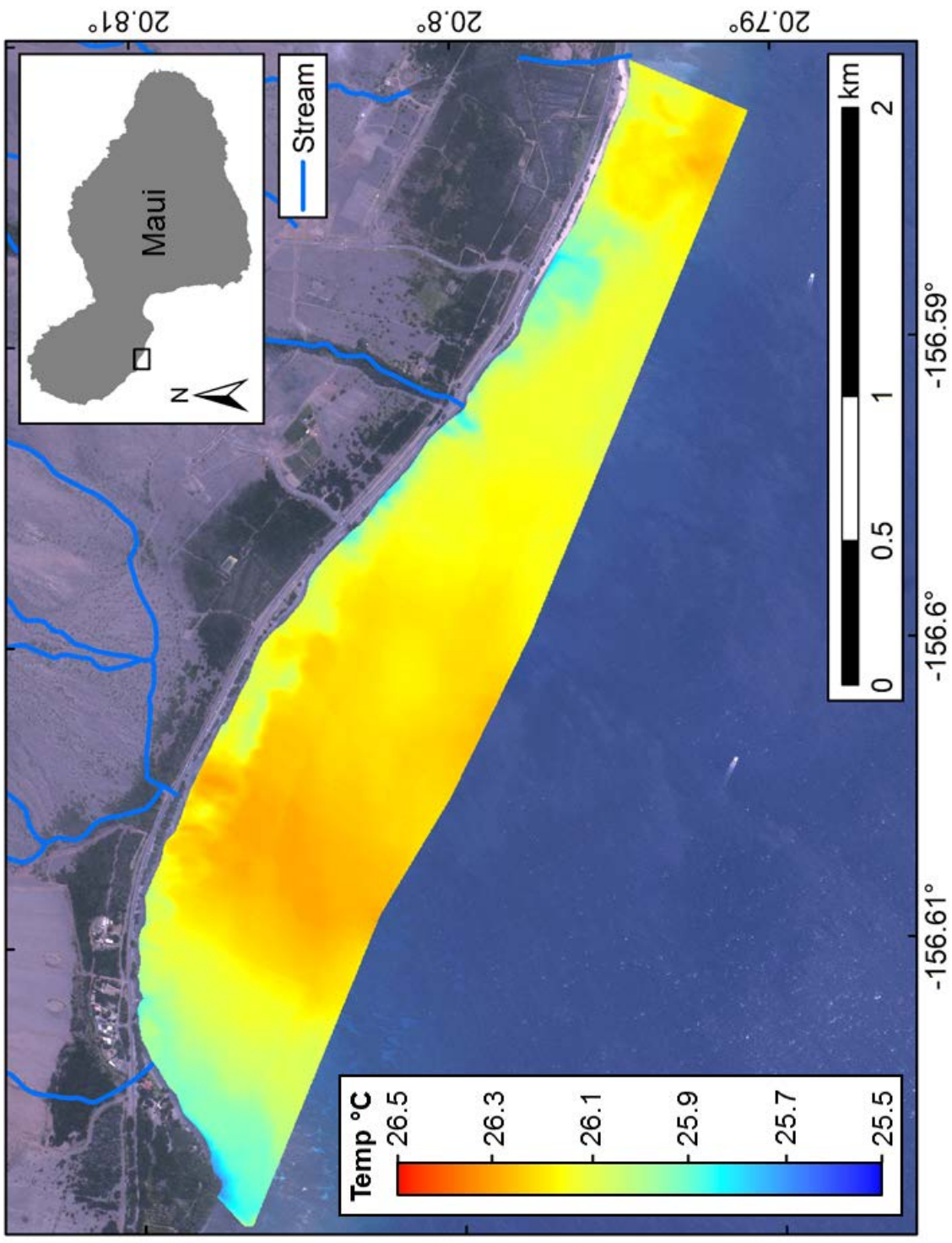

Panel 7: Olowalu to Ukumehame, 7 June 2014, 23:54-23:57 HST (scale 1:15,500). Blue line representing stream in panel only indicates stream bed location which is likely dry.

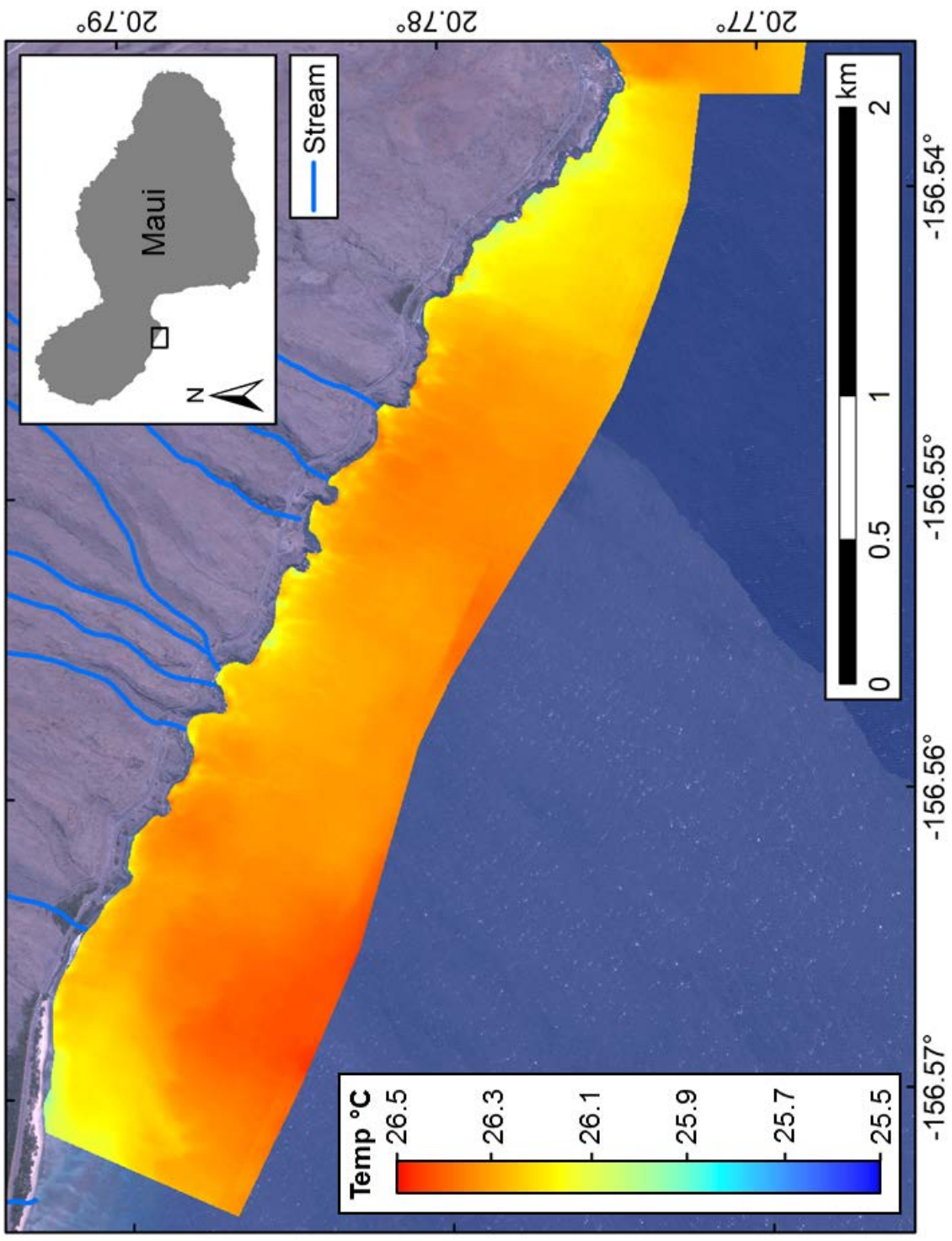

Panel 8: Pāpalaua State Wayside to Papawai Point, 7 June 2014, 23:54-23:57 HST (scale 1:15,500). Blue line representing stream in panel only indicates stream bed location which is likely dry.

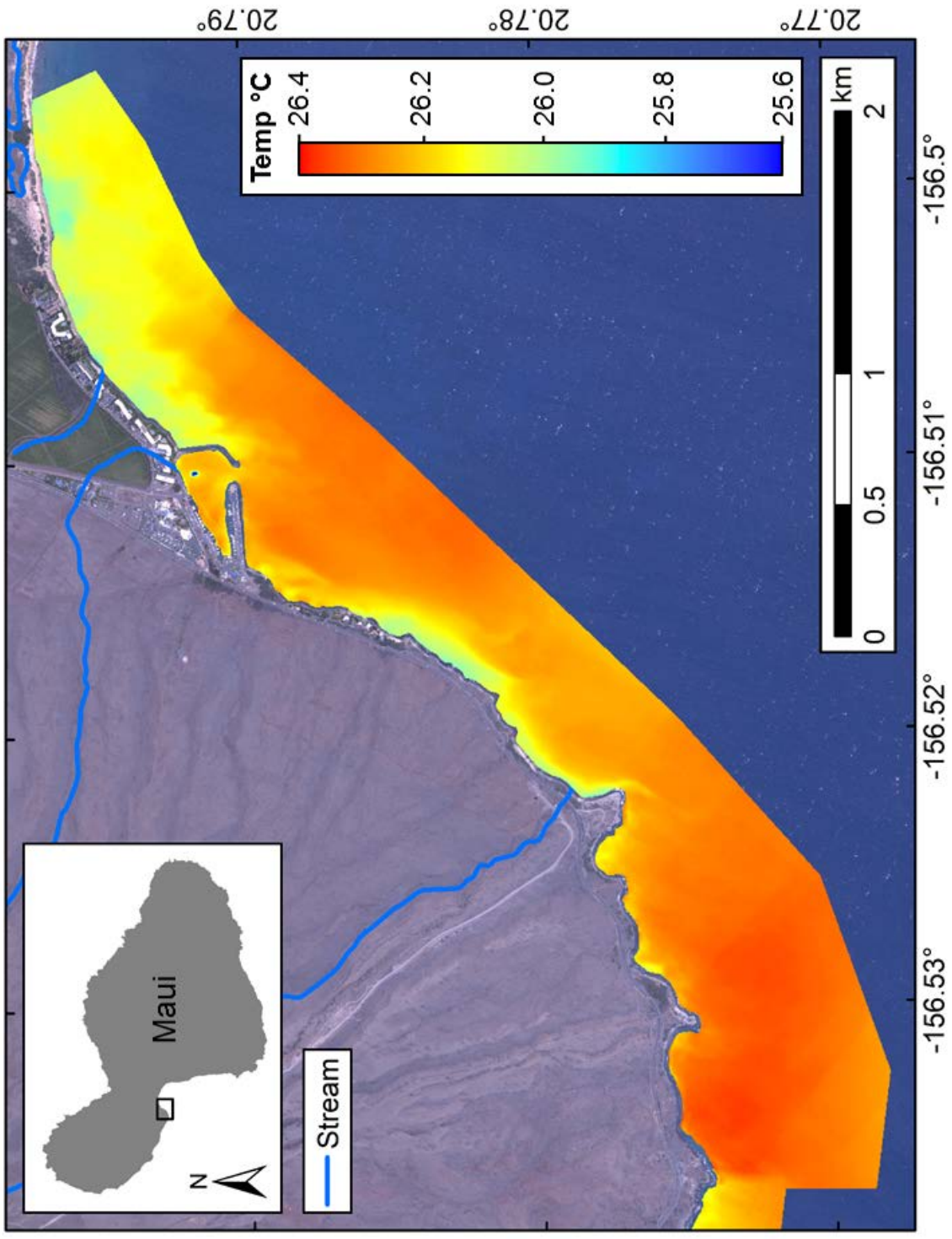

Panel 9: Papawai Point to Mā'alaea, 8 June 2014, 00:04-00:06 HST (scale 1:17,000). Blue line representing stream in panel only indicates stream bed location which is likely dry.

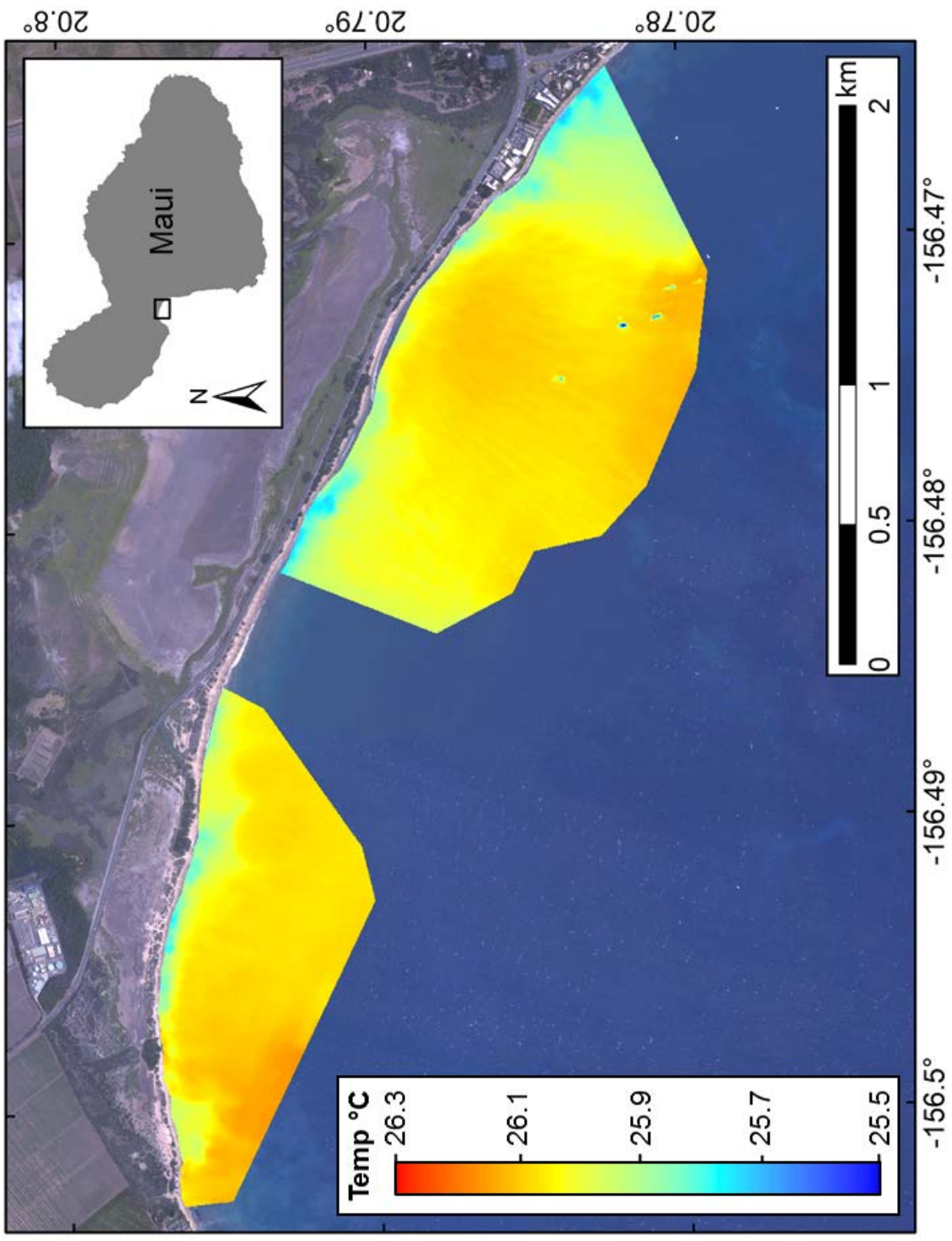

Panel 10: Māʻalaea to North Kihei, 8 June 2014, 01:09-01:11 HST (scale 1:16,000).

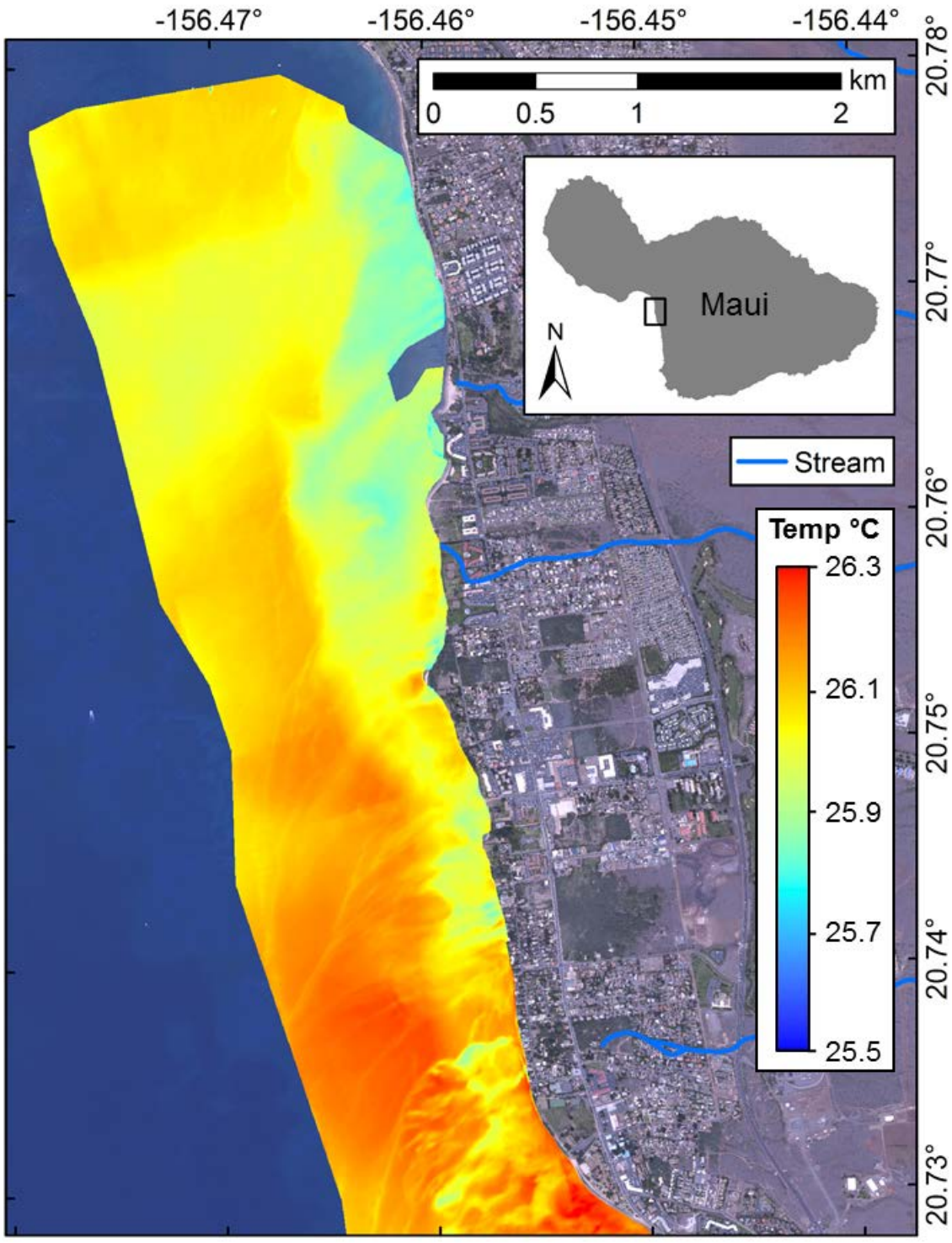

Panel 11: North Kihei, 8 June 2014, 00:15-00:19 HST (scale 1:22,000). Blue line representing stream in panel only indicates stream bed location which is likely dry.

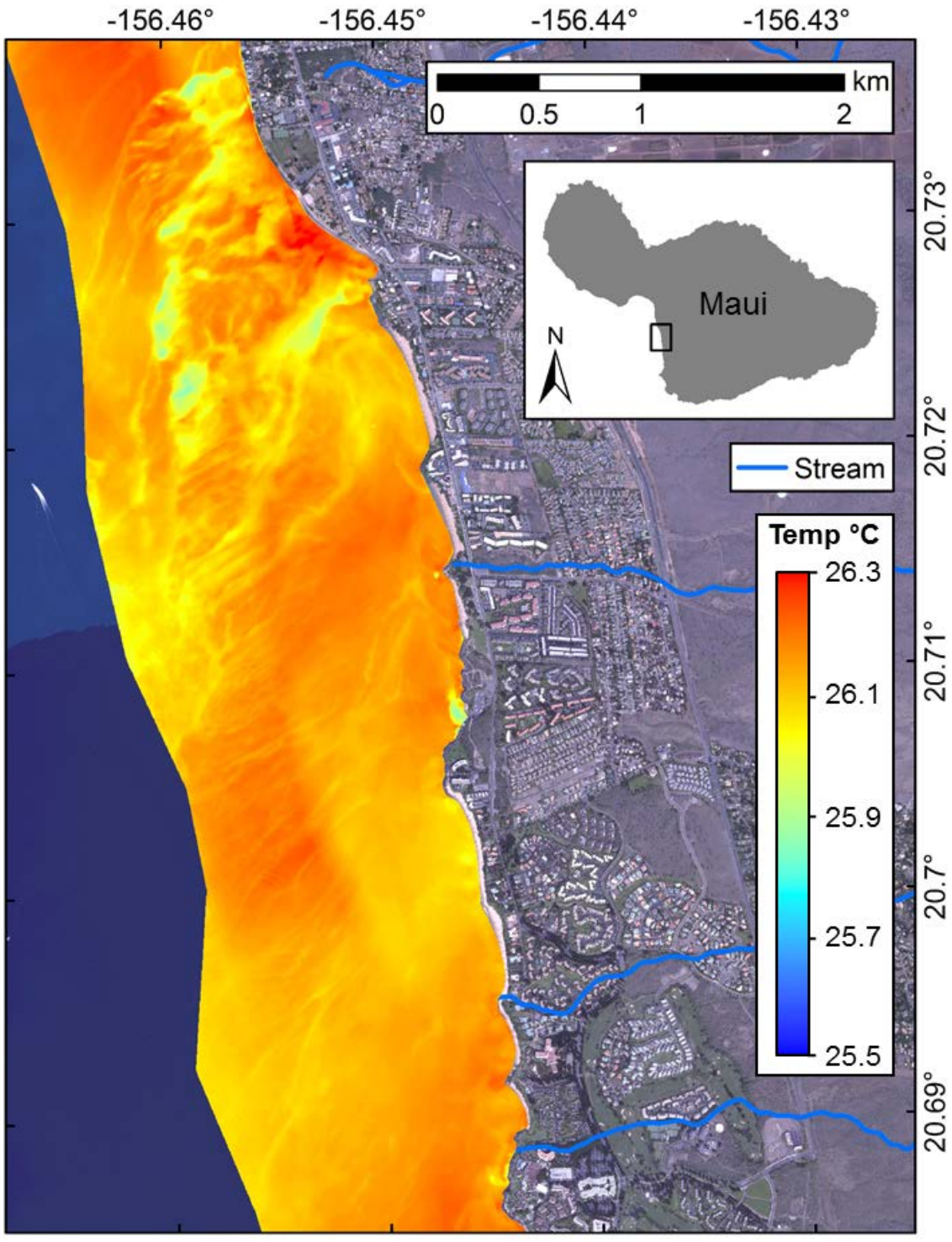

Panel 12: South Kihei, 8 June 2014, 00:15-00:19 HST (scale 1:22,000). Blue line representing stream in panel only indicates stream bed location which is likely dry.

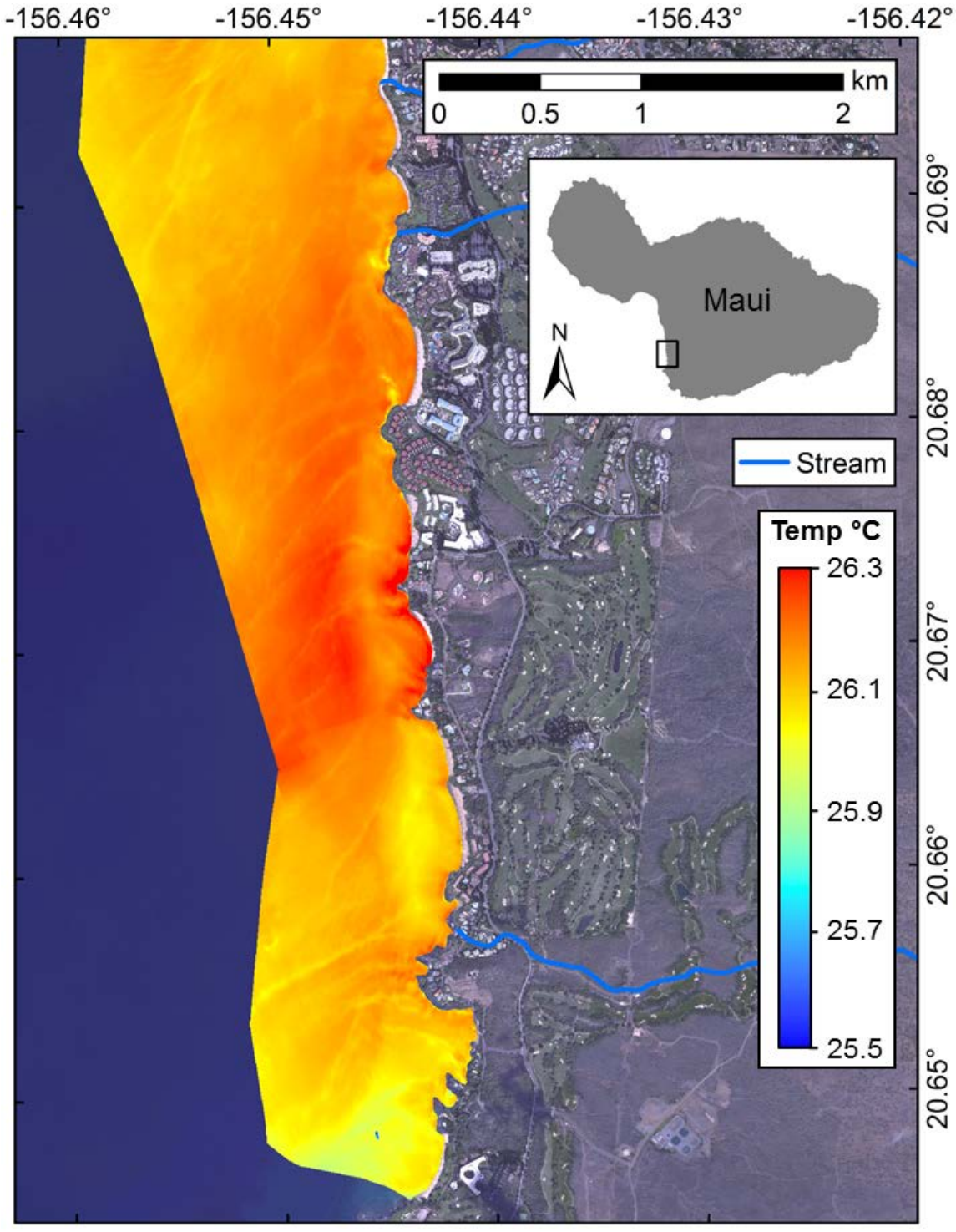

Panel 13: Wailea, 8 June 2014, 00:15-00:19 HST (scale 1:22,000). Blue line representing stream in panel only indicates stream bed location which is likely dry.

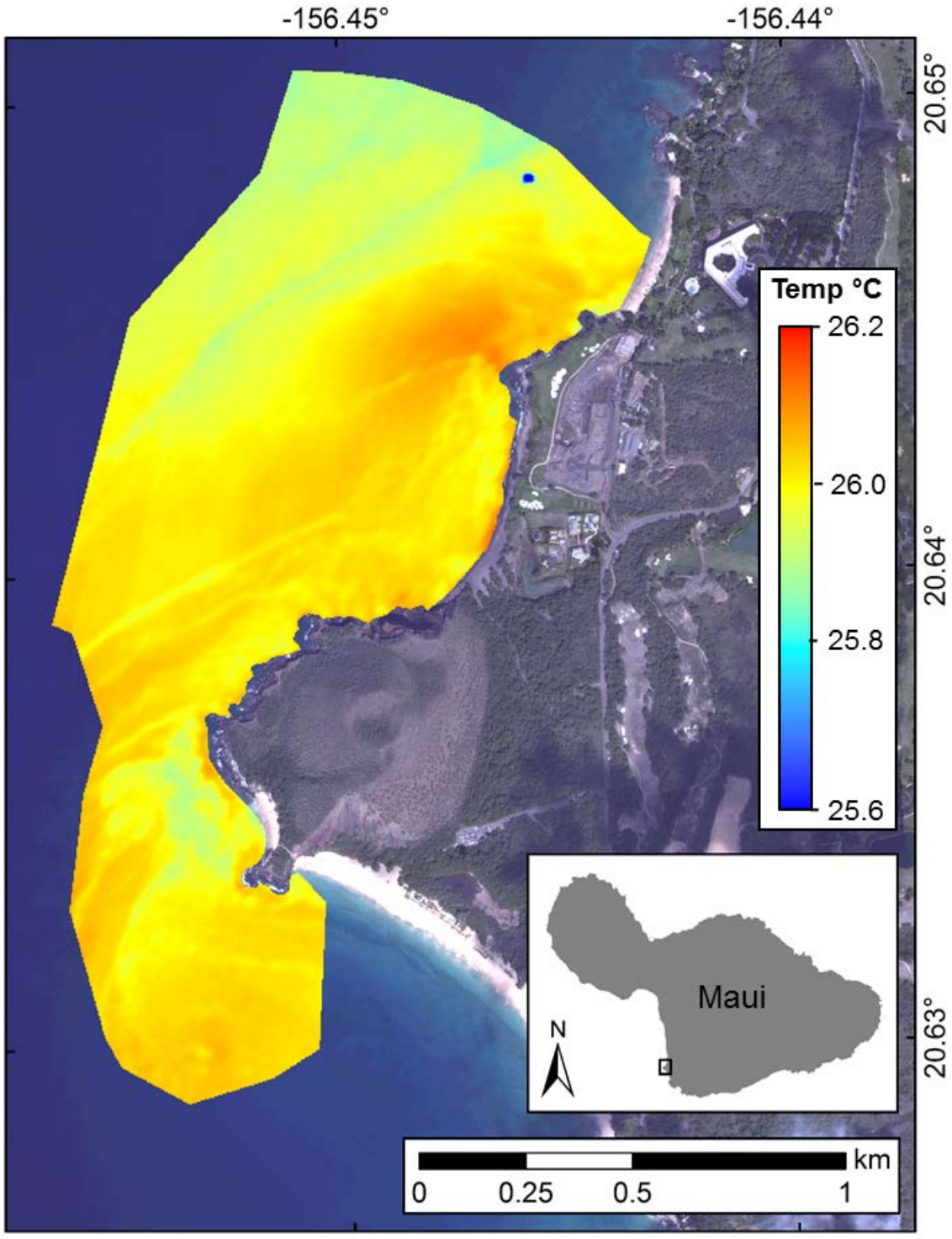

Panel 14: Mākena, 8 June 2014, 00:42-00:44 HST (scale 1:10,500).

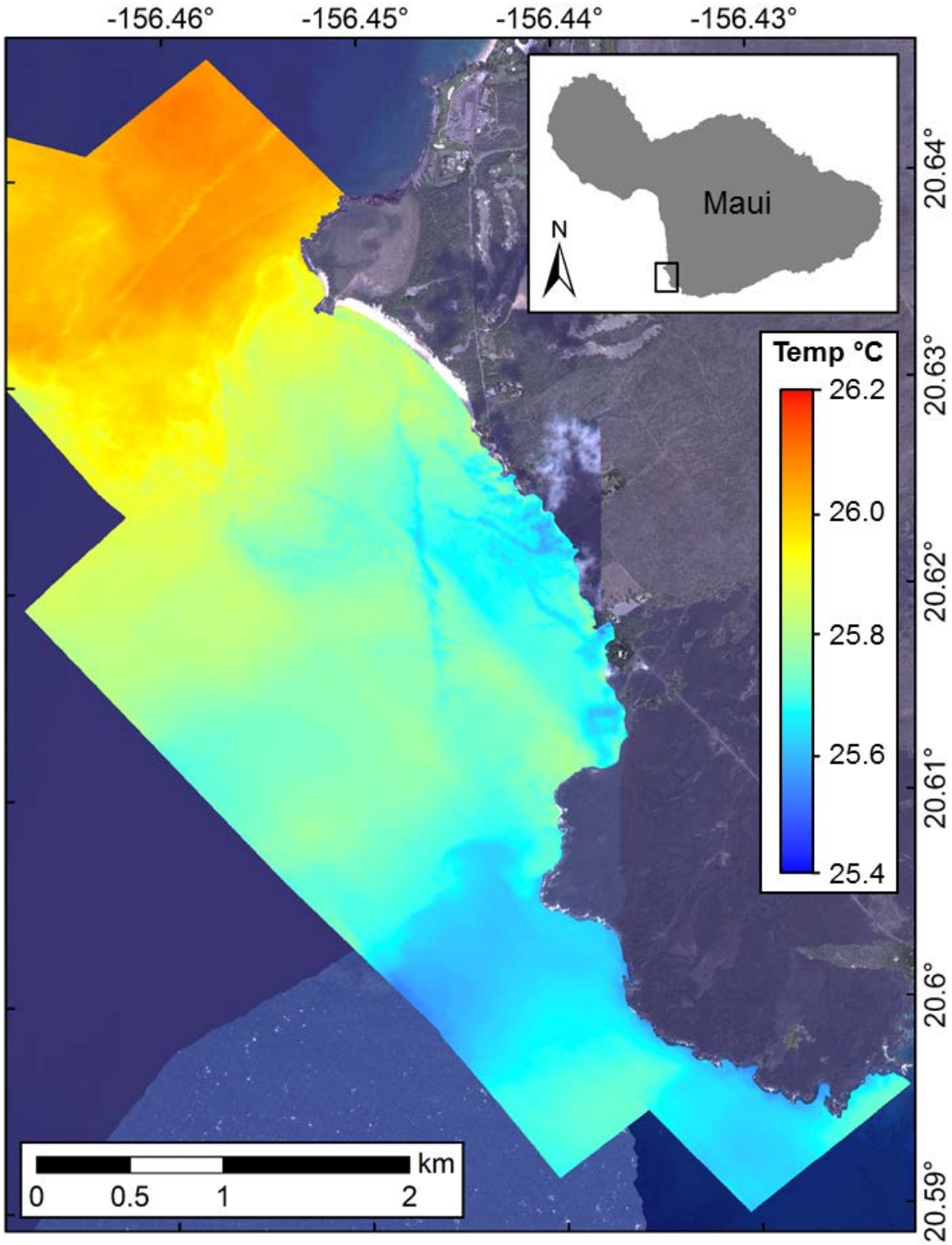

Panel 15: Āhihi Bay, 8 June 2014, 00:56-01:02 HST (scale 1:24,000).

APPENDIX B

Coastal nutrient samples from specified research location listed in the caption with each table showing sample name, date collected, time collected (HST), latitude and longitude of exact sample location, salinity, and dissolved inorganic nutrient concentration in µmol/L of phosphate, silicate, nitrate plus nitrite, and Ammonium .

Table B1: Māʻalaea nutrient samples

						Concentration (µmol/L)			
Sample	**Date**	**Time**	**Lat**	**Lon**	**Salinity**	**PO_4^{3-}**	**Si**	**N+N**	**NH_4^-**
MAL-CSP-1	8/26/2015	6:48	20.793400	-156.508450	4.96	3.60	470.94	219.53	0.30
MAL-CSP-2	8/26/2015	7:00	20.793400	-156.508450	19.57	2.19	242.71	143.77	1.26
MAL-C-1	8/26/2015	6:25	20.794030	-156.507770	32.38	0.59	44.10	21.76	0.71
MAL-C-2	8/26/2015	7:40	20.793330	-156.508420	19.12	2.23	247.99	141.49	1.16
MAL-C-3	8/26/2015	7:56	20.792470	-156.508190	34.73	0.14	4.84	1.10	0.35
MAL-C-4	8/26/2015	8:03	20.791720	-156.506770	34.64	0.13	4.51	1.26	0.13
MAL-C-5	8/26/2015	8:05	20.792790	-156.508740	33.21	0.43	28.71	12.33	0.52
MAL-C-6	8/26/2015	8:12	20.793380	-156.508060	33.26	0.41	28.26	12.68	0.71
MAL-C-7	8/26/2015	8:18	20.793900	-156.507630	31.97	0.59	50.39	25.24	0.86
MAL-C-8	8/26/2015	8:22	20.794490	-156.507050	31.38	0.69	66.45	35.01	0.59
MAL2-1	9/3/2015	15:05	20.793850	-156.507780	32.91	0.37	34.20	16.67	0.57
MAL2-2	9/3/2015	15:10	20.793890	-156.507690	32.88	0.41	33.77	16.45	1.09
MAL2-3	9/3/2015	15:14	20.793920	-156.507630	33.77	0.26	20.71	9.16	0.57
MAL2-4	9/3/2015	15:16	20.793960	-156.507480	34.18	0.16	13.49	4.63	0.46
MAL2-5	9/3/2015	15:18	20.793930	-156.507310	34.55	0.09	5.66	1.54	0.18
MAL2-6	9/3/2015	15:22	20.793920	-156.507170	34.73	0.05	2.71	0.47	0.14
MAL2-7	9/3/2015	15:24	20.793910	-156.506930	34.69	0.05	2.60	0.56	0.05
MAL2-8	9/3/2015	15:35	20.793330	-156.508420	28.72	1.13	128.39	69.63	1.02
MAL2-8-dup	9/3/2015	15:35	20.793330	-156.508420	28.72	1.09	128.24	69.09	0.59

Table B2: Wahikuli Wayside Park nutrient samples.

						Concentration (µmol/L)			
Sample	**Date**	**Time**	**Lat**	**Lon**	**Salinity**	**PO_4^{3-}**	**Si**	**N+N**	**NH_4^-**
WSW-P-1	8/31/2015	10:10	20.896970	-156.685130	32.18	1.84	112.20	9.79	<0.019
WSW-CSP-2	8/31/2015	10:50	20.898240	-156.685120	32.47	0.47	57.00	6.02	<0.019
WSW-CSP-3	8/31/2015	11:06	20.897330	-156.685070	33.09	0.43	38.65	5.91	<0.019
WSW-C-4	8/31/2015	11:32	20.898400	-156.685670	33.46	0.26	27.57	2.79	0.32
WSW-C-5	8/31/2015	11:40	20.898350	-156.685530	33.38	0.25	28.21	2.74	0.32
WSW-C-6	8/31/2015	11:44	20.898060	-156.685500	33.81	0.23	23.55	2.28	0.40
WSW-C-7	8/31/2015	11:52	20.897360	-156.685550	33.26	0.26	30.96	2.99	0.41
WSW-C-8	8/31/2015	11:59	20.898770	-156.685520	33.54	0.26	30.39	2.85	0.31
WSW-C-9	8/31/2015	12:05	20.898170	-156.686840	34.49	0.14	9.86	0.52	0.30

Table B3: Kihei Boat Ramp nutrient samples.

						Concentration (µmol/L)			
Sample	**Date**	**Time**	**Lat**	**Lon**	**Salinity**	**PO_4^{3-}**	**Si**	**N+N**	**NH_4^-**
KBR-1	8/31/2015	11:10	20.707680	-156.446230	2.87	1.92	706.37	223.56	0.05
KBR-1-dup	8/31/2015	11:10	20.707680	-156.446230	2.87	1.89	697.80	212.32	<0.019
KBR-2	8/31/2015	11:34	20.707870	-156.446200	5.57	1.90	618.50	191.32	<0.019
KBR-3	8/31/2015	11:15	20.707720	-156.446590	23.96	0.99	233.90	85.20	0.48
KBR-4	8/31/2015	11:20	20.708400	-156.446820	33.47	0.20	27.25	8.22	0.46
KBR-5	8/31/2015	11:45	20.707890	-156.446420	27.07	0.73	161.68	59.34	0.64
KBR-6	8/31/2015	11:57	20.708150	-156.446475	31.38	0.35	71.90	25.89	0.38
KBR-7	8/31/2015	12:16	20.707440	-156.446470	32.22	0.24	48.90	15.70	<0.019
KBR-8	8/31/2015	12:55	20.709250	-156.447680	34.68	0.01	5.14	0.02	<0.019
KBR-8-dup	8/31/2015	12:55	20.709250	-156.447680	34.71	0.02	4.72	0.02	0.94
KBR-T-1	9/1/2015	11:58	20.707670	-156.446290	27.29	0.66	160.06	58.08	<0.019
KBR-T-2	9/1/2015	12:02	20.707760	-156.446350	25.37	0.85	199.26	72.95	0.55
KBR-T-3	9/1/2015	12:05	20.707890	-156.446440	26.63	0.69	172.38	63.30	<0.019
KBR-T-4	9/1/2015	12:08	20.708010	-156.446500	31.46	0.35	69.38	25.03	0.23
KBR-T-5	9/1/2015	12:12	20.708180	-156.446590	31.53	0.29	69.17	24.51	<0.019
KBR-T-6	9/1/2015	12:16	20.708560	-156.446760	33.14	0.12	31.83	10.69	<0.019
KBR-T-7	9/1/2015	12:20	20.708810	-156.446990	34.05	0.09	15.83	4.68	0.09
KBR-T-7-dup	9/1/2015	12:20	20.708810	-156.446990	35.05	0.09	15.77	4.66	<0.019
KBR-T-P	9/1/2015	11:50	20.707680	-156.446230	3.06	1.83	687.84	214.46	<0.019

Table B4: Honolua Bay nutrient samples.

						Concentration (µmol/L)			
Sample	**Date**	**Time**	**Lat**	**Lon**	**Salinity**	**PO_4^{3-}**	**Si**	**N+N**	**NH_4^-**
HON-1	9/5/2015	17:20	21.012950	-156.638480	0.38	0.44	202.96	0.25	<0.019
HON-1-dup	9/5/2015	17:20	21.012950	-156.638480	0.38	0.45	204.88	0.43	0.09
HON-2	9/5/2015	17:35	21.013300	-156.639360	0.89	1.57	688.47	21.46	0.09
HON-3	9/5/2015	17:15	21.013370	-156.639400	32.35	0.22	42.21	1.72	0.80
HON-4	9/5/2015	17:18	21.013450	-156.639430	32.85	0.18	35.80	1.41	0.10
HON-5	9/5/2015	17:22	21.013600	-156.639530	32.86	0.19	33.27	1.42	0.07
HON-6	9/5/2015	17:25	21.013740	-156.639570	32.6	0.23	38.19	1.94	0.27
HON-7	9/5/2015	17:30	21.013880	-156.639680	32.6	0.24	37.25	2.18	0.37
HON-8	9/5/2015	17:33	21.013690	-156.639450	32.42	0.22	40.79	1.69	0.19
HON-9	9/5/2015	17:37	21.013640	-156.639660	32.02	0.24	47.57	2.08	0.16

Table B5: Wailupe Beach Park nutrient samples.

						Concentration (µmol/L)			
Sample	**Date**	**Time**	**Lat**	**Lon**	**Salinity**	**PO_4^{3-}**	**Si**	**N+N**	**NH_4^-**
4_HT	1/28/2016	~8:00	21.27562	-157.76268	30.86	0.49	99.84	5.97	0.57
5_HT	1/28/2016	~8:00	21.27580	-157.76233	29.044	0.60	144.72	11.46	0.57
TS_HT	1/28/2016	~8:00	21.27570	-157.76253	31.105	0.45	95.26	5.80	0.48
7_HT	1/28/2016	~8:00	21.27562	-157.76251	31.448	0.40	87.05	5.07	0.49
8_HT	1/28/2016	~8:00	21.27576	-157.76244	29.639	0.53	131.36	10.13	0.30
9_HT	1/28/2016	~8:00	21.27551	-157.76248	31.759	0.34	80.70	3.47	0.57
10_HT	1/28/2016	~8:00	21.27540	-157.76245	32.955	0.22	51.16	1.08	0.48
4_MT	1/28/2016	~10:00	21.27562	-157.76268	26.987	0.76	206.66	13.15	0.55
4_MT-dup	1/28/2016	~10:00	21.27562	-157.76268	26.987	0.76	205.55	13.13	0.56
5_MT	1/28/2016	~10:00	21.27580	-157.76233	26.326	0.80	218.54	16.25	0.62
7_MT	1/28/2016	~10:00	21.27562	-157.76251	30.407	0.47	122.84	6.13	0.57
8_MT	1/28/2016	~10:00	21.27576	-157.76244	26.275	0.78	218.30	15.94	0.50
8_MT-dup	1/28/2016	~10:00	21.27576	-157.76244	26.275	0.81	219.30	15.97	0.65
9_MT	1/28/2016	~10:00	21.27551	-157.76248	30.783	0.40	109.65	4.84	0.67
10_MT	1/28/2016	~10:00	21.27540	-157.76245	31.389	0.32	94.57	3.48	0.78
4_LT	1/28/2016	~12:30	21.27562	-157.76268	26.712	0.77	212.95	14.91	0.57
5_LT	1/28/2016	~12:30	21.27580	-157.76233	20.267	1.19	362.16	29.64	1.59
TS_LT	1/28/2016	~12:30	21.27570	-157.76253	20.613	1.19	350.85	26.72	0.57
7_LT	1/28/2016	~12:30	21.27562	-157.76251	21.521	1.12	330.64	23.26	0.63
8_LT	1/28/2016	~12:30	21.27576	-157.76244	19.973	1.30	366.91	28.70	0.68
9_LT	1/28/2016	~12:30	21.27551	-157.76248	28.786	0.61	158.59	9.45	0.80
10_LT	1/28/2016	~12:30	21.27540	-157.76245	29.612	0.53	139.29	7.45	0.73
Boil_LT	1/28/2016	~12:30	21.27556	-157.76250	21.842	1.12	324.80	25.32	0.53
Boil_dup	1/28/2016	~12:30	21.27556	-157.76250	21.842	1.11	326.44	25.19	0.36

REFERENCES

Amato, D. 2015. Ecophysiological responses of macroalgae to submarine groundwater discharge in Hawaii. Ph.D. dissertation. University of Hawai‘i.

Banks, W.S., Paylor, R.L. and Hughes, W.B., 1996. Using thermal-infrared imagery to delineate ground-water discharge. Ground Water, 34(3), pp. 434-443.

Bishop, J.M., Glenn, C.R., Amato, D.W. and Dulai, H., 2015. Effect of land use and groundwater flow path on submarine groundwater discharge nutrient flux. Journal of Hydrology: Regional Studies. http://dx.doi.org/10.1016/j.ejrh.2015.10.008

Bos, M.G., Replogle, J.A. and Clemmens, A.J., 1984. Flow measuring flumes for open channel systems.

Bratton, J.F., 2010. The three scales of submarine groundwater flow and discharge across passive continental margins. The Journal of Geology, 118(5), pp. 565-575.

Burnett, W.C. and Dulaiova, H., 2003. Estimating the dynamics of groundwater input into the coastal zone via continuous radon-222 measurements. Journal of Environmental Radioactivity, 69(1), pp. 21-35.

Burnett, W.C. and Dulaiova, H., 2006. Radon as a tracer of submarine groundwater discharge into a boat basin in Donnalucata, Sicily. Continental Shelf Research, 26(7), pp. 862-873.

Burnett, W.C., Aggarwal, P.K., Aureli, A., Bokuniewicz, H., Cable, J.E., Charette, M.A., Kontar, E., Krupa, S., Kulkarni, K.M., Loveless, A. and Moore, W.S., 2006. Quantifying submarine groundwater discharge in the coastal zone via multiple methods. Science of the Total Environment, 367(2), pp. 498-543.

Cheng, C.L., 2014. Low-flow characteristics of streams in the Lahaina District, West Maui, Hawai'i. US Geological Survey Scientific Investigations Report 2014-5087, 58 p. http://dx.doi.org/10.3133/sir20145087

Conklin, E.J., and Smith, J.E., 2005. Abundance and spread of the invasive red algae, Kappaphycus spp., in Kane’ohe Bay, Hawai’i and an experimental assessment of management options. Biologic Invasions, 7, pp. 1029-1039. doi 10.1007/s10530-004-3125-x.

Corbett, D.R., Chanton, J., Burnett, W., Dillon, K., Rutkowski, C. and Fourqurean, J.W., 1999. Patterns of groundwater discharge into Florida Bay. Limnology and Oceanography, 44(4), pp. 1045-1055.

Costa, O.S., Nimmo, M. and Attrill, M.J., 2008. Coastal nutrification in Brazil: a review of the role of nutrient excess on coral reef demise. Journal of South American Earth Sciences, 25(2), pp. 257-270.

Dailer, M.L., Knox, R.S., Smith, J.E., Napier, M. and Smith, C.M., 2010. Using $\delta^{15}N$ values in algal tissue to map locations and potential sources of anthropogenic nutrient inputs on the island of Maui, Hawai'i, USA. Marine Pollution Bulletin, 60(5), pp. 655-671.

Danielescu, S., MacQuarrie, K.T. and Faux, R.N., 2009. The integration of thermal infrared imaging, discharge measurements and numerical simulation to quantify the relative contributions of freshwater inflows to small estuaries in Atlantic Canada. Hydrological processes, 23(20), pp. 2847-2859.

Dollar, S.J. and Atkinson, M.J., 1992. Effects of nutrient subsidies from groundwater to nearshore marine ecosystems off the island of Hawaii. Estuarine, Coastal and Shelf Science, 35(4), pp. 409-424.

Duarte, T., Hemond, H.F., Frankel, D. and Frankel, S., 2006. Assessment of submarine groundwater discharge by handheld aerial infrared imagery: Case study of Kaloko fishpond and bay, Hawai'i. Limnology and Oceanography: Methods, 4(7), pp. 227-236.

Dulaiova, H., Camilli, R., Henderson, P.B. and Charette, M.A., 2010. Coupled radon, methane and nitrate sensors for large-scale assessment of groundwater discharge and non-point source pollution to coastal waters. Journal of Environmental Radioactivity, 101(7), pp. 553-563.

Engott, J.A., Johnson, A.G., Bassiouni, M. and Izuka, S.K., 2015. Spatially distributed groundwater recharge for 2010 land cover estimated using a water-budget model for the Island of O'ahu, Hawai'i. US Geological Survey Scientific Investigations Report 2015-5010, 49p. http://dx.doi.org/10.3133/sir20155010.

Giambelluca, T.W., and Nullet, D., 1991. Influence of the trade-wind inversion on the climate of a leeward mountain slope in Hawaii. Climate Research, 1, pp. 207-216.

Gingerich, S.B., 2008. Ground-water availability in the Wailuku Area, Maui, Hawai'i. US Geological Survey Scientific Investigations Report 2008-5236, 95p.

Glenn, C.R., Whittier, R.B., Dailer, M.L., Dulaiova, H., El-Kadi, A.I., Fackrell, J., Kelly, J.L., Waters, C.A., 2012. Lahaina groundwater tracer study – Lahaina, Maui, Hawai'i. Final Interim Report. Prepared for the State of Hawai'i Department of Health, the U.S. Environmental Protection Agency, and the U.S. Army Engineer Research and Development Center, pp. 463. http://www.epa.gov/region9/water/groundwater/uic-pdfs/lahaina02/lahaina-final-interim-report.pdf.

Glenn, C.R., Whittier, R.B., Dailer, M.L., Dulaiova, H., El-Kadi, A.I., Fackrell, J., Kelly, J.L., Waters, C.A., Sevadjian, J., 2013. Lahaina groundwater tracer study — Lahaina, Maui, Hawai‘i, Final Report. Prepared for the State of Hawai‘i Department of Health, the U.S. Environmental Protection Agency, and the U.S. Army Engineer Research and Development Center, 502p. http://www.epa.gov/region9/water/groundwater/uic-pdfs/lahaina02/lahaina-gw-tracer-study-final-report-june-2013.pdf.

Goldman, D.B. and Chen, J.H., 2005, October. Vignette and exposure calibration and compensation. In Tenth IEEE International Conference on Computer Vision (ICCV'05), 1, pp. 899-906.

Heiss, J.W. and Michael, H.A., 2014. Saltwater-freshwater mixing dynamics in a sandy beach aquifer over tidal, spring-neap, and seasonal cycles. Water Resources Research, 50(8), pp. 6747-6766.

Hu, C., Muller-Karger, F.E. and Swarzenski, P.W., 2006. Hurricanes, submarine groundwater discharge, and Florida's red tides. Geophysical Research Letters, 33(11). DOI: 10.1029/2005GL025449.

Hunt, C.D. and Rosa, S.N., 2009. A multitracer approach to detecting wastewater plumes from municipal injection wells in nearshore marine waters at Kihei and Lahaina, Maui, Hawaii. US Geological Survey Scientific Investigations Report 2009-5253, 166p.

Hunter, C.L. and Evans, C.W., 1995. Coral reefs in Kāne‘ohe Bay, Hawai‘i: Two centuries of western influence and two decades of data. Bulletin of Marine Science, 57(2), pp. 501-515.

Johannes, R.E., 1980. Ecological significance of the submarine discharge of groundwater. Marine Ecology, 3(4), pp. 365-373.

Johnson, A.G. 2008. Groundwater discharge from the leeward half of the Big Island, Hawaii. M.S. thesis. University of Hawai‘i.

Johnson, A.G., Glenn, C.R., Burnett, W.C., Peterson, R.N. and Lucey, P.G., 2008. Aerial infrared imaging reveals large nutrient-rich groundwater inputs to the ocean. Geophysical Research Letters, 35(15). DOI: 10.1029/2008GL034574

Jurisa, J.T. and Chant, R.J., 2013. Impact of offshore winds on a buoyant river plume system. Journal of Physical Oceanography, 43(12), pp. 2571-2587.

Kelly, J.L., Glenn, C.R. and Lucey, P.G., 2013. High-resolution aerial infrared mapping of groundwater discharge to the coastal ocean. Limnology and Oceanography: Methods, 11, pp. 262-277. doi:10.4319/lom.2013.11.262.

Knee, K.L., Layton, B.A., Street, J.H., Boehm, A.B. and Paytan, A., 2008. Sources of nutrients and fecal indicator bacteria to nearshore waters on the north shore of Kauai (Hawaii, USA). Estuaries and Coasts, 31(4), pp. 607-622.

Kwon, E.Y., Kim, G., Primeau, F., Moore, W.S., Cho, H.M., DeVries, T., Sarmiento, J.L., Charette, M.A. and Cho, Y.K., 2014. Global estimate of submarine groundwater discharge based on an observationally constrained radium isotope model. Geophysical Research Letters, 41(23), pp. 8438-8444.

Li, L., Barry, D.A., Stagnitti, F. and Parlange, J.Y., 1999. Submarine groundwater discharge and associated chemical input to a coastal sea. Water Resources Research, 35(11), pp. 3253-3259.

Lirman D., 2001. Competition between macroalgae and corals: effects of herbivore exclusion and increased algal biomass on coral survivorship and growth. Coral Reefs, 19(4), pp. 392-399. doi: 10.1007/s003380000125.

Martinez, J.A., Smith, C.M., Richmond, R.H., 2012. Invasive algal mats degrade coral reef physical habitat quality. Estuarine, Coastal and Shelf Science, 99, pp. 42-49. doi:10.1016/j.ecss.2011.12.022.

McCook, L., Jompa, J., and Diaz-Pulido, G., 2001, Competition between corals and algae on coral reefs: a review of evidence and mechanisms. Coral Reefs, 19, pp. 400-417. doi: 10.1007/s003380000129.

Moore, W.S., 1999. The subterranean estuary: a reaction zone of ground water and sea water. Marine Chemistry, 65(1), pp. 111-125.

Moore, W.S., Sarmiento, J.L. and Key, R.M., 2008. Submarine groundwater discharge revealed by ^{228}Ra distribution in the upper Atlantic Ocean. Nature Geoscience, 1(5), pp. 309-311. doi:310.1038/ngeo1183.

Natural Area Reserve System, 2012. Ahihi-Kinau Natural Area Reserve Management Plan. Prepared for the Department of Land and Natural Resources, Honolulu, Hawai‘i. 118p.

Paerl, H.W., 1997, Coastal eutrophication and harmful algal blooms: Importance of atmospheric deposition and groundwater as "new" nitrogen and other nutrient sources. Limnology and Oceanography, Vol. 42(5 part 2), pp. 1154-1165.

Paerl, H.W., and Otten, T.G., 2013, Harmful cyanobacterial blooms: causes, consequences, and controls. Microbial Ecology 54(4), pp. 995-1010. doi: 10.1007/s00248-012-0159-y.

Paytan, A., Shellenbarger, G.G., Street, J.H., Gonneea, M.E., Davis, K., Young, M.B. and Moore, W.S., 2006. Submarine groundwater discharge: An important source of new inorganic nitrogen to coral reef ecosystems. Limnology and Oceanography, 51(1), pp. 343-348.

Peterson, R.N., Burnett, W.C., Glenn, C.R., and Johnson, A.D., 2009. Quantification of point-source groundwater discharges to the ocean from the shoreline of the Big Island, Hawaii. Limnology and Oceanography, 54(3), pp. 890-904.

Richardson, C.M., Dulai, H. and Whittier, R.B., 2015. Sources and spatial variability of groundwater-delivered nutrients in Maunalua Bay, O'ahu, Hawai 'i. Journal of Hydrology: Regional Studies. http://dx.doi.org/10.1016/j.ejrh.2015.11.006

Röper, T., Greskowiak, J. and Massmann, G., 2015. Instabilities of submarine groundwater discharge under tidal forcing. Limnology and Oceanography, 60(1), pp. 22-28.

Ross. M., White, D., Aiwohi, M., Walton, M., Sudek, M., Lager, D., and Jokiel, P.L., 2012. Characterization of "dead zones" and population of demography of *Porites compressa* along a gradient of anthropogenic nutrient input at Kahekili Beach Park, Maui. Final Report for Project C11722 submitted to State of Hawai'i, Department of Land and Natural Resources, Division of Aquatic Resources.

Santos, I.R., Dimova, N., Peterson, R.N., Mwashote, B., Chanton, J. and Burnett, W.C., 2009. Extended time series measurements of submarine groundwater discharge tracers (^{222}Rn and CH_4) at a coastal site in Florida. Marine Chemistry, 113(1), pp. 137-147.

Santos, I.R., Eyre, B.D. and Huettel, M., 2012. The driving forces of porewater and groundwater flow in permeable coastal sediments: A review. Estuarine, Coastal and Shelf Science, 98, pp. 1-15.

Shade, P.J., 1996. Water budget for the Lahaina District, island of Maui, US Geological Survey Hawai'i Water-Resources Investigations Report 96-4238, 27p.

Shade, P.J., 1997. Water budget for the Iao area, island of Maui, Hawaii. Water-Resources Investigations Report 97–4244, 29p.

Shade, P.J., 1999. Water budget of East Maui, Hawaii: US Geological Survey Water Resources Investigations Report 98–4159, 36p.

Sherrod, D.R., Sinton, J.M., Watkins, S.E., and Kelly, B.M., 2007. Geologic map of the state of Hawai'i. US Geological Survey Open-File Report 2007-1089, with GIS database.

Slomp, C.P. and Van Cappellen, P., 2004. Nutrient inputs to the coastal ocean through submarine groundwater discharge: controls and potential impact. Journal of Hydrology, 295(1), pp. 64-86.

Smith, J.E., Hunter, C.L., and Smith, C.M., 2002, Distribution and reproductive characteristics of nonindigenous and invasive marine algae in the Hawaiian Islands. Pacific Science, 56(3), pp. 299-315.

Smith, J.E., Runcie, J.W., Smith, C.M., 2005, Characterization of a large-scale ephemeral bloom of the green alga Cladophora sericea on the coral reefs of west Maui, Hawai‘i. Marine Ecology Progress Series, 302, pp. 77-91. doi:10.3354/meps302077.

Smith, S.V., Kimmerer, W.J., Laws, E.A., Brock, R.E., Walsh, T.W., 1981, Kāne‘ohe Bay sewage diversion experiment: Perspectives on ecosystem responses to nutritional perturbation. Pacific Science, 35(4), pp. 279-397. http://hdl.handle.net/10125/616.

Soicher, A.J. and Peterson, F.L., 1997. Terrestrial nutrient and sediment fluxes to the coastal waters of west Maui, Hawai'i. Pacific Science, 51(3), p. 221-232.

Stearns, H.T., 1939. Geologic map and guide of the island of Oahu, Hawai‘I (No. 2). Division of Hydrography of the Territory of Hawai‘i.

Stearns, H.T., and MacDonald, G.A., 1942, Geology and Groundwater resources of the island of Maui, Hawaii: Hawaii (Territory) Division of Hydrography Bulletin, v. 7, 344p.

Street, J.H., Knee, K.L., Grossman, E.E. and Paytan, A., 2008. Submarine groundwater discharge and nutrient addition to the coastal zone and coral reefs of leeward Hawai'i. Marine Chemistry, 109(3), pp. 355-376.

Swarzenski, P.W., Storlazzi, C.D., Presto, M.K., Gibbs, A.E., Smith, C.G., Dimova, N.T., Dailer, M.L. and Logan, J.B., 2012. Nearshore morphology, benthic structure, hydrodynamics, and coastal groundwater discharge near Kahekili Beach Park, Maui, Hawai‘i. US Geological Survey Open-File Report 2012-1166, 34p.

Tamborski, J.J., Rogers, A.D., Bokuniewicz, H.J., Cochran, J.K. and Young, C.R., 2015. Identification and quantification of diffuse fresh submarine groundwater discharge via airborne thermal infrared remote sensing. Remote Sensing of Environment, 171, pp. 202-217.

Valiela, I., Costa, J., Foreman, K., Teal, J.M., Howes, B. and Aubrey, D., 1990. Transport of groundwater-borne nutrients from watersheds and their effects on coastal waters. Biogeochemistry, 10(3), pp. 177-197.

Van Beukering, P. and Cesar, H.S., 2004. Ecological economic modeling of coral reefs: Evaluating tourist overuse at Hanauma Bay and algae blooms at the Kihei Coast, Hawai'i. Pacific Science, 58(2), pp. 243-260.

Wilson, J., and Rocha, C., 2012. Regional scale assessment of submarine groundwater discharge in Ireland combining medium resolution satellite imagery and geochemical tracing techniques. Remote Sensing of the Environment, 119, pp. 21-34. doi:10.1016/j.rse.2011.11.018

Wilson, J. and Rocha, C., 2016. A combined remote sensing and multi-tracer approach for localizing and assessing groundwater-lake interactions. International Journal of Applied Earth Observation and Geoinformation, 44, pp. 195-204.

Young, C., Tamborski, J. and Bokuniewicz, H., 2015. Embayment scale assessment of submarine groundwater discharge nutrient loading and associated land use. Estuarine, Coastal, and Shelf Science, 158, pp. 20-30.